

University of Nebraska - Lincoln

## DigitalCommons@University of Nebraska - Lincoln

---

Department of Mechanical and Materials  
Engineering: Dissertations, Theses, and Student  
Research

Mechanical & Materials Engineering,  
Department of

---

5-2024

### Development of a Multi-Use Modular Microfluidic Platform Using 3D Printing

Carson Emeigh

*University of Nebraska-Lincoln*, [cemeigh2@unl.edu](mailto:cemeigh2@unl.edu)

Follow this and additional works at: <https://digitalcommons.unl.edu/mechengdiss>



Part of the [Hardware Systems Commons](#), [Materials Science and Engineering Commons](#), [Mechanical Engineering Commons](#), and the [VLSI and Circuits, Embedded and Hardware Systems Commons](#)

---

Emeigh, Carson, "Development of a Multi-Use Modular Microfluidic Platform Using 3D Printing" (2024).  
*Department of Mechanical and Materials Engineering: Dissertations, Theses, and Student Research*. 198.  
<https://digitalcommons.unl.edu/mechengdiss/198>

This Article is brought to you for free and open access by the Mechanical & Materials Engineering, Department of at DigitalCommons@University of Nebraska - Lincoln. It has been accepted for inclusion in Department of Mechanical and Materials Engineering: Dissertations, Theses, and Student Research by an authorized administrator of DigitalCommons@University of Nebraska - Lincoln.

DEVELOPMENT OF A MULTI-USE MODULAR MICROFLUIDIC PLATFORM  
USING 3D PRINTING

by

Carson C. Emeigh

A THESIS

Presented to the Faculty of

The Graduate College at the University of Nebraska

In Partial Fulfillment of Requirements

For the Degree of Master of Science

Major: Mechanical Engineering and Applied Mechanics

Under the Supervision of Professor Sangjin Ryu

Lincoln, Nebraska

May, 2024

DEVELOPMENT OF A MULTI-USE MODULAR MICROFLUIDIC PLATFORM  
USING 3D PRINTING

Carson Emeigh, M.S.

University of Nebraska, 2024

Advisor: Sangjin Ryu

Microfluidic lab-on-a-chip (LoC) technology has driven numerous innovations due to their ability to perform laboratory-scale experiments on a single chip using microchannels. Although LoC technology has been innovative, it still suffers from limitations related to its fabrication and design flexibility. Typical LoC fabrication, with photolithography, is time consuming, expensive, and inflexible. To overcome the limitations of LoC devices, modular microfluidic platforms have been developed where multiple microfluidic modules, each with a specific function or group of functions, can be combined on a single platform. Modular microfluidics have overcome some of the limitations of LoC devices, but currently, their fabrication is complex, and they remain relatively inaccessible. This study attempts to address the limitations of both LoC microfluidics and modular microfluidic platforms by implementing stereolithography 3D printing for ease of fabrication, design flexibility, and increased accessibility. A modular platform with reversible connections was developed that could accommodate two microfluidic modules in series. The optimal printing parameters and fabrication procedure for printing both microfluidic molds and microfluidic devices was found. The

base to a modular platform was designed and 3D printed with integrated O-ring module attachments and luer-lock mechanisms for connection to external flow sources. To demonstrate the capability of the developed platform, a microfluidic device previously used to compress cells by inflating a thin PDMS membrane, like a balloon, was reconfigured to serve as an active mixing microfluidic module. Next, the height response of the balloons of the active mixer was characterized in response to an applied pressure to ensure the performance of the mixer fabricated with 3D printing was comparable to that of the previous study. Separately, a straight-channel microfluidic module was fabricated. The flow through the straight-channel microfluidic was measured using particle tracking velocimetry because many studies require shear stress application. Finally, the modular platform, mixing module, and straight-channel module was combined, and a mixing experiment was performed by dynamically actuating the balloons of the mixing module at varying frequencies. The fabricated mixing module could mix two samples before they flowed into the second module, and the platform was capable of quick, reversible, and leak-free connections.

## Acknowledgements

This degree has been one of the hardest things that I have ever attempted. Without the help, guidance, support, and encouragement of Dr. Sangjin Ryu, none of it would have been possible. I will forever be grateful for the opportunities that he has given me, and for the opportunities learning under him will provide me in the future. Anytime I speak with him, research or otherwise, he always has my best interests in mind and wisdom beyond his years. I would also like to thank Dr. Jae Sung Park, Dr. Ryan Pedrigi, and Dr. Stephen Morin for their time, for serving on my thesis committee, and for helping me to improve my thesis.

I would also like to thank all of the people whom I have spent my time with during my undergraduate and graduate program. I would like to thank all the people who have worked in the lab alongside me. Particularly, I want to thank Haipeng Zhang for being the person who first helped me grow in Dr. Ryu's lab. Additionally, I would like to thank Rose Pineda for her help with the compression testing of PDMS presented in this thesis. I am grateful for all of the friends I have made throughout my time at UNL, and for the professors who have instilled their knowledge into me. Additionally, I want to thank Ulises Gallegos, Oghenetega Obewhere, and Rajesh Keloth, you all have become some of my closest friends, and I am thankful that we were able to meet during my time in the College of Engineering.

I would also like to thank all my friends and family whom without, none of this would have been possible. Particularly, I want to appreciate my parents Kerry Emeigh and Wes Emeigh for their unwavering support and unconditional love throughout my entire life. I would like to thank my girlfriend Kirsten Kieper who has been there for me

through this process, and who encourages me to grow and to be the best version of myself. I want to thank Cole Emeigh, Elijah Wilcox, and James Craig. Dan and Grant, I am so grateful you have been, and will continue to be, life-long friends. Finally, I would also like to thank all of my family and friends whom I could not list here. Thank you all for being a part of my life and making my experience enjoyable. Without you all, I would not be where I am today.

## List of Publications

**C. Emeigh** and S. Ryu (2024) Using brightfield microscopy to assess the balloon expansion performance of a microfluidic cell compression device, American Society of Mechanical Engineers (ASME) Fluids Engineering Division Summer Meeting (FEDSM) 2024, ASME FEDSM2024-130787, Anaheim, California, USA. Accepted for presentation. ASME Graduate Returning Scholar Award.

**C. Emeigh**, R. Pineda, B. Harms, and S. Ryu (2023) The effects of balloon thickness on the viability of a microfluidic cell compression device, American Society of Mechanical Engineers (ASME) International Mechanical Engineering Congress and Exposition (IMECE) 2023, ASME IMECE2023-113642, New Orleans, Louisiana, USA. ASME FEDSM Graduate Student Scholar Award.

**C. Emeigh**, A. Griswold, R. Hassan Pallock, J. Sahni, M. Schake, U. Anuta, J. Deters, and S. Ryu (2023) Group-project-based development of a modular microfluidic platform: A case report on a hands-on microfluidics course, American Society of Engineering Education (ASEE) 2023 Midwest Section Conference, Lincoln, Nebraska, USA.

**C. Emeigh**, H. Zhang, and S. Ryu (2022) Fabrication of a microfluidic cell compressor using a 3D-printed mold, American Society of Mechanical Engineers (ASME) Fluids

Engineering Division Summer Meeting (FEDSM) 2022, ASME FEDSM2022-87613, Toronto, Ontario, Canada.

H. Zhang, **C. Emeigh**, S. Brooks, T. Wei, S. Ryu, Y. Chatzizisis, and X. Liu (2022) Fabrication of a multi-well plate channel device with reversible seals, American Society of Mechanical Engineers (ASME) Fluids Engineering Division Summer Meeting (FEDSM) 2022, ASME FEDSM2022-87923, Toronto, Ontario, Canada.

S. Ryu, H. Zhang, and **C. Emeigh** (2022) The dark annulus of a drop in a Hele-Shaw cell is caused by the refraction of light through its meniscus, *Micromachines*, 13, 1021.

**C. Emeigh**, H. Bak, D. Kizghin, H. Zhang, and S. Ryu (2022) Marinated eggs: An engaging quantitative demonstration of diffusion, *American Journal of Physics*, 90, 317-320. Featured in the cover image.

**C. Emeigh**, H. Zhang, and S. Ryu (2021) Microfluidics-based fabrication of a Hele-Shaw cell device for drop coalescence imaging, American Society of Mechanical Engineers International Mechanical Engineering Congress and Exposition 2021, ASME IMECE2021-68063. ASME Young Engineers Paper Contest 1<sup>st</sup> Place.

**Table of Contents**

Acknowledgements .....	iv
List of Publications .....	vi
List of Figures .....	xii
List of Tables .....	xv
Chapter 1: Introduction .....	1
1.1 Microfluidic Lab-on-a-Chip Devices .....	1
1.2 Current Status and Limitations of Microfluidics.....	5
1.3 Modular Microfluidic Platforms .....	9
1.4 Previous Studies .....	12
1.5 Mixing in Microchannels .....	16
1.6 Purpose of This Study .....	17
Chapter 2: 3D Printing Microfluidics .....	21
2.1 3D Printing for Microfluidic Fabrication .....	21
2.2 3D Printer Maintenance and Preparation .....	27
2.3 Printing Parameters and Effects on Final Print .....	31
2.4 Design and Fabrication Consideration for Green Mold Resin.....	34
2.4.1 Design Considerations for Increasing Printability of Green Resin Molds .....	35
2.4.2 Processing of Green Mold Resin .....	39
2.5 Design and Fabrication Considerations for Clear Channel Resin.....	41

2.5.1 Design Considerations for Increasing Printability of Clear Channel Resin .....	41
2.5.2 Processing of Clear Channel Resin .....	45
Chapter 3: Motherboard and Module Fabrication .....	48
3.1 Motherboard Design and Fabrication.....	48
3.1.1 Microfluidic Motherboard Design.....	48
3.1.2 Motherboard Fabrication .....	50
3.2 Microfluidic Module Design and Fabrication.....	51
3.2.1 Microfluidic Module Design .....	51
3.2.2 Soft Lithography for the Mixing Module .....	57
3.3 Motherboard and Module Assembly.....	62
Chapter 4: Balloon Inflation Characterization.....	64
4.1 Motivation for Characterizing Balloon Height Response.....	64
4.2 Previous Balloon Characterization Methods.....	67
4.3 Confocal Laser Scanning Microscopy and Image Processing .....	68
4.3.1 Diameter Characterization.....	68
4.3.2 Balloon Height Measurement with Confocal Microscopy and Image Processing .....	70
4.3.3 Young's Modulus Characterization of PDMS.....	74
4.3.4 Balloon Diameter Results.....	75
4.3.5 Balloon Height Results from Image Processing.....	78

4.3.6 Young's modulus of PDMS .....	81
4.3.7 Comparison with a Theoretical Prediction .....	82
4.4 Inverted Brightfield Microscopy for Balloon Characterization .....	84
4.4.1 Balloon Diameter Measurement .....	84
4.4.2 Top-View Imaging of the Inflated Balloons.....	86
4.4.3 Side-View Imaging of the Inflated Balloons .....	90
4.4.4 Results of Diameter Measurement .....	91
4.4.5 Inflated Balloon Height vs Balloon Diameter .....	94
4.4.6 Discussion of the Top- and Side-View Imaging Methods .....	97
Chapter 5: Flow Characterization Using PTV .....	100
5.1 Introduction (What is PTV?).....	100
5.2 Measuring Channel Height.....	103
5.3 Particle Selection and Imaging Methods.....	105
5.4 MATLAB-Based Image Processing.....	109
5.5 Results from PTV .....	117
5.6 Discussion .....	122
Chapter 6: Applications of the Microfluidic Motherboard and Its Modules .....	125
6.1 Motherboard and Module Operation.....	126
6.2 Active Microfluidic Mixing .....	131
6.3 Results .....	136

6.3.1 Mixing in the Microfluidic Mixer .....	136
6.3.2 Mixing Efficiency Measured in the Second Module.....	141
6.4 Discussion .....	143
6.4.1 Improving Mixing Within the Balloon Module .....	143
6.4.2 Pulsatile Flow Motion Due to Balloon Inflation .....	147
6.5 Possible Future Applications.....	149
Chapter 7: Conclusion and Prospective Research .....	152
7.1 Conclusion.....	152
7.2 Prospective Research Directions .....	153
References.....	154
Appendix A: MATLAB Code Used for Balloon Height Image Processing.....	167
Appendix B: MATLAB-Based Balloon Diameter Measurement Code Using Kasa's Method .....	173
Appendix C: MATLAB Code Used for PTV Analysis .....	175
Appendix D: MATLAB Code Used for Mixing Analysis.....	178

## List of Figures

Figure 1-1: Examples of microfluidic Lab-on-a-Chip (LoC) devices .....	1
Figure 1-2: Examples of microfluidic Organ-on-a-chip (OoC) devices.....	2
Figure 1-3: Point-of-Care microfluidic device capable of detecting signs of diabetes and hyperlipidemia .....	4
Figure 1-4: A schematic of the photolithography process for fabricating microfluidic molds.....	7
Figure 1-5: A schematic of a modular microfluidic platform.....	10
Figure 1-6: Examples of connection mechanisms between microfluidic modules.....	11
Figure 1-7: Schematic of microfluidic cell compression device fabricated using photolithography and soft lithography.....	13
Figure 1-8: Balloon height response of the microfluidic cell compressor to an applied pressure .....	15
Figure 1-9: An image of the microfluidic motherboard, mixing module, and straightchannel module developed in this study .....	18
Figure 2-1: Schematic of a stereolithography 3D printer .....	24
Figure 2-2: Images of a 3D printed microfluidic mold and channel device .....	27
Figure 2-3: An image of a microfluidic 3D printer.....	28
Figure 2-4: Flowchart of the fabrication procedure for microfluidic molds and microfluidic devices.....	35
Figure 2-5: Image of 3D printed molds for microfluidic fabrication.....	37
Figure 2-6: Test device with various channel lengths .....	43
Figure 3-1: Image of the motherboard and its connection mechanisms .....	49

Figure 3-2: Computer aided design (CAD) drawing of the motherboard.....	50
Figure 3-3: Images of the PDMS mixing module.....	52
Figure 3-4: Computer aided design (CAD) drawing of the balloon part mold.....	54
Figure 3-5: Computer aided design (CAD) drawing of the mixing channel part mold....	56
Figure 3-6: Schematic diagram of the soft lithography procedure to fabricate microfluidics .....	58
Figure 3-7: Clamping setup used for microfluidic soft lithography with 3D printed molds .....	59
Figure 3-8: Effect of spin-coater rotational speed (rpm) on the thickness of the resulting PDMS membrane.....	61
Figure 4-1: Image of the fabricated device for balloon height measurement .....	67
Figure 4-2: Measurement of balloon diameter with laser scanning confocal microscopy	69
Figure 4-3: Image processing procedure for laser scanning confocal microscopy data ...	72
Figure 4-4: Balloon diameter results from laser scanning confocal microscopy.....	77
Figure 4-5: Measured height of the inflated balloon found through image processing....	79
Figure 4-6: Experimentally measured stress-strain data of a PDMS sample.....	82
Figure 4-7: Balloon diameter measurement using circle fitting .....	85
Figure 4-8: Brightfield microscopy imaging setup for balloon height measurement.....	88
Figure 4-9: Coverslip calibration data .....	90
Figure 4-10: Side-view imaging of a 2.5 mm-diameter balloon.....	91
Figure 4-11: Measured balloon diameters from circle fitting.....	93
Figure 4-12: Measured inflation height of the balloons from top-view imaging .....	95
Figure 5-1: A schematic overview of a typical PTV experiment .....	100

Figure 5-2: A schematic diagram of volumetric illumination .....	102
Figure 5-3: Image of straight channel microfluidic device.....	109
Figure 5-4: PTV image processing procedure .....	110
Figure 5-5: Streamline results from PTV code.....	116
Figure 5-6: Velocity results from PTV measurement.....	120
Figure 6-1: Hypothetical mechanobiology study overview.....	126
Figure 6-2: Experimental setup of mixing experiment with dynamic balloon inflation.	127
Figure 6-3: A time series of a balloon inflation cycle .....	130
Figure 6-4: Balloon module for mixing and straight-channel module connected to motherboard for mixing experiment .....	132
Figure 6-5: MATLAB image processing for mixing images.....	134
Figure 6-6: Quantitative mixing analysis of mixing within the active mixing microfluidic .....	139
Figure 6-7: Image of mixing channel before mixing to show channel misalignment ....	140
Figure 6-8: Quantitative mixing analysis of mixing within the second module.....	142
Figure 6-9: Mixing efficiencies in the second module .....	143
Figure 6-10: Function of a 3 way normally closed solenoid valve.....	145
Figure 6-11: Images of the mixing module to visually demonstrate the pulsatile flow .	148

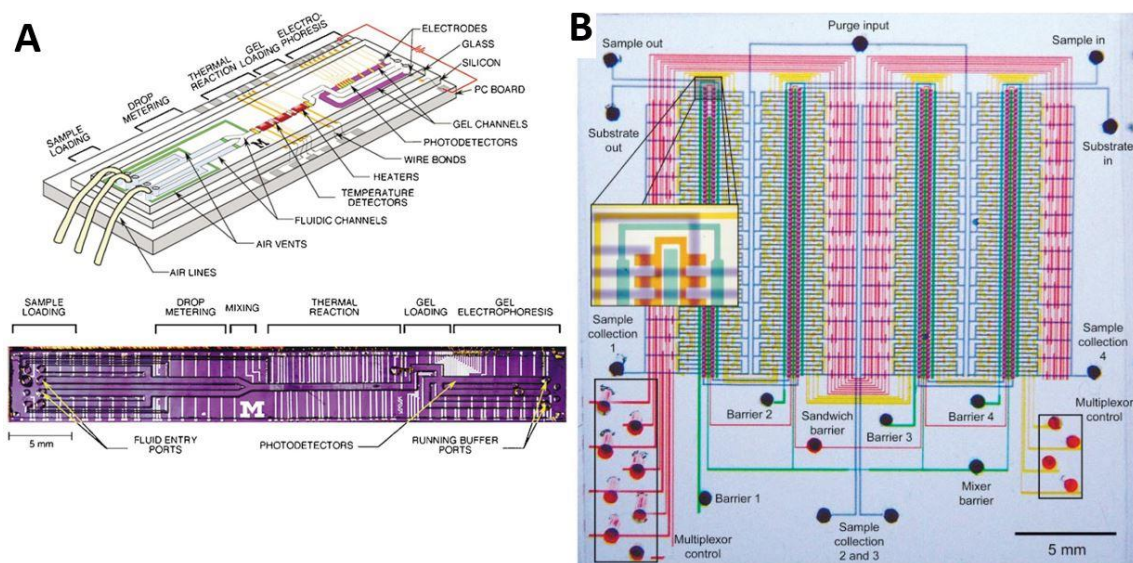
**List of Tables**

Table 2-1: Summary of the 3D printing techniques for microfluidic mold fabrication....	23
Table 2-2: Comparison of stereolithography and photolithography.....	26
Table 2-3: Printing parameters for green mold resin and clear channel resin .....	32
Table 2-4: Optimal design parameters for microfluidic molds printed with green master mold material .....	36
Table 2-5: Optimal design parameters for devices printed with the clear channel resin ..	44

## Chapter 1: Introduction

### 1.1 Microfluidic Lab-on-a-Chip Devices

Microfluidics are devices capable of utilizing fluid dynamics at the microscale to perform laboratory experiments. The use of microfluidics has exploded over the past few decades due to their versatility and the development of rapid prototyping [1]. The expansion of the use of microfluidics has led to the development of microfluidic lab-on-a-chip (LoC) devices where full laboratory experiments can take place on a single microfluidic chip as shown in Figure 1-1 [2]. The growth of the field of microfluidics can be attributed to their low cost, efficiency, versatility, and size.



**Figure 1-1:** Examples of microfluidic Lab-on-a-Chip (LoC) devices. (A) A microfluidic LoC device capable of performing nanoliter DNA analysis [3]. (B) A microfluidic

comparator chip capable of performing distinct biological assays. The channels are filled with dye for visualization [4]. Adapted from [2]

Due to the size and versatility of microfluidics, a specific type of microfluidic LoC, known as an organ-on-a-chip (OoC), has been developed as shown below in Figure 1-2. OoC devices create an *in vitro* environment in which cells can be cultured to mimic the function of a specific organ [5]. OoC microfluidics have been used to create models of human organs such as livers, kidneys, lungs, heart, etc. [6, 7]. After the establishment of OoC devices, the *in vitro* models have been used to study the mechanobiology of organ cells, test drugs for disease treatment, screening and diagnosis of diseases, organ-organ interactions, etc. [8-10].

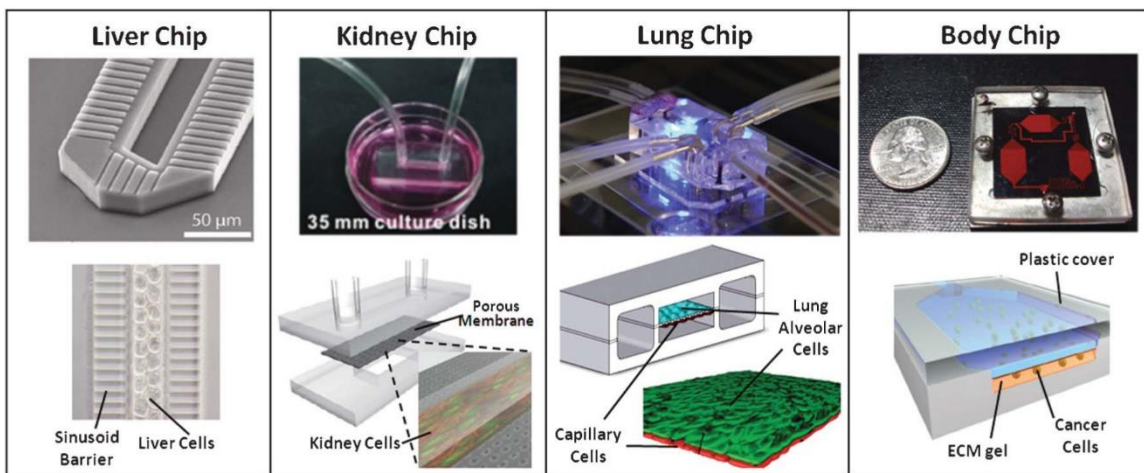


**Figure 1-2:** Examples of microfluidic Organ-on-a-chip (OoC) devices. The liver chip was designed to test the effects of shear stress on liver cell alignment [11]. The kidney chip was designed to understand how kidney cells filter urine [12]. The lung chip was

designed to understand the effects of tension on lung cells [13]. The body chip was designed to connect multiple different cell types [14]. Adapted from [6].

Microfluidic LoC devices have also started to have a direct impact on the patient healthcare industry with the development of microfluidic point-of-care (PoC) devices. Microfluidic PoC devices are diagnostic tools that can conduct simple medical tests for individual patients quickly and efficiently, even in low-resource areas [15]. Microfluidic PoC devices are capable of detecting diseases from saliva samples, detect biomarkers for cardiovascular disease, or perform advanced fluid handling techniques, such as droplet generation, mixing, etc. [16-18]. A PoC microfluidic device capable of testing for signs of diabetes and hyperlipidemia is shown below in Figure 1-3.

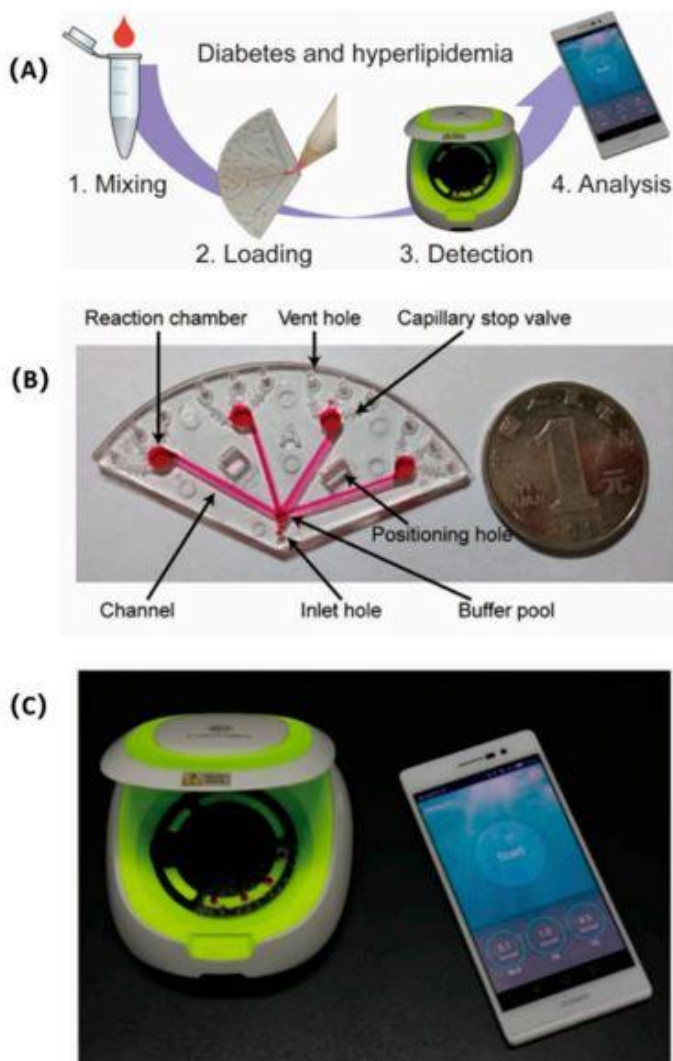


**Figure 1-3:** Point-of-Care microfluidic device capable of detecting signs of diabetes and hyperlipidemia. (A) Diagram showing steps of device usage. (B) The microfluidic component of the point-of-care device. (C) Packaging and data output component of the point-of-care device. Adapted from [19].

Overall, due to the versatility, ease of use, and size of microfluidic devices, their use has expanded across various areas of science and engineering. The development of

microfluidic LoC devices will enable faster experimentation and further expand the use of microfluidic devices.

## **1.2 Current Status and Limitations of Microfluidics**

Microfluidic technology has steadily been increasing in terms of both capability and usage since they were first developed over 30 years ago [20]. The development of rapid prototyping technology, using photolithography and polydimethylsiloxane (PDMS) soft lithography, was a major contributor to the widespread usage of microfluidics today [1].

Although microfluidics have become highly important in many areas of science and engineering due to their unique characteristics, microfluidics suffer from limitations, often relating to their fabrication. The development of rapid prototyping was a major step in microfluidics becoming mainstream, but microfluidic fabrication procedures still involve many challenges. Due to the complex, costly, and time-consuming fabrication procedures, the use of microfluidics remains limited and inaccessible for many applications in which their technology may prove revolutionary [21].

Currently, the major methods of fabricating microfluidic devices can be separated into the following categories: chemical processes, mechanical processes, and light-based processes [22, 23]. Chemical processes involve making a master mold by using chemicals to either add or remove material from a base substrate. The most popular chemical processes for microfluidic fabrication are wet etching, dry etching, and electrochemical discharge machining [24]. Mechanical processes involve fabricating molds by removing

material using mechanical forces. Common examples of mechanical processes for microfluidic mold fabrication are micro-milling, micro-cutting, and micro-grinding [24-26]. Light-based processes involve fabricating microfluidic molds through the solidification or removal of material by using lasers or LED light sources. The most common light-based techniques are photolithography and stereolithography 3D printing [27, 28].

Photolithography is the most widely used technique for fabricating molds for microfluidic devices. Photolithography involves coating a silicon wafer with a thin layer of photoresist, selectively solidifying portions of the photoresist using a UV light source and photomask, and removing excess photoresist using a developer as shown below in Figure 1-4 [1].

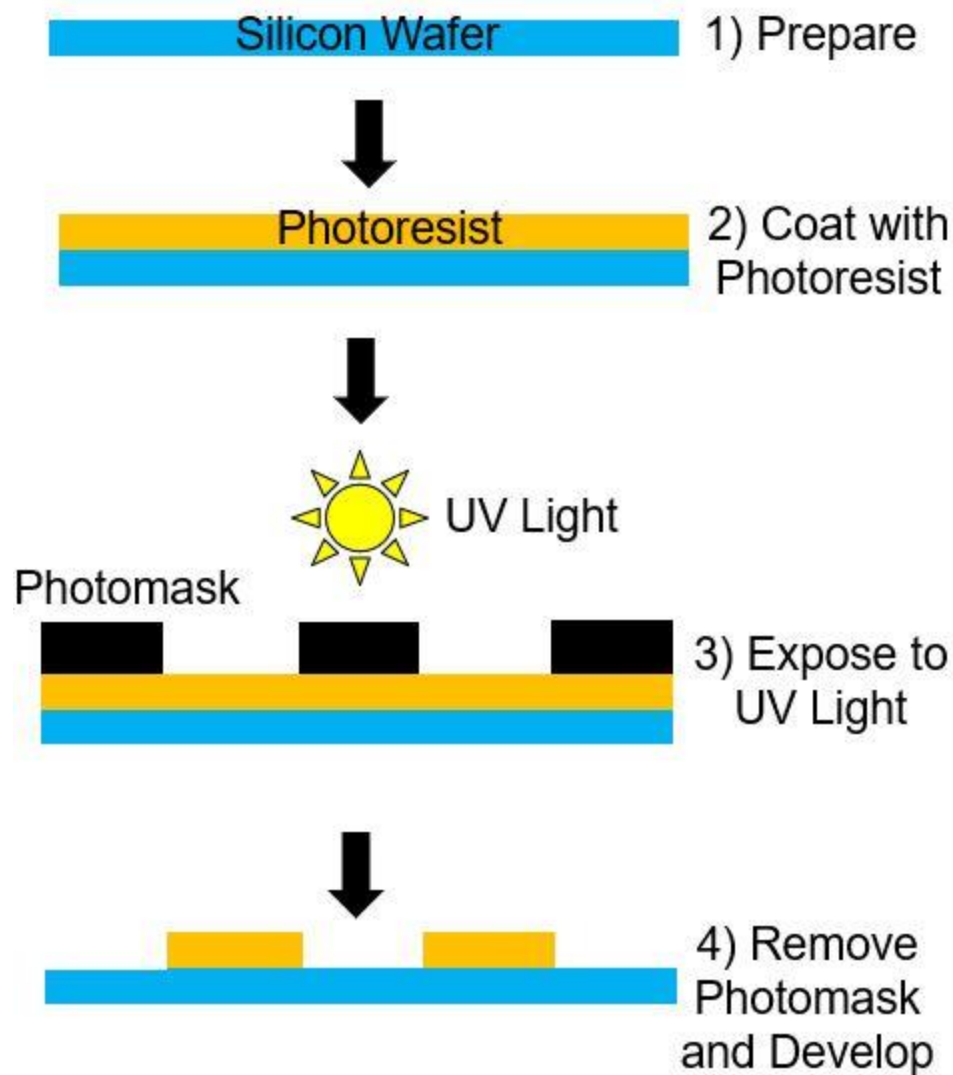


**Figure 1-4:** A schematic of the photolithography process for fabricating microfluidic molds. 1) Prepare a silicon wafer by cleaning the surface. 2) Coat the silicon wafer with a photoresist. 3) Selectively solidify portions of the photoresist using a photomask and UV light. 4) Remove excess photoresist with a developer.

Photolithography gained popularity within the field of microfluidics due to its ability to produce features in the size range of a few nanometers to hundreds of microns [29]. Additionally, photolithography is relatively fast compared to many of the other microfluidic fabrication methods.

Although photolithography has gained popularity amongst the microfluidic community, new microfluidic fabrication techniques are still being developed to overcome the limitations of photolithography. Some of the common downsides of photolithography are that it requires an array of expensive equipment, extensive training on the fabrication procedure, it is usually conducted within a clean room, it has low design flexibility when design changes are needed, it can only create planar two-dimensional (2D) channels, it has a high probability of defects affecting the performance of the mold, and the molds are brittle and easily broken. The limitations of photolithography affect both the use and the accessibility of the technology.

To overcome the limitations of photolithography, stereolithography 3D printing has become an alternative method for fabricating both microfluidic molds and microfluidic devices directly [30]. Stereolithography 3D printing works by lowering a plate on which the model will be printed, known as the build plate, into a vat of resin. Then a single layer of the object will be solidified by exposing specific portions of the resin using UV light. The build plate will then reposition itself, and the process will be repeated until the object has been printed [31]. Stereolithography is later discussed in depth in Chapter 2.

Stereolithography 3D printing of microfluidic molds has made microfluidic technology more accessible. Additionally, when compared to photolithography, the cost

of fabricating molds is cheaper, fabrication times are shorter, less training is required, design flexibility is increased, and 3D geometries can be printed. As such, 3D printing has become a very attractive technology for microfluidic fabrication.

### **1.3 Modular Microfluidic Platforms**

Even with the advances in microfluidic fabrication technology, there are still limitations of microfluidic LoC or OoC devices due to the nature of single-chip microfluidics [32]. When entire components of an experimental setup are configured on a single chip, if a portion of the chip fails or breaks, the entire experiment is compromised. Additionally, if a specific aspect of the experiment needs to be reconfigured, a completely new microfluidic mold and microfluidic device may be needed. After a LoC or OoC device has been used, it may not be possible or suitable to prepare the device for multiple uses. Thus, single-use LoC or OoC devices may suffer from higher costs and more complex experiment setup than originally proposed.

To overcome the limitations of LoC and OoC devices, multi-chip modular platforms have been developed. The field of modular multi-chip microfluidic platforms has exploded into its own research subcategory [33, 34]. Multi-chip microfluidic LoC platforms are microfluidics LoC devices where each function, or groups of functions, are separated onto different modules. Each module can then be connected to each other through a base platform to function as a single experimental setup as shown below in Figure 1-5.

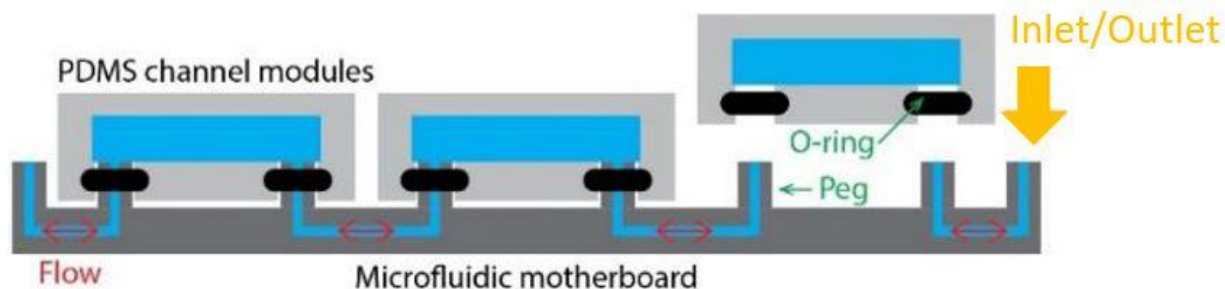


**Figure 1-5:** A schematic of a modular microfluidic platform. PDMS channel modules with specific functions can be connected through a microfluidic motherboard. Adapted from [35].

Microfluidic modules have been developed that can serve as pumps, fluidic reservoirs, uni-directional valves, tunable mixers, microdroplet generators, etc. [36, 37]. Many different methods to connect modules have also been developed. Some examples of connection types are embedded O-rings, magnetic fixtures, and lego-like stacking of modules [38-40]. Examples of the connections are shown below in Figure 1-6.

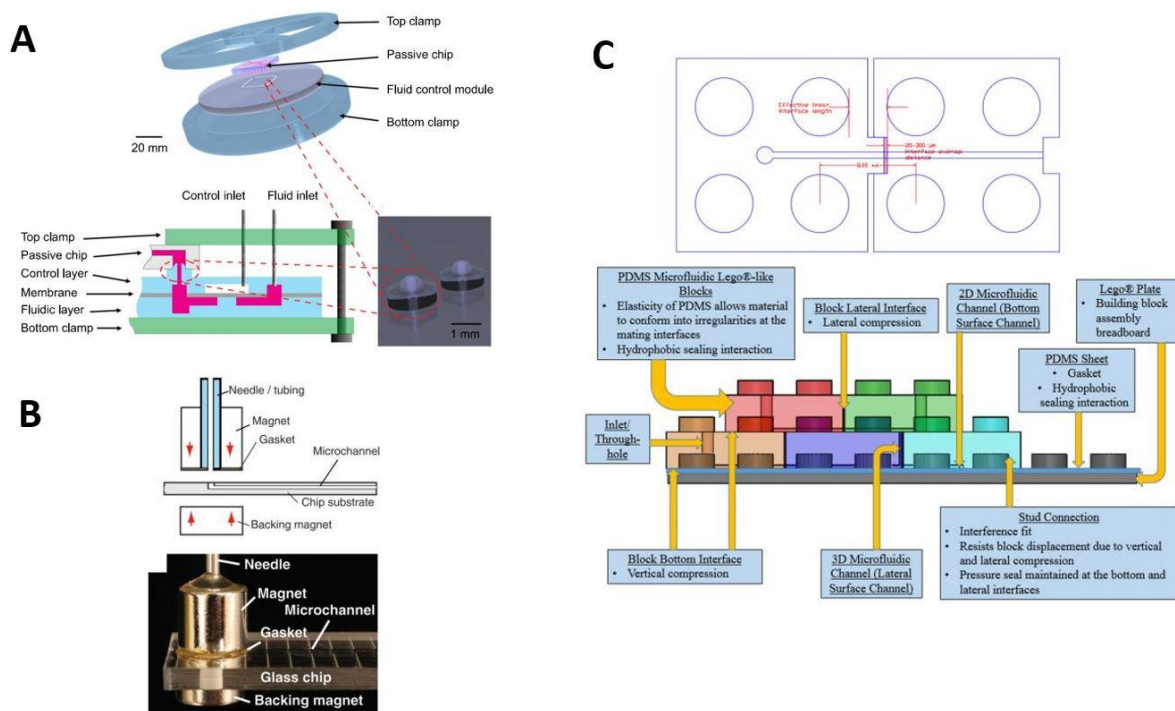


**Figure 1-6:** Examples of connection mechanisms between microfluidic modules. (A) Connection between modules is achieved with PDMS O-rings. Adapted from [39]. (B) Connection between modules is achieved by applying pressure through magnets. Adapted from [38]. (C) Connection is achieved through a Lego-like connection. Adapted from [40].

Modular microfluidic platforms have been used to improve the design of microfluidic systems, increase experimental parallelization, extend the length of microfluidic channels, increase control over a microfluidic system, and allow for reconfiguration of experimental setups [33].

Similar to microfluidic devices, modular platforms typically implement photolithography for fabrication. As such, modular microfluidic platforms face similar

limitations to microfluidic LoC devices such as their cost, time for fabrication, and design inflexibility. Another limitation of modular microfluidic platforms includes standardization of their connectors across the field of microfluidics. Due to the limitations of fabricating modular platforms, 3D printing is an attractive alternative to photolithography for fabricating microfluidic motherboards due to its unique characteristics of design flexibility, speed, and low cost. Additionally, by using 3D printing, it may be possible to increase the standardization through its ability to produce three-dimensional geometries.

#### **1.4 Previous Studies**

Due to the relevance of microfluidics for cellular studies, microfluidics are well-suited for the field of cellular mechanobiology. Cellular mechanobiology, or the way the biology of a cell is affected by mechanical stimulation, is an emerging sector of biomedical engineering with the potential to reshape our thinking of medical treatment. Cells respond to mechanical stimulation by modulating extracellular matrix synthesis, increasing proliferation, promoting gene expression, releasing biomolecules, etc. [41-44]. By understanding the responses of cells to mechanical stimulation, the causation of specific diseases, such as osteoporosis or myocardial infarction, can be understood and new treatments can be developed [45, 46]. Therefore, our group previously developed a microfluidic cell compression device [47, 48].

The device was able to apply regulated levels of compressive stress to chondrocytes suspended within a hydrogel scaffold and is shown below in Figure 1-7.

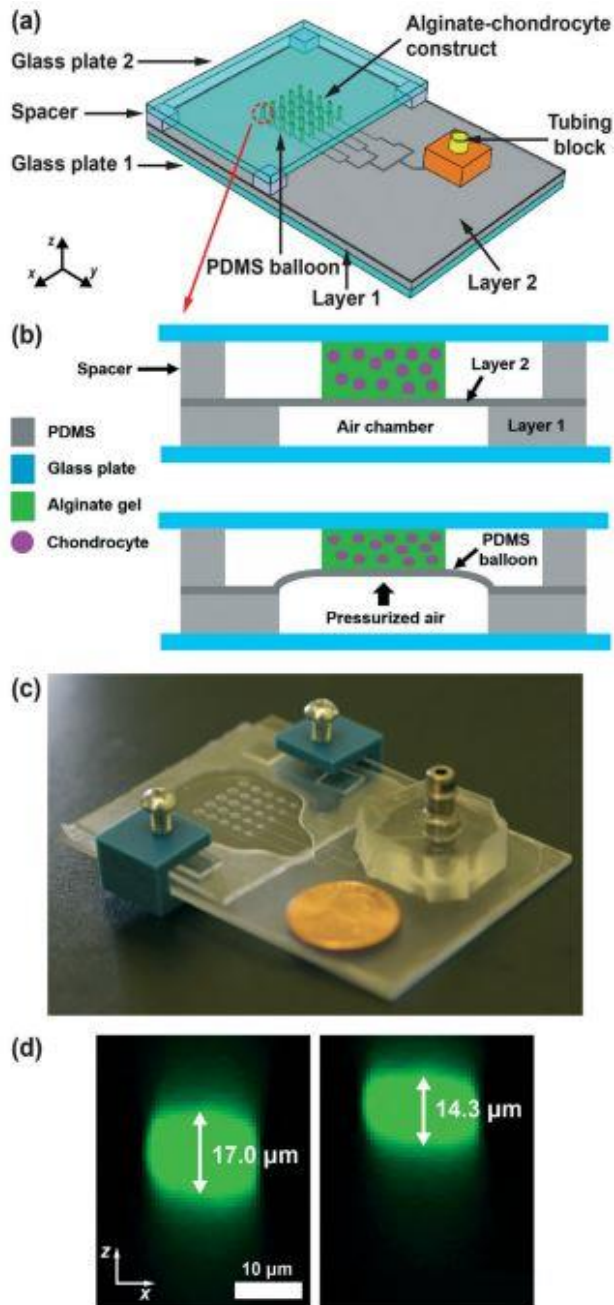


**Figure 1-7:** Schematic of microfluidic cell compression device fabricated using photolithography and soft lithography. (A) Isometric view of the device. It has an array of balloons with diameters of 1.2, 1.4, 1.6, 1.8, and 2.0 mm. (B) Side-view of the device showing the various layers of fabrication. (C) Image of the fabricated device. (D)

Microscopy images of chondrocytes experiencing compression upon balloon inflation.  
Adapted from [48].

The device consisted of multiple layers. From bottom to top it had a glass plate, a microchannel layer (Layer 1), a balloon layer (Layer 2), a layer for chondrocytes suspended within hydrogel, and an upper glass plate. The microchannel layer and balloon layer consisted of an inlet, microchannels, and an array of air chambers with a thin layer of flexible PDMS suspended above them. The thin layer of PDMS above the air chambers would deform when the air chamber was pressurized, similar to a balloon. As such, they become known as the balloons of the device. The device had a 5 by 5 array of balloons with diameters of 1.2, 1.4, 1.6, 1.8, and 2.0 mm.

To characterize the performance of the device, confocal laser scanning microscopy was used to measure the height to which a pressurized balloon on the device would inflate (hereinafter balloon height). It was found that under a constant applied pressure, as balloon diameter increased, balloon height also increased as shown below in Figure 1-8.

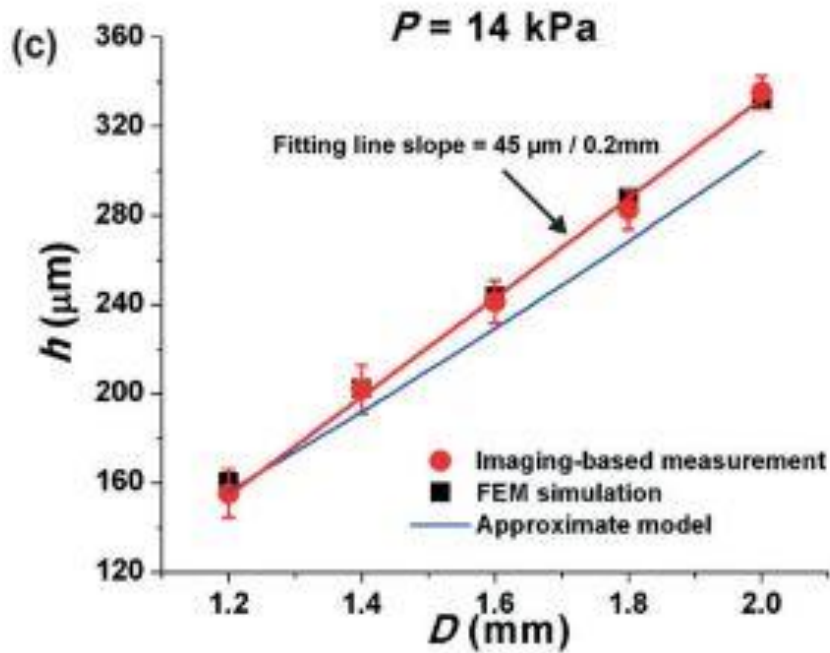


**Figure 1-8:** The balloon heights of the above cell compression device when subjected to 14 kPa of pressure. The red line represents data obtained through confocal laser scanning microscopy, and the blue line represents an approximate model developed (Equation 4-1). Adapted from [48].

Overall, it was shown that the cell compression device fabricated with photolithography was capable of applying compressive stress to cells by compressing the cells between the balloons of the device and an upper glass plate. Although the device was successful, it suffered the following limitations. Because photolithography was used to create the device, fabricating the device was complex and time consuming. Additionally, the device was only capable of applying compression to cells. As such, the work presented in this thesis aims to improve upon the cell compression microfluidic fabricated with photolithography by improving the fabrication methods, further

characterizing the device, and adding additional components to the cell compressor to allow it to function as an active mixing microfluidic.

### 1.5 Mixing in Microchannels

It is well known that mixing in a microchannel is limited due to viscous forces dominating the flow. The Reynolds number ( $Re$ ) can be used to describe the inertial effects of the flow compared to the viscous effects of the flow as shown below [49].

$$Re = \frac{uL}{\nu}, \quad (1-1)$$

where  $u$  is the average velocity of the flow,  $L$  is the characteristic length scale of the flow, and  $\nu$  is the kinematic viscosity of the working fluid. When Reynolds number is low, viscous forces are dominant. In microchannels,  $Re$  is typically very low due to the small velocities and characteristic length scales.

Mixing typically occurs from two sources, diffusion and advection. Diffusion is the net movement of particles from an area of high concentration to an area of low concentration. Advection is the bulk movement of the fluid. Typically, advection is the main cause of mixing at short time scales for fluid flow. At microscales, the inertial forces are limited, and viscous effects become dominant, meaning advection is limited. A dimensionless number known as the Peclet number ( $Pe$ ) can be used to quantify the mixing in a microchannel as shown below [50].

$$Pe = \frac{uL}{D}, \quad (1-2)$$

where  $u$  is the bulk velocity of the flow,  $L$  is the characteristic length scale of the flow, and  $D$  is the coefficient of diffusion. High  $Pe$  indicates that advection is dominant, and mixing is more efficient. Low  $Pe$  indicates that diffusion is dominant, and mixing is less efficient. Typically, the  $Pe$  for microchannel flow is relatively small. Therefore, if mixing in a LoC microfluidic is desired, special components must be designed to promote complete mixing.

In this study, the microfluidic cell compression device developed previously was adapted into a microfluidic mixing module due to its relative ease of use. Additionally, to achieve dynamic inflation of the balloons, it requires limited equipment. In the active mixer, flow was generated above the balloons of the device. The flow above the PDMS balloons was mixed by dynamic motion of the balloons. The dynamic motion of the balloon locally increased the  $Pe$  number, which mixed two samples via advection.

## **1.6 Purpose of This Study**

In this study, we aim to develop a multi-use modular microfluidic platform using 3D printing for applications in active mixing, lab-on-a-chip development, and cell mechanobiology research as shown in Figure 1-9.

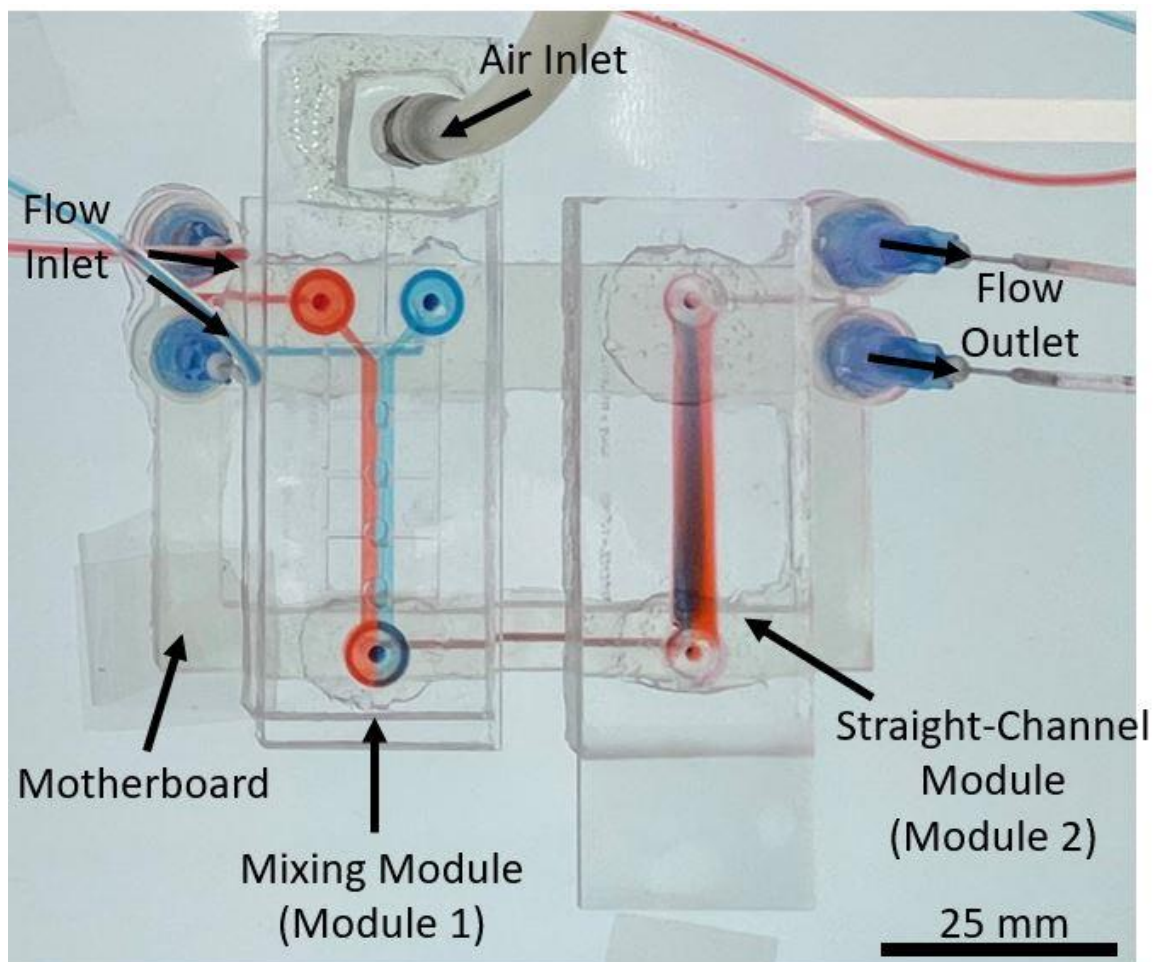


**Figure 1-9:** An image of the microfluidic motherboard, mixing module, and straight-channel module developed in this study. Red dye water and blue dye water flow into the motherboard separately before being mixed in the mixing module (module 1). Next the mixed dyes flow into the straight-channel module (module 2). The air inlet is used to control the balloons of the mixing module. In this image, the balloons had not been actuated to show samples before mixing.

To develop a multi-use microfluidic platform using 3D printing, the working conditions of the 3D printer first needed to be established for printing both microfluidic

molds and microfluidic devices (Chapter 2). A procedure to process the printed parts was also developed that was compatible with PDMS soft lithography.

Next, the microfluidic balloon device was redesigned to be compatible with the 3D printer, to have the ability to actively mix a flow, and to be compatible with a microfluidic motherboard platform. The size of the device, the number of balloons, and the balloon diameters were changed to enable compatibility with the 3D printer and the microfluidic motherboard. Additionally, a flow channel microfluidic was added above the balloons to enable fluid flow above the balloons (Chapter 3).

A microfluidic motherboard was also designed which was compatible with the microfluidic modules to improve the functionality of the microfluidic device developed previously (Chapter 3). The connection between the motherboard and modules was completely integrated into the design of the motherboard, and modules, and did not require any additional components. The motherboard was designed to allow for two modules to be connected in series, and for two samples to be injected separately. The functionality of the motherboard could easily be changed by updating its design within a computer aided design (CAD) software.

The response of the height of the balloons to an applied pressure was measured using an updated balloon height characterization method that was quicker and cheaper than the previous method (Chapter 4). Inverted brightfield microscopy was used to measure the balloon diameter and balloon height in place of 3D laser scanning confocal microscopy.

Next, the flow through a straight-channel microfluidic was measured using particle image velocimetry (PTV). PTV is a method of measuring the velocity field of a flow by seeding tracer particles into the flow, imaging the particles, and tracking the change of position of the particles over time. PTV will be explained further in Chapter 5. The PTV measurements of the flow through a straight-channel module was used to estimate the level of shear stress cells within the module would experience.

Then, the microfluidic motherboard, balloon module, and straight-channel module were combined to perform an experiment to test the mixing efficiency of the balloon module under varying frequencies of balloon inflation (Chapter 6). A hypothetical cell mechanobiology study was envisioned where two liquids would be mixed in a balloon module connected to the first slot of the motherboard, then the mixed solution would apply shear stress to cells cultured in a straight-channel module connected to the second slot of the motherboard. Finally, the results from this study are summarized (Chapter 7), and prospective research directions are suggested.

## **Chapter 2: 3D Printing Microfluidics**

### **2.1 3D Printing for Microfluidic Fabrication**

Microfluidic device fabrication techniques have evolved rapidly since their initial development. Initial versions of microfluidic devices were fabricated using complex methods based on modifying, or building upon, a silicon wafer [20]. As the field of microfluidics began to mature, a new method combining photolithography and PDMS soft lithography, enabled rapid prototyping of microfluidic devices [1]. Rapid prototyping was accomplished by casting polydimethylsiloxane (PDMS) into a mold fabricated with photolithography. Although these methods are well established, common methods, such as photolithography or etching, are expensive, require specialized training, are time consuming, and are highly sensitive to defects.

Due to the limitations of silicon wafer based microfluidic fabrication techniques, 3D printing was employed as an alternative with the following benefits. First, 3D printing allows for greater design flexibility as three-dimensional (3D) designs are possible and easy to fabricate. Designs can also easily be modified for improvement. Second, 3D printing is cheaper and more accessible. Third, 3D printing can print both master molds for soft lithography and microfluidic devices directly. Fourth, 3D printing is less sensitive to the environment and defects during fabrication. Fifth, 3D printed microfluidic molds are more durable and less brittle than molds made with silicon wafers. Overall, 3D printing has made microfluidics accessible to a wider array of fields of science and, as such, the field of microfluidics is expanding [51].

Within the field of 3D printed microfluidics, there are many different methods of 3D printing which use many different materials [52]. These methods are summarized

below in Table 2-1. Binder jetting printing builds 3D architectures by depositing material via droplets onto a base structure and binding the material using adhesives. Photopolymer jetting printing is similar to inkjet printing where droplets are deposited on a base structure and solidified with UV light [53]. Wax printing applies a thin layer of wax onto a substrate to create a hydrophobic barrier which can be used to create microchannels [54]. Xerography uses a cutting plotter to cut lamination pouches to a desired shape. Then thermal lamination is used to build the mold layer by layer. Fused deposition modeling melts solid filament and then extrudes the filament through a nozzle to apply material to a base structure [55]. Laser sintering and electron beam melting utilizes a laser or electron beam respectively, to selectively melt plastic to create 3D structures [56, 57]. Although many techniques can be used to 3D print microfluidic molds and devices, stereolithography is the most common.

**Table 2-1:** Summary of the 3D printing techniques for microfluidic mold fabrication

Printing Technique	Overview [54, 52, 51]	Resolution [52, 58, 59, 55-57, 60, 53]
Stereolithography	Vat of polymer resin solidification through UV light	5 – 200 $\mu\text{m}$
Ink jetting	Droplets applied to a surface layer by layer	60 $\mu\text{m}$
Photopolymer jetting	Photoresistive droplets applied to a surface and exposed to UV light	10 $\mu\text{m}$
Wax printing	Create hydrophobic barrier as microchannel	~ 300 $\mu\text{m}$
Xerography	Cutting and thermal bonding of thermally reactive polymer	75 – 200 $\mu\text{m}$
Fused deposition modeling	Heating and extrusion of solid filament	400 – 600 $\mu\text{m}$
Laser sintering	Melting and cooling of plastic particles with a laser beam	20 – 100 nm
Electron beam melting	Melting and cooling of plastic particles with an electron beam	200 nm

A schematic figure of the stereolithography 3D printer used in this study is shown below in Figure 2-1. Stereolithography works by lowering a plate on which the model will be printed, known as a build plate, into a vat of negative photoresist. The build plate will move itself towards the UV light source and position itself at a specified distance from the light source to control the layer height. Once in position, the light source will

turn on to solidify a single layer of photoresist in the pattern specified by the 3D slice file. Once solidified, the light will turn off and the build plate will reposition itself to create the next layer. This will be repeated until the part is printed [31].

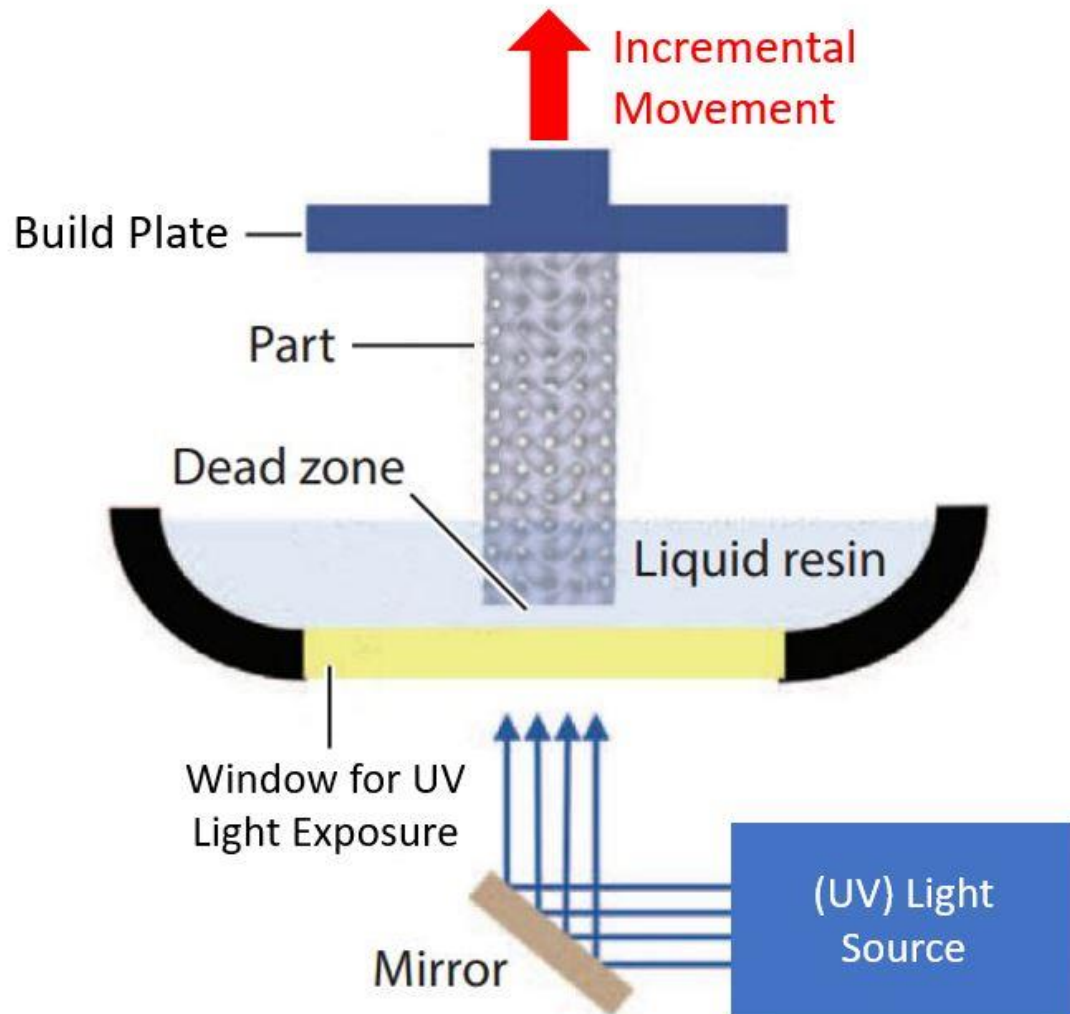


**Figure 2-1:** Schematic of a stereolithography 3D printer where the 3D printed object is fabricated on the build plate by exposing photosensitive resin to UV light. The build plate

incrementally moves upward between each solidified layer with a step size equal to the layer thickness. Reproduced from [61].

Although microfluidic fabrication with stereolithography 3D printing has many advantages, it suffers from limitations like any other technology. Compared to stereolithography, photolithography-based techniques have the following benefits. First, photolithography has a greater resolution compared to 3D printing. Typical microfluidic 3D printers have a lateral resolution of 30  $\mu\text{m}$  to 50  $\mu\text{m}$ , whereas photolithography can have lateral resolutions as small as 15 nm [29]. Second, photolithography uses spin-coating to control the channel height. As such, smaller minimum channel heights can be achieved. The minimum channel height of stereolithography 3D printing is around 5  $\mu\text{m}$ , whereas photolithography can have channel heights as low as 15 nm [58, 29]. Third, photolithography molds are smoother and have a lower surface roughness. A summary of the comparison between stereolithography and photolithography are shown in Table 2-2.

**Table 2-2:** Comparison of stereolithography and photolithography for microfluidic mold fabrication

Characteristic	Stereolithography 3D Printing [58, 62, 63]	Photolithography [29, 64, 27]
Resolution	5 – 200 $\mu\text{m}$	15 nm – 7 $\mu\text{m}$
Cost per mold	\$5 - \$7	> \$100
Fabrication time	2 - 4 hours	1 – 2 weeks
Design flexibility	Easy design changes with CAD software	Limited due to photomask requirements
3-Dimensional channels	Mold height variability	Planar material solidification
Surface roughness	1 – 3.5 $\mu\text{m}$	0.3 - 3 nm
Defect probability	Low	High

Throughout this thesis, a stereolithography 3D printer was used to fabricate not only microfluidic molds for use with PDMS soft lithography, but also to directly print microfluidic devices. A CADWorks3D MiiCraft Ultra 100 series printer was used for both types of printing. When printing microfluidic molds, a green photosensitive polymer resin, master mold resin (hereinafter, the green mold resin) was used. When printing microfluidic devices, a clear photosensitive polymer resin (hereinafter, the clear channel resin), BV-007 clear, was used. Figure 2-2 shows images of devices printed with the green mold and clear channel resins. The 3D printer had a minimum lateral resolution of 53  $\mu\text{m}$ , a minimum vertical resolution of 30  $\mu\text{m}$ , a build area of 102 mm by 57.5 mm by 120 mm, and operated at wavelengths between 365 nm and 405 nm [58].

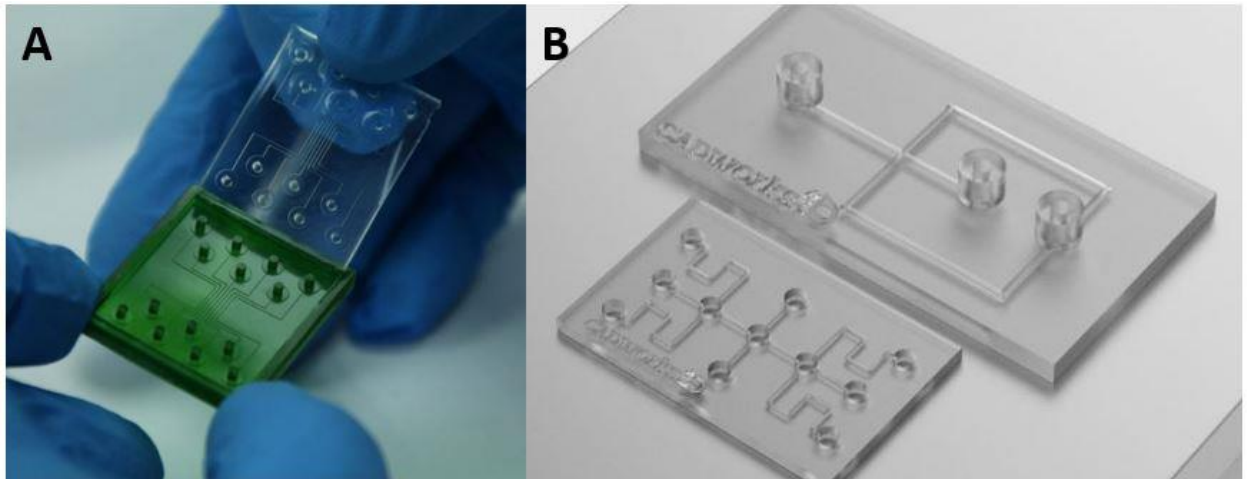


**Figure 2-2:** (A) Image of a 3D printed microfluidic mold for used with soft lithography printed with green mold resin. Cured PDMS is being peeled from the mold. (B) Image of two 3D printed microfluidic devices printed with clear channel resin. Images reproduced from [65].

## 2.2 3D Printer Maintenance and Preparation<sup>1</sup>

To produce 3D printed molds for microfluidic devices, the 3D printer must be properly maintained, prepared, and cleaned regularly. Failure to maintain and prepare the printer will result in mold defects, PDMS cure inhibition, and possibly damage to the printer [62]. The anatomy of the 3D printer used in this study is shown below in Figure 2-3.

<sup>1</sup> Published in the American Society of Mechanical Engineers (ASME) Fluids Engineering Division Summer Meeting 2022 (FEDSM) conference. C. Emeigh, H. Zhang, and S. Ryu, 2022, Fabrication of a microfluidic cell compressor using a 3D-printed mold, ASME FEDSM 2022-87613.

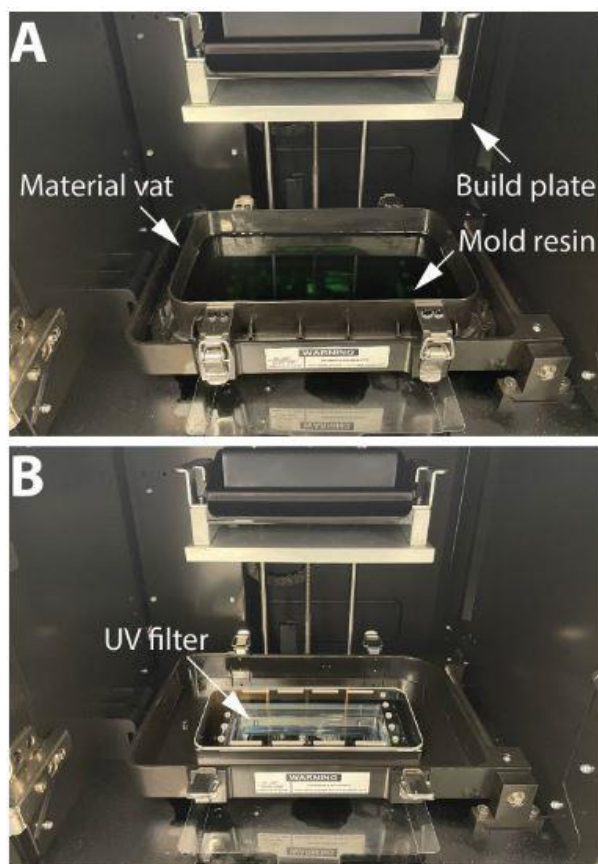


**Figure 2-3:** Microfluidic 3D printer (MiiCraft Ultra 100 Series, CreativeCADWorks) used to fabricate devices in this study. (A) The material vat with resin (green liquid) and the build plate. (B) The UV filter is located below the material vat. Originally published in [62].

To properly care for the printer, multiple considerations must be taken. First, after printing, the 3D printer build plate must be washed by using only IPA, hot water, and gloves. Using paper towels or Kim wipes on the build plate may scratch the build plate and introduce particulate into the resin during the next print. Green mold resin contaminated with particles may result in poor printability and molds unable to cure

PDMS. Additionally, the resin should be stirred gently using a gloved finger to homogenize the resin before printing. After mixing, the resin needs to be left for approximately 20 minutes to allow air bubbles within the resin to dissipate.

Second, using the printer for an extended period will result in partially cured resin accumulating in the material vat and clouding of the bottom Teflon film. Accumulation of partially cured resin is due to the scatter of UV light as it passes through the resin to the build plate. The scattered UV light will solidify undesired regions of the resin. This is minimized by the resins photo-absorber, but it cannot be prevented. Although the effect is small during UV exposure of each layer, after many prints, the partially cured resin will absorb UV light before it can reach the build plate. Additionally, the Teflon film will begin to cloud due to exposure of UV light, absorbing or distorting the light before it can reach the resin. Both may result in poor printability and molds incapable of curing PDMS. The printer resin and Teflon film were changed when either the prints would inhibit PDMS curing or when resolution and channel definition became unsatisfactory.

If servicing of the printer is needed due to the lack of transparency of the Teflon film or partially cured resin, the following steps should be taken. (1) The material vat should be removed from the printer. (2) The remaining resin in the printer should be poured into a separate container. The printer manufacturer suggests that filtering the material with a fine particle filter may render the resin usable again. The container should either be one of the empty containers that the resin came in or glass. The resin will corrode certain types of plastic. (3) The material vat should be placed upside down and the placement of the brackets should be noted. (4) The material vat should be unscrewed and disassembled. (5) The body of the material vat, the lower plate of the material vat,

and the O-ring should be cleaned with hot water and gloves. IPA may be used to clean the body and the lower plate of the material vat. (6) All parts of the material vat should be dried with compressed nitrogen. (7) The Teflon film must be replaced with a new one. The Teflon film may be cleaned using dish soap and hot water if the main problem was partially cured resin, but this is a temporary solution and not advised. (8) The material vat may be reassembled, placed into the printer, and new resin can be added. After these steps, the material vat is ready for printing.

To maintain the printer, another consideration that must be taken is that the UV glass may accumulate oils or be scratched during printing. The source of the oil buildup is unconfirmed, but it may be due to the contact between the UV glass and the Teflon film. Oil on the UV glass may absorb or refract UV light during printing. To clean the UV glass, hot water, dish soap, and gloves are effective. Begin by wetting the UV glass to loosen debris and prevent scratching. Then, apply a small amount of dish soap directly to the glass. Using a wet, clean glove spread the soap across the glass to further loosen any debris and ensure all built-up oils will be removed. Finally, rinse the glass with hot water and dry with compressed nitrogen.

By following these steps to maintain and prepare the 3D printer, the printer is capable of producing high quality microfluidic molds compatible with PDMS. Failure to properly care for the printer will result in print defects, the mold's inability to cure PDMS, and possibly damage to parts of the printer. If after maintaining the printer, it still has issues with resolution and printing small channel features, the layer exposure time can be increased up to a maximum of 4.5 seconds. This will cause the resin to decay within the material vat faster, but it can be an effective solution. Reducing the amount of

resin in the material vat at any given time can reduce waste and prevent the effects from the scattered light.

### **2.3 Printing Parameters and Effects on Final Print**

When using the 3D printer, multiple parameters may be changed that will affect the final 3D object that is printed. Through the printing software (MiiController, MiiCraft), it is possible to change various features of the print, but the most important parameters are layer thickness, layer curing time, number of base layers, base layer curing time, and the number of buffer layers. Each of these aspects and their effects on the final printed part will be discussed in this section. A summary of the printing parameters and their effects on each resin type is shown below in Table 2-3.

**Table 2-3:** Printing parameters for green mold resin and clear channel resin. Optimal values are shown in bold.

Printing Parameter	Effect on Printed Part	Green Mold Resin	Clear Channel Resin
Layer Thickness	Changes resolution, speed, print quality	<b>30 <math>\mu\text{m}</math></b> – 50 $\mu\text{m}$	<b>30 <math>\mu\text{m}</math></b> – 50 $\mu\text{m}$
Layer Curing Time	Changes channel feature definition, speed, resolution, and lifespan of resin	3.5 sec – <b>4.5 sec</b>	<b>0.9 sec</b> – 1.0 sec
Number of Base Layers	Affects adhesion to the build plate, defects related to adhesion	<b>1 layer</b> – 3 layers	<b>1 layer</b> – 3 layers
Base Layer Curing Time	Affects adhesion to the build plate	<b>50 sec</b> – 60 sec	<b>25 sec</b> – 30 sec
Number of Buffer Layers	Affects adhesion to the build plate	2	2

The layer thickness chosen for printing will determine the resolution, speed, and overall quality of the printed object. The layer thickness refers to the thickness of the resin that is solidified for each slice of the printed object. The printer used in this study is capable of printing in layer thicknesses of 30  $\mu\text{m}$  and 50  $\mu\text{m}$ . When choosing what layer thickness to use, one must decide whether speed or final print quality is most important. Small layer thickness will result in longer printing times with higher quality due to a higher resolution, and larger layer thickness will produce faster prints with lower quality. Typically, when printing either microfluidic molds or microfluidic devices, it is

beneficial to keep the layer thickness as small as possible to ensure that all channel features are printed accurately and completely. For the creation of microfluidic molds and motherboards in this thesis, the smallest layer thickness of 30  $\mu\text{m}$  was used.

Layer curing time is an equally important parameter. The layer curing time refers to the amount of time each slice of the object is exposed to UV light. When choosing what layer curing time to use, one must decide whether speed, definition of channel features, resolution of the printer, or preservation of the printer resin is most important. When printing microfluidic molds or channels, the channel feature definition and resolution of the printer are the most important considerations. When increasing the layer curing time, the channel features become more defined, but the resin is prone to over solidification, slightly reducing the tolerance of the printer. Additionally, increasing the layer curing time will reduce the speed of the print and may reduce the life of the resin in the printer due to UV light scatter into the material vat. High layer curing times may result in the printed part becoming detached from the build-plate due to bonding between the freshly printed layer and the bottom of the material vat. The printer manufacturer recommends that the layer curing time be kept between 3.5 seconds to 4.5 seconds for the green mold resin and 0.9 seconds to 1 second for the clear channel resin. For the creation of molds and motherboards fabricated in this thesis, a layer curing time of 4.5 seconds was used for the green mold resin and 0.9 seconds for the clear channel resin.

The number of base layers, base layer curing time, and number of buffer layers will affect how well the printed object sticks to the build-plate, as well as if it will have any defects from the contact with the build-plate. The number of base layers refers to how many layers are printed before the desired object is started. The base layer curing

time is the amount of time each base layer is exposed to UV light. The number of buffer layers is the number of layers between the base layer and the printed object. These base layers are printed to ensure strong bonding between the build-plate and the printed object. Typically, the number of base layers was left at its default value of 1 for both resin types but was increased if a print failed due to poor attachment to the build-plate. The base layer curing time was also left at its default value of 50 seconds for the green mold resin and 25 seconds for the clear channel resin but was increased by 5 seconds if poor adhesion occurred during part printing. The number of buffer layers was left at its default value of two and was never changed.

#### **2.4 Design and Fabrication Consideration for Green Mold Resin**

When developing green molds for microfluidic fabrication, the following design and fabrication flow should be followed as shown on the left side in Figure 2-4. To produce high quality microfluidic device molds compatible with PDMS soft lithography, the molds must be designed to be compatible with the 3D printer and the proper processing procedure must be implemented. In this section, the processing procedure for the green mold resin will be discussed. The processing procedure for the clear channel resin will be discussed in Chapter 2.5.

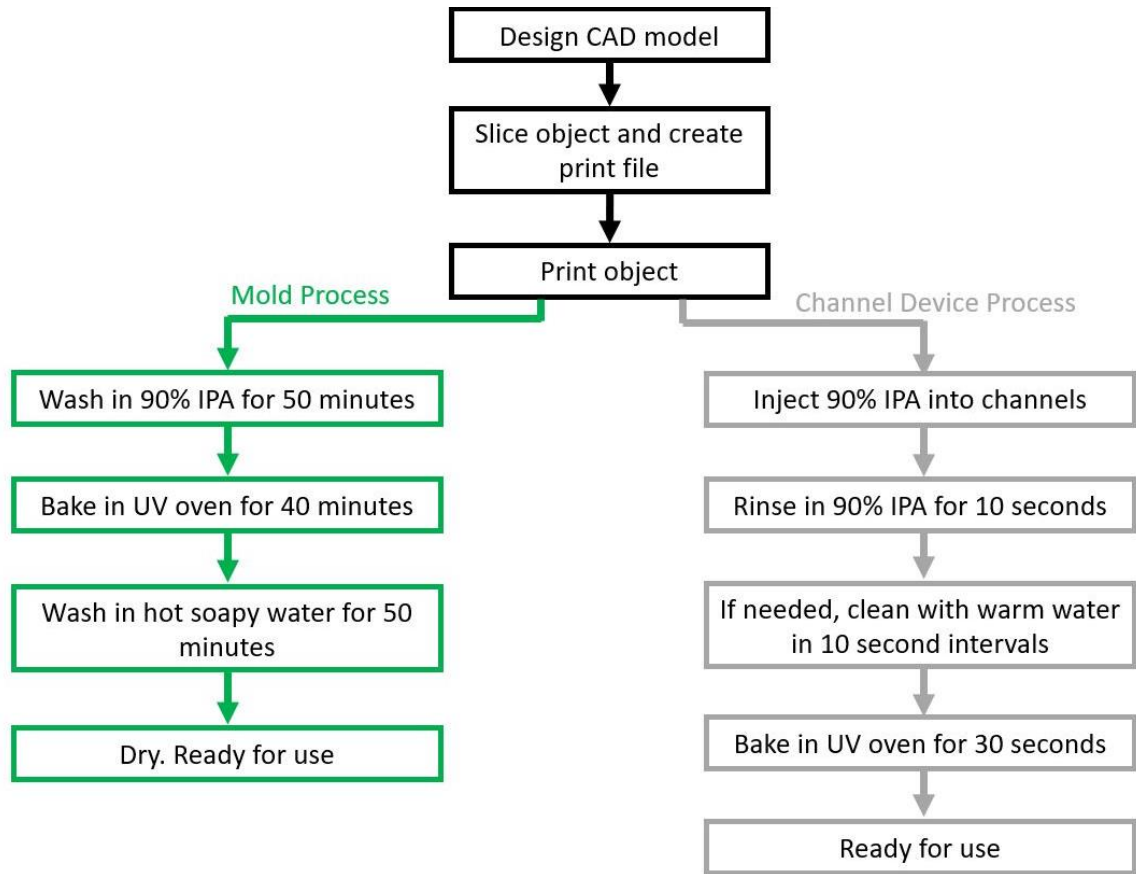


**Figure 2-4:** Flowchart of the fabrication procedure for microfluidic molds and microfluidic devices. The procedure to print and process microfluidic molds with green mold resin for use with soft lithography is shown in green (left), and the procedure to print and process microfluidic devices with clear channel resin for direct usage is shown in gray (right). Steps common to both procedures are shown in black (center). Adapted from [35].

#### 2.4.1 Design Considerations for Increasing Printability of Green Resin Molds

To improve the quality of the 3D printed microfluidic device molds using the green mold resin, the following design considerations must be taken. Failure to design a

device compatible with the 3D printer's capability may result in unusable microfluidic device molds. The height and width of the channel features, the spacer heights, the features to control device thickness and curvature, and the base layer thickness must be considered. The ideal mold parameters for use with mold design are summarized below in Table 2-4.

**Table 2-4:** Optimal design parameters for microfluidic molds printed with green master mold material.

Design Parameter	Optimal Choice
Channel Height	Multiple of 30 $\mu\text{m}$
Channel Width	Multiple of 53 $\mu\text{m}$
Features for Thickness and Curvature Control	Spacers and Wall Along Mold Edge
Base Layer Thickness	1 mm – 2 mm

When choosing the channel heights, widths, and spacer heights, it is important to consider the minimum vertical and lateral resolution of the 3D printer. The 3D printer has a minimum vertical and lateral resolution of 30  $\mu\text{m}$  and 53  $\mu\text{m}$ , respectively. One should design their microfluidic mold such that the features conform to the minimum resolution of the 3D printer (e.g. 30  $\mu\text{m}$ , 60  $\mu\text{m}$ , 90  $\mu\text{m}$ , etc.). Additionally, larger features typically print with a higher feature definition. In this study, it was found that the minimum channel height that could reliably be printed was 120  $\mu\text{m}$ , and that wider and taller channels would print with fewer problems.

When designing a microfluidic master mold to be fabricated with 3D printing, it was beneficial to include features that could be used to control the overall PDMS device thickness and curvature. Microfluidic molds fabricated with stereolithography would not lay flat and had curvature after removing the mold from the printer as shown in Figure 2-5.

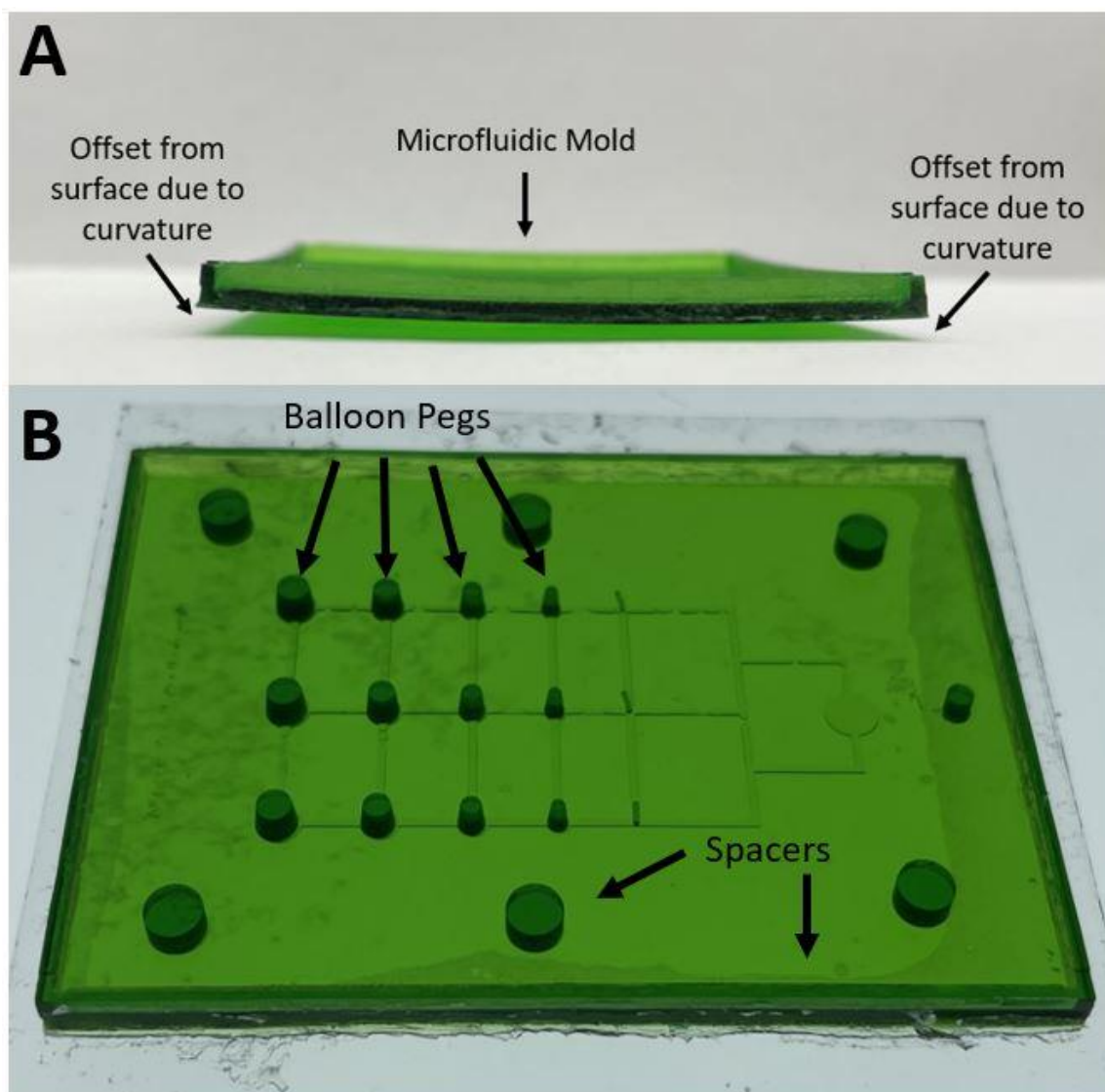


**Figure 2-5:** Image of 3D printed molds for microfluidic fabrication. (A) Side-view image of a microfluidic mold with curvature. At the mold's edges, it does not sit flat on the base

surface. (B) Top-view image of the mold. The spacers were used to control device thickness and correct curvature when the mold was clamped.

The curvature of the mold is thought to be due to residual stresses in the mold due to shrinkage of the polymer during solidification [66]. Curvature of the mold was undesirable as PDMS microfluidics fabricated from the molds have a higher level of channel height uncertainty and trouble bonding to base substrates. As such, spacers and walls at the edges of the mold were added that could be used with clamping to flatten the mold and control the overall channel thickness (Figure 2-5B). The spacer and wall heights were used to determine the final thickness of the PDMS microfluidic device. The wall had a thickness of 1 mm and was able to support any level of clamping necessary when curing PDMS in the mold. The usage of the 3D printed molds is discussed in depth in Chapter 3.2.

To ensure the microfluidic molds designed would be rigid during PDMS soft lithography. The base layer thickness must be considered. Ideally, the base layer of a microfluidic mold is thick enough to withstand multiple PDMS curing and removal processes without breaking or significantly deforming while also being thin to prevent material waste. A base layer thickness of 1 mm was used for microfluidic device mold used in this study. A base layer thickness of 1 mm was found to be ideal for conserving material while also having adequate strength for use.

Additionally, the build volume of the 3D printer was 102 mm x 57.5 mm x 120 mm for its length, width, and height, respectively. As such the molds printed by the 3D printer must conform to the maximum part size of the printer.

#### **2.4.2 Processing of Green Mold Resin<sup>2</sup>**

After 3D printing microfluidic molds with the green mold resin, the following steps must be taken to ensure the mold can be used for soft lithography. If these steps are not taken, the mold may inhibit PDMS curing, remain uncured, and maintain surface defects [67]. A flowchart describing the fabrication procedure for microfluidic molds made with the green mold resin is shown above in Figure 2-4.

Before post-print processing of the mold, it may be beneficial to allow the mold to stay on the build plate in the printer overnight. Keeping the mold in the printer after printing allows the excess green mold resin to drip off of the mold and build plate. Although it is not necessary, it may make further processing easier and more effective.

Once the mold is removed from the build plate of the printer, the mold was placed in a beaker and submerged in isopropyl alcohol (IPA) with a concentration equal to or greater than 90%. Next, the IPA within the beaker should be agitated to promote excess green mold resin removal from the mold. To agitate the IPA, the beaker was placed onto a digital shaker at 170 rotations per minute (rpm). The mold was shaken in IPA for a total of 50 minutes. To enhance resin removal, the mold was removed from the IPA every 10

---

<sup>2</sup> Published in the American Society of Mechanical Engineers International Mechanical Engineering Congress and Exposition 2023 conference. C. Emeigh, R. Pineda, B. Harms, and S. Ryu (2023) The effects of balloon thickness on the viability of a microfluidic cell compression device, ASME IMECE2023-113642.

minutes, sprayed with compressed air, and then placed back into the IPA to continue shaking. After the first 10-minute cycle, the IPA was replaced with fresh IPA.

After the mold had been washed in IPA for 50 minutes, the mold was exposed to UV light to finish the solidification of the green mold resin. The mold was placed into a UV oven (Professional CureZone, CADWorks) and exposed for 4 cycles, totaling 40 minutes. After each cycle, the mold's orientation was changed to promote even expose of the mold to UV light.

Once the mold had been fully solidified by UV light, the mold was washed with hot soapy water. Washing the mold with hot soapy water allowed the PDMS to solidify on the mold. Without washing the mold in soapy water, PDMS curing inhibition occurred at the interface between PDMS and the mold. It is thought that the PDMS cure inhibition is due to a buildup of ammonia compounds on the mold surface. Although no information was available for the green mold resin specifically, most photosensitive polymer resins use ammonia compounds as photo absorbers. It is thought that dish soap removes the thin oily ammonia film from the mold, preparing it for PDMS curing.

First, hot soapy water was prepared in a beaker by combining Dawn dish soap and hot water. Next, the mold was placed into the beaker and submerged in the hot soapy water. The beaker was then placed onto the digital shaker and spun at 170 rpm for 50 minutes total. Every 10 minutes, the mold should be removed from the water and sprayed with compressed air. After the first 10 minutes of washing, the hot soapy water was replaced with fresh hot soapy water. After 50 minutes, the mold should be sprayed once more and rinsed with hot water.

After washing the mold with IPA for 50 minutes, exposing the mold to UV light for 40 minutes, and washing the mold with hot soapy water for 50 minutes, the mold is ready to use for PDMS soft lithography. Failure to follow the steps properly will result in a mold unable to cure PDMS with surface defects.

## **2.5 Design and Fabrication Considerations for Clear Channel Resin<sup>3</sup>**

When developing clear channel devices for microfluidic fabrication, the following design and fabrication flow should be followed as shown above in Figure 2-4. Proper design and post-processing treatment of the materials will lead to high quality microfluidic device molds compatible with soft lithography. In this section, the processing procedure for the clear channel resin will be discussed.

### **2.5.1 Design Considerations for Increasing Printability of Clear Channel Resin**

To improve the quality of the 3D printed microfluidic device using the clear channel resin, the following design considerations must be taken. Failure to design a device compatible with the capability of the 3D printer may result in unusable microfluidic devices with blocked channels or poor channel features. The cross-sectional shape, height, and length of a microchannel contributed to whether the 3D printer had the capability to print the device. Channel geometry determines if the 3D printer must print overhanging structures, the orientation of the motherboard on the printer's build plate,

---

<sup>3</sup> Published in the American Society for Engineering Educations (ASEE) Midwest Section Conference 2023. C. Emeigh, A. Griswold, R. Hassan Pallock, J. Sahni, M. Schake, U. Anuta, J. Deters, and S. Ryu, 2023, Group-project-based development of a modular microfluidic platform: a case report on a hands-on microfluidics course, ASEE 2023.

and drainage of the channel while printing. Channel height and length determined the drainage of the channel while printing and the effectiveness of the post-processing procedure. To determine the optimal channel cross-sectional shape, height, and length the following experiment was employed.

To find the optimal parameters for the motherboard, several test devices were designed using SolidWorks (Dassault), printed, and tested. Circular, triangular, rectangular, and diamond channels were tested. These cross-sectional shapes were chosen for the following reasons. Circular channels were tested due to their axisymmetric features and the similarity to biological structures such as blood vessels. Triangular channels were tested because microfluidic molds fabricated with most silicone etching techniques produce triangular channels [68]. Rectangular channels were tested because they are the most common channel geometry for microfluidic devices. Diamond channels were tested as a secondary orientation of rectangular channels.

Regarding channel heights, channel heights of 120, 240, 480, 760, 1,020 and 1,280  $\mu\text{m}$  were tested for the following reasons. The smaller channel heights were tested because having the smallest dead volume possible for the motherboard is beneficial to biological studies. The larger channel heights were tested because the 3D printer is more compatible with larger channels. All the channel sizes used followed the 30  $\mu\text{m}$  resolution of the 3D printer.

To efficiently test channel geometry and height simultaneously, eight different test devices were designed. Each test device had a single shape with three channel heights. As such, all four shapes were tested with all six heights by printing two devices for each shape. Additionally, all the test devices had channels with a length of 10 mm. It

was found that the best channel shape and height for the motherboard was circular channels with a height of 1,020  $\mu\text{m}$ . Circular channels were identified as the best due the ability of the printer to print the full length of the channel. This indicated that the channels drained well during printing, and the orientation during printing was acceptable. After printing and processing, other shapes had cured material filling the channel, or the channel had collapsed during printing resulting in channel blockage.

Afterwards the maximum printable length of the channel was found by creating a test device with the following channel lengths: 5, 10, 15, 20, 25, 30, 35, 40, 45, 50, and 55 mm, with the chosen channel shape and height, as shown in Figure 2-6.

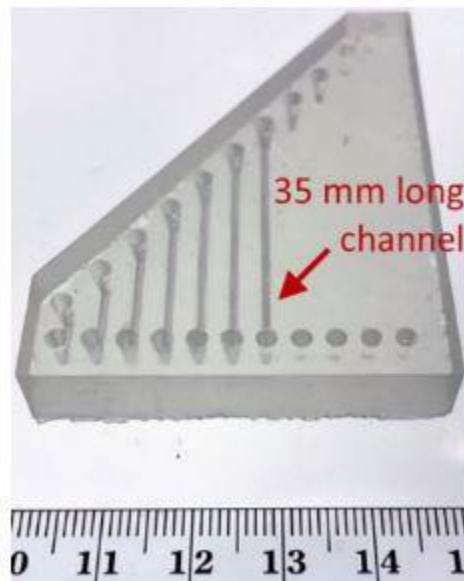


**Figure 2-6:** Test device with various channel lengths. The 35 mm channel length was the longest channel that printed. Published in [35].

It was found, in the printed test device, that channels longer than 35 mm had defects, and it was speculated that resin could have not drained well from such long channels. As such, drainage holes were added to the final design of the devices with channels longer than 35 mm to allow for excess resin to flow out of the channels while printing.

Additionally, the build area of the 3D printer was 102 mm x 57.5 mm x 120 mm. As such the channel devices printed by the 3D printer must conform to the maximum part size of the printer.

In summary, it was found that the best design parameters for devices printed with the clear channel resin was a circular channel with a height of 1,020  $\mu\text{m}$  and a maximum length of 35 mm. The results are summarized below in Table 2-5. Additionally, it is beneficial to keep all channel heights a multiple of 30  $\mu\text{m}$  and all channel widths a multiple of 53  $\mu\text{m}$  to prevent unexpected effects from the printer's vertical resolution of 30  $\mu\text{m}$  and lateral resolution of 53  $\mu\text{m}$ .

**Table 2-5:** Optimal design parameters for devices printed with the clear channel resin [35].

Channel Parameter	Ideal Parameter Choice
Shape	Circular
Height	1,020 $\mu\text{m}$
Length	< 35 mm

### 2.5.2 Processing of Clear Channel Resin<sup>4</sup>

After 3D printing microfluidics using the clear channel resin, the following steps should be taken to prepare the microfluidic platform for use. Failure to complete the following steps or completing them in the improper order may result in a non-functional device [35]. Excess resin, channel blockages, and improper curing may result in suboptimal devices and material properties. A flowchart describing the fabrication procedure for microfluidic devices made with the clear channel resin is shown above in Figure 2-4.

After printing a microfluidic device with the clear channel resin, it may be beneficial to allow the printed device to sit in the printer for 10 to 20 minutes. Although it is not necessary, allowing the device to sit will allow excess resin to drip off the device and back into the material vat. Lower amounts of resin left on the part when it is removed from the printer will reduce the amount of cleaning that must be done in later steps. Additionally, the parts printed with the clear channel resin do not need to stay in the printer as long as parts printed with the green mold resin. Due to the lower viscosity of the clear channel resin, excess resin dripped off the part much quicker.

Next, the printed part was removed from the 3D printer, and a syringe was used to spray IPA into the channels of the device through its inlet and outlet ports and in areas with a high likelihood of entrapping excess resin. Spraying the device with IPA helped

---

<sup>4</sup> Published in the American Society for Engineering Education Midwest Section Conference 2023. C. Emeigh, A. Griswold, R. Hassan Pallock, J. Sahni, M. Schake, U. Anuta, J. Deters, and S. Ryu (2023) ASEE Midwest Section Conference 2023.

remove excess resin trapped within the printed microfluidic device channels and other areas with complex geometry. After spraying specific areas of the device with IPA, the device was fully submerged into IPA for 10 seconds. The IPA was gently agitated by hand to promote the removal of excess resin from the microfluidic device. After 10 seconds, the device was removed from the IPA. Exposing the clear channel resin to IPA for longer than 10 seconds may lead to frosting of the material, reducing the optical transparency of the device.

If there was still excess resin left on the printed device after washing the device in IPA, hot water was used to remove the remaining material. If required, the device should be submerged into hot water for 10 seconds and gently agitated by hand. Hot water can also lead to frosting of the material, so it is best to limit the amount of time the device is submerged. Washing the mold in hot water may be repeated until all excess material has been removed.

Once the excess resin had been removed from the microfluidic device, the device must be exposed to UV light. The device was placed into a UV cure oven and exposed to UV light for 30 seconds total in 10 second intervals. Overexposing the clear channel resin to UV light will cause yellowing of the material. As such, the device was exposed to 10 seconds of UV light and then allowed to rest for 1 minute. After 30 seconds of cumulative exposure time, the device was inspected to see if it was fully cured. If the material was fully cured, it would be hard and no longer sticky. If the device is still soft or sticky, it was exposed to UV light further for 10 second intervals until it was fully cured.

After removing the device from the 3D printer, washing the device with IPA, washing the device with hot water, and exposing the device to UV light, the microfluidic device is ready for operation. Careful design of the microfluidic device can improve printability and reduce problems with its usage.

## Chapter 3: Motherboard and Module Fabrication

### 3.1 Motherboard Design and Fabrication

#### 3.1.1 Microfluidic Motherboard Design

When designing the microfluidic motherboard, as shown in Figure 3-1A, the following parameters were considered: channel shape, channel height, channel length, connection peg size and height, 3D printed O-ring size, the inclusion of drainage holes, the distance between the connection pegs, and the external tubing connections. Proper design of the microfluidic motherboard allowed for it to be easily printed, compatible with microfluidic modules, and easily connected to external flow sources. Easy, reversible, and tightly sealed fittings were required to make the microfluidic motherboard an effective tool for microfluidic applications.

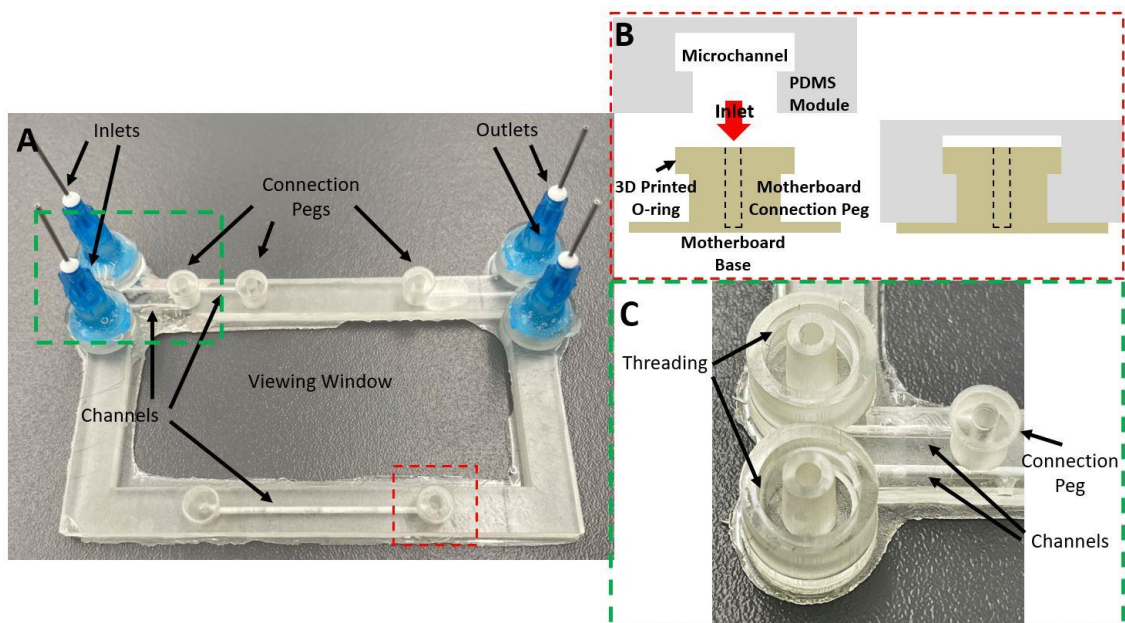


**Figure 3-1:** (A) Image of the 3D printed motherboard with the inlets, outlets, connection pegs, channels, and its viewing window labeled. (B) Schematic of connection between the motherboard and the channel layer. The schematic shows the motherboard and channel disconnected with basic anatomy. The motherboard connection peg has a 3D printed O-ring feature to help sealing. The depth of the microchannel inlet for the modules was greater than the height of the connection peg to prevent channel blockage. (C) An image of the luer-lock connection mechanism without needles for the inlets and outlets of the motherboard.

When designing the channels of the motherboard (Figure 3-2), the channel shape, height, and length were chosen to be circular, 1020  $\mu\text{m}$ , and a maximum of 35 mm, respectively. Circular channels were found to have the best printability as shown in Chapter 2.5.1. A channel height of 1020  $\mu\text{m}$  as shown to prevent channel blockage during printing. Keeping the channel length below 35 mm allowed the channel to drain while printing, preventing blockages. For channels longer than 35 mm, drainage holes were added. These optimal channel parameters are discussed in depth within Chapter 2.5.1.

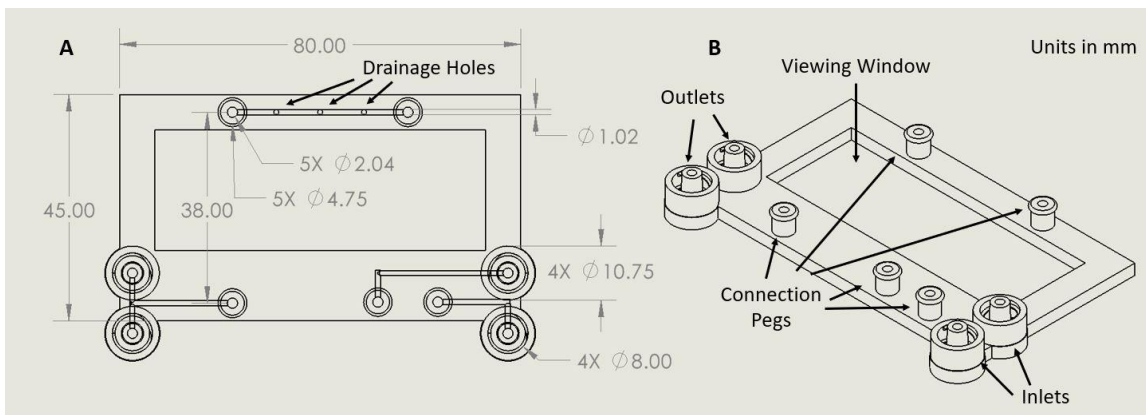


**Figure 3-2:** Computer aided design (CAD) drawing of the motherboard and its dimensions. All units are in mm. (A) Top-view of the motherboard. The drainage holes are labeled. Channels are only shown in (A) for clarity. (B) Isometric view of the motherboard. The inlets, outlets, connection pegs, and a viewing window are labeled.

The connection pegs on the motherboard for each module (Figure 3-2A) were positioned 38 mm apart from one another across the viewing window. The distance between the connection pegs was important because of the build plate size of the 3D printer. Because of the build area of the 3D printer, channels fabricated for use with the motherboard could have a maximum length of 50 mm. As such, the distance between the connection pegs was arbitrarily chosen to be 38 mm apart to conform to the build volume of the 3D printer.

For the luer-lock connections on the motherboard that were used to connect the syringe pumps to the motherboard, the following considerations were taken. To enable the motherboard to work with preexisting syringe needles, the outer ring of the luer-lock mechanism had a diameter of 8 mm with M8 x 1.0 threads, and a pitch of 3.20 mm was used. Additionally, the portion that sits inside the syringe needle had a diameter of 4 mm and a slight taper angle of  $1.80^\circ$  to enable easy insertion.

### **3.1.2 Motherboard Fabrication**

Once the motherboard had been printed as described in Chapter 2.5.2, syringe needles (23G 0.5" blunt needle B23-50, SAI Infusion Technologies) with a luer-lock

connection mechanism were screwed into the inlets and outlets of the motherboard. When syringe needles were screwed into the inlets and outlets of the motherboard, slight leaking still occurred. The leaking may be due to the tolerance of the 3D printed part or due to misalignment between the needle and the motherboard. To prevent leaking, the thread pitch of the 3D printed motherboard luer-lock mechanisms may be increased to give the syringe needle more room for proper alignment. Additionally, the diameter of the inner portion of the luer-lock mechanism can be increased for a tighter seal with the syringe needle.

To prevent leaking, the needles were screwed on, and epoxy (Gorilla Epoxy Clear) was used to permanently attach the needles to the motherboard. Although some of the motherboard's modularity was eliminated by epoxying the needles, it allowed for leak free sealing while using minimal resources. After connecting the needles, the motherboard was ready for use (Figure 3-1).

## **3.2 Microfluidic Module Design and Fabrication**

### **3.2.1 Microfluidic Module Design**

The microfluidic mixing module designed and used in combination with the motherboard in this study consisted of multiple parts as shown in Figure 3-3. The first layer of the device was a glass plate, which acted as the base of the device, followed by the PDMS body of the balloon part, a thin PDMS balloon layer, and finally the PDMS mixing channel part. When designing the microfluidic mixing module, the printability of the mold, removal of PDMS from the mold, operation of the device, and compatibility of the device with microscopy imaging were considered.

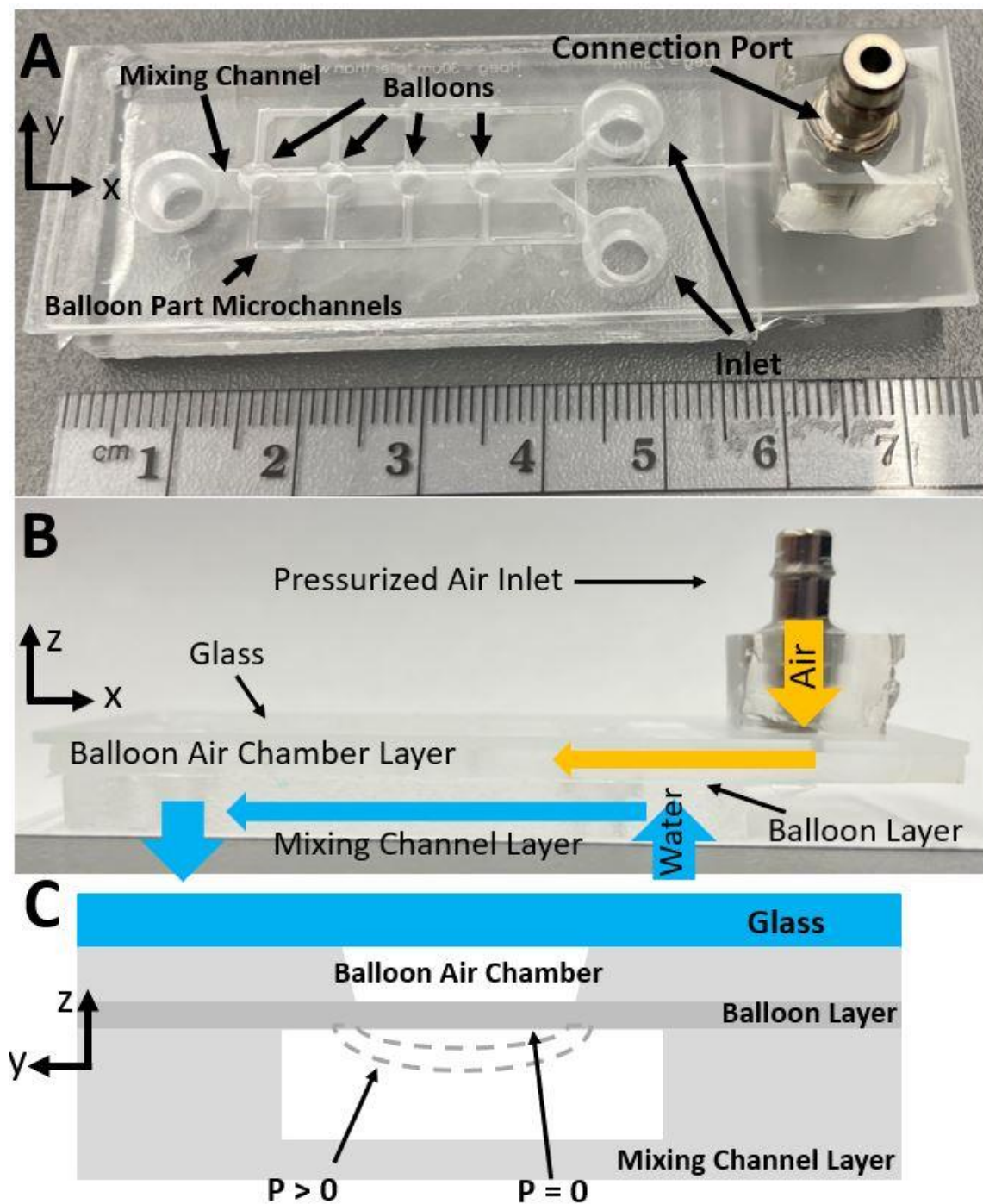


**Figure 3-3:** (A) Top view of the PDMS microfluidic mixing device. The balloon part of the device consists of a connection port for pressurized air, microchannels, and an array of four 2.5 mm diameter balloons. The mixing channel part consists of a y-channel with two inlets and one outlet. (B) Side-view of the parts of the device. The yellow arrows

indicate the direction of flow for pressurized air through the balloon part, and the blue arrows indicate the direction of flow of dyed water through the mixing channel part. (C) Side-view schematic of device layers and operation. Balloons become inflated when the balloon air chamber was pressurized.

The first consideration taken when designing the microfluidic mixing module was the printability of the mold. Features such as overhangs, the channel dimensions, and feature thickness all play a role in whether a mold can be 3D printed. Overhanging features typically will not print due to the feature lacking support. Also, channel dimensions must be a multiple of the 30  $\mu\text{m}$  resolution of the 3D printer (e.g. 30  $\mu\text{m}$ , 60  $\mu\text{m}$ , 90  $\mu\text{m}$ , 120  $\mu\text{m}$ , etc.). Additionally, larger channel features typically have better definition. Thicker features have improved printability compared to thinner features. Detailed design parameters to ensure printability of the mold are discussed in depth in Chapter 2.4.

In the balloon part designed, the square channels had a height and width of 750  $\mu\text{m}$  (Figure 3-4A). Multiple channel paths to the same balloon were included as a redundancy to reduce the effect of unexpected channel blockage. A 4 mm diameter inlet section was added to facilitate ease of alignment for the connection port. A taper angle of  $5^\circ$  was added to the balloon pegs of the mold to enable easy removal of PDMS from the mold and to prevent the PDMS from tearing. The balloon pegs had a height that was 30  $\mu\text{m}$  taller than the outer wall of the mold. The balloon peg height ensured there was minimal to no PDMS over the balloon air chamber when removing the PDMS from the mold. The balloons also had 6.25 mm between them, center to center, to fit the maximum

number of balloons on a single chip without risking balloon tearing or balloons interfering with one another.

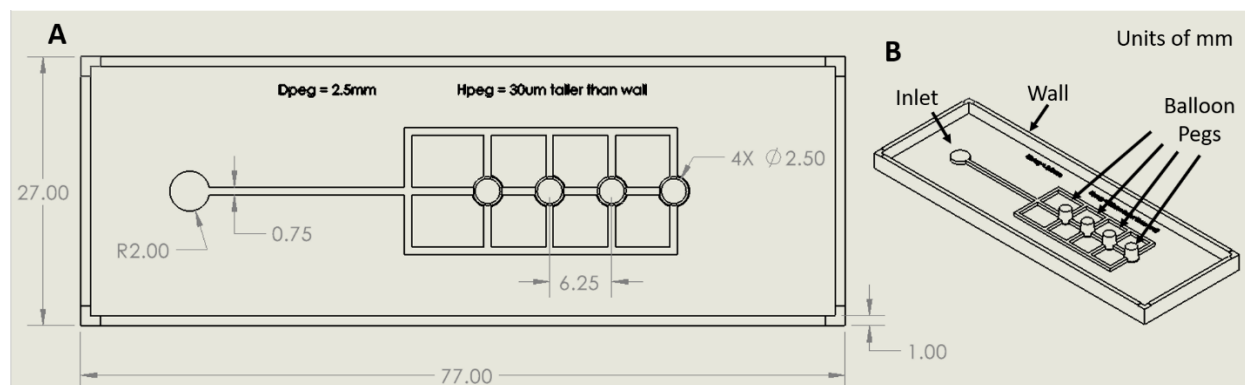


**Figure 3-4:** Computer aided design (CAD) drawing of the balloon part mold and its dimensions. All units are in mm. (A) Top-view of the balloon part mold. (B) Isometric view of the balloon part mold. The inlets, balloon pegs, and outer wall are labeled. Note, the balloon pegs are 30  $\mu\text{m}$  taller than the wall of the mold.

The balloons of the balloon part had a nominal diameter of 2.5 mm. Previous studies used balloon diameters ranging from 1.2 to 2.0 mm and showed that as balloon diameter increased, balloon height also increased [62, 48]. Balloon diameters of 2.5 mm were chosen because it was assumed that 2.5 mm balloons would have a high level of inflation in response to an applied pressure. The larger diameter of the balloons also eliminated some of the effect of the 3D printer's tolerance. For instance, the 3D printer has a set tolerance value, due to the over-solidification of resin, determined by its hardware and software. As parts become larger, although the tolerance of the printer is

constant, the effect of the excess solidification becomes less noticeable due to the relative size difference between the printed part and the over solidified material. Additionally, the larger size of the balloons made it easier to align the mixing channel over the balloon part.

In the mixing channel part designed (Figure 3-5A), the rectangular channel had a nominal height and width of 840  $\mu\text{m}$  and 3.5 mm, respectively. A nominal channel height of 840  $\mu\text{m}$  was chosen as it was easily printed by the 3D printer as discussed in Chapter 2.4, was small enough to allow balloons to reach the top of the channel and was large enough to plasma bond to the balloon layer without the balloons bonding to the top of the channel. Additionally, the channel height of 840  $\mu\text{m}$  made image analysis more sensitive to color changes for the mixing experiment discussed in Chapter 6. A nominal channel width of 3.5 mm was chosen to enable easy alignment of the mixing channel and the balloons of the balloon layer and prevent inflated balloon obstruction.

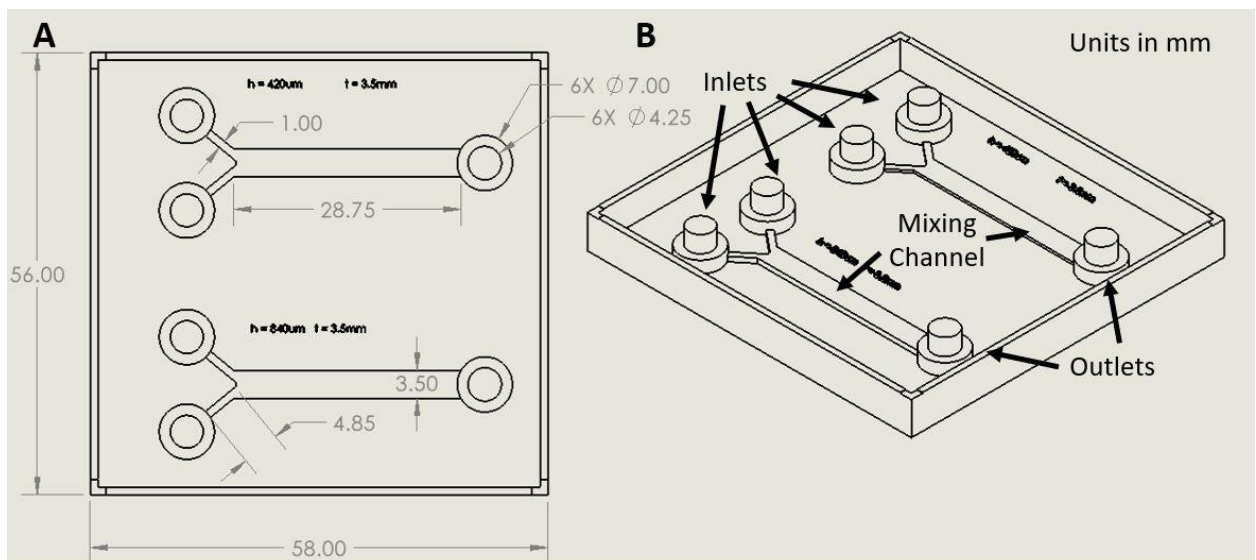


**Figure 3-5:** Computer aided design (CAD) drawing of the mixing channel part mold and its dimensions. The mold had two mixing channels with heights of 420  $\mu\text{m}$  and 840  $\mu\text{m}$ . The 840  $\mu\text{m}$  mixing channel (the bottom one) was used in this study. All units are in mm. (A) Top-view of the mixing channel part mold. (B) Isometric view of the mixing channel part mold. The inlets, outlets, and mixing channels are labeled.

The inlets and outlets of the mixing channel part were designed to be compatible with the motherboard's connection pegs as shown in Figure 3-5B. The connection between the motherboard and the microfluidic module needed to be easily connected, reversible, and leak-free. The inlets were designed to have two areas with different diameters as shown in Figure 3-5B. The larger diameter deeper in the layer was the microchannel. The microchannel was the region where flow would occur, and the 3D printed O-ring of the connection peg would sit. The smaller diameter was the inlet and was designed to squeeze the motherboard connection peg.

Two versions of the microchannel were printed on a single mold. Both microchannels had a width of 3.5 mm. One microchannel had a height of 420, and the other microchannel had a height of 840  $\mu\text{m}$ . In this study, the microchannel with a height of 840  $\mu\text{m}$  was used to allow more room for the balloons to inflate. The inlet had a diameter of 4.25 mm and a height of 5.07 mm. These heights were chosen as the motherboard had a connection peg diameter of 4.75 mm, an O-ring cross-sectional diameter of 1.02 mm, and a height of 4.98 mm. The motherboard connection pegs were larger than the inlet of the microfluidic module so the PDMS of the module would squeeze the peg, creating a seal as shown in Figure 3-1B. The microchannel was designed

to be deeper than the motherboard connection peg so that channel blockage could not occur.

### **3.2.2 Soft Lithography for the Mixing Module<sup>5</sup>**

To fabricate microfluidic devices from the 3D printed molds, soft lithography was used. Soft lithography is a microfluidic fabrication technique where channel features are created by casting rubber into a mold to replicate an inverse of the channel features of the mold into the rubber device. In this study, PDMS was the rubber used to fabricate the devices, and two separate molds were used to fabricate the PDMS body of the balloon part and the mixing channel part. Fabricating microfluidic devices using the 3D printed mold and soft lithography has been written about previously [69]. The soft lithography fabrication procedure commonly used in microfluidic fabrication is as follows and is shown below in Figure 3-6 [1, 70].

---

<sup>5</sup> The soft lithography technique was accepted for presentation in the American Society of Mechanical Engineers conference of Fluids Engineering Division Summer Meeting 2024. C. Emeigh and S. Ryu, Using brightfield microscopy to assess the balloon expansion performance of a microfluidic cell compression device, ASME FEDSM 2024-130787.

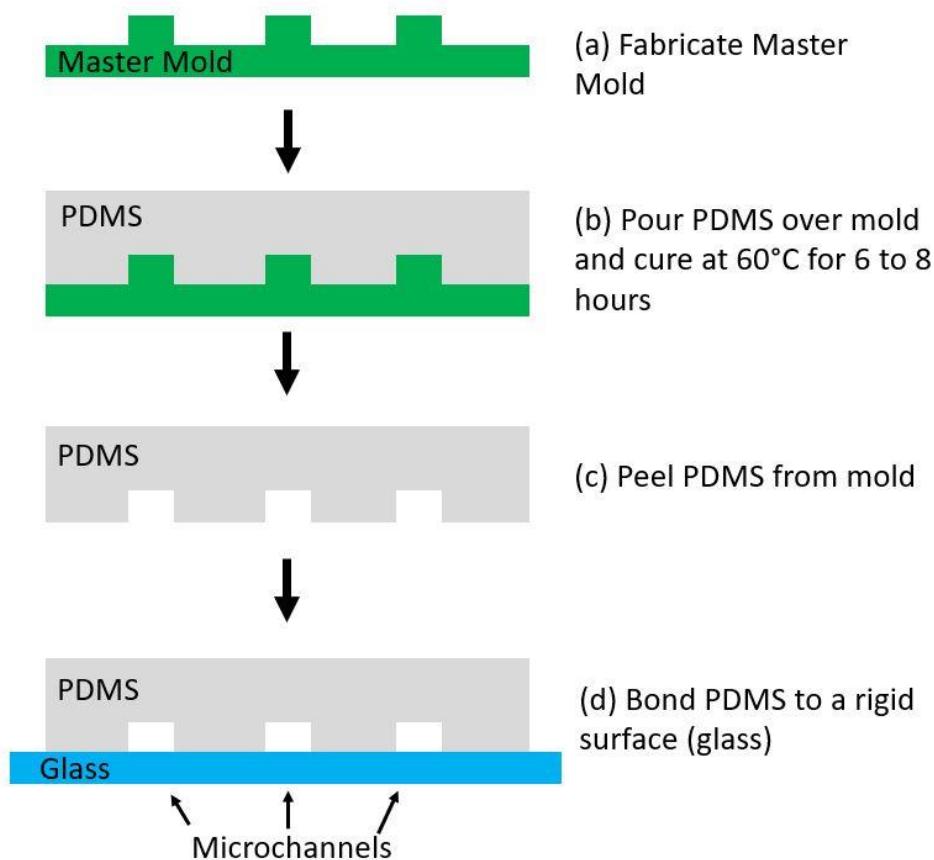


**Figure 3-6:** Schematic diagram of the soft lithography procedure to fabricate microfluidics. (a) In this study, the mold was designed in a CAD program and printed with a 3D printer. (b) PDMS is poured into the mold and cured at 60°C for 6 to 8 hours. (c) The cured PDMS body is carefully removed from the mold. (d) The PDMS body is bonded to a glass plate to seal the microchannels. Adapted from [70].

After the mold for the body of the balloon part had been fabricated and prepared for use with soft lithography, 15 g of 10:1 base-crosslinking agent PDMS (Sylgard 184, Dow Corning) was mixed for 5 minutes. The mold was placed into a vacuum chamber,

the PDMS was poured into the mold, and a vacuum was applied for 1.5 hours to remove air bubbles within the PDMS.

Next, the mold was sandwiched between a transparency film, glass plates, foam pads, and plexiglass as described in [47, 48]. The clamping setup is shown below in Figure 3-7. A clamp was used to hold the setup together and apply pressure to the mold. The clamp was tightened until slight resistance was felt. If the clamp was too loose, it would not flatten the mold or control the microfluidic device height. If the clamp was too tight, the glass plate or mold could break and render the resulting device unusable. Then, the setup was placed into an oven at 60°C overnight. Clamping the device using the sandwiching method helped keep the mold flat and controlled the thickness of the PDMS part of the microfluidic device.

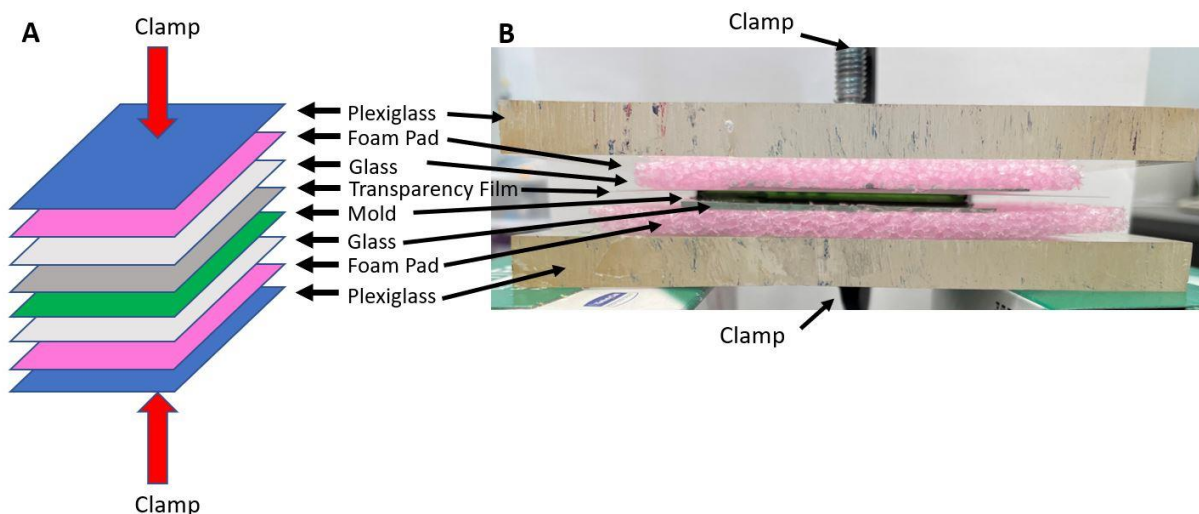


**Figure 3-7:** (A) A schematic of the clamping setup when performing PDMS soft lithography with 3D printed molds. From bottom to top the components are plexiglass, a foam pad, a glass plate, the mold, transparency film, a glass plate, a foam pad, and plexiglass. (B) An image of the clamping setup for a 3D printed microfluidic mold.

After curing the PDMS, it was removed from the mold. This became the body of the balloon part. The PDMS body of the balloon part was then plasma bonded to a glass slide (25 mm x 75 mm). For later connection of the connection port to the microchannels of the balloon part, a 1.5 mm diamond ball burr was used to drill a hole into the glass where the connection port would be bonded. Due to the mold's balloon pegs being 30  $\mu\text{m}$  taller than the nominal height of the spacers and outer wall of the mold, there was little to no PDMS over the balloon chamber after PDMS removal. As such, the microchannels of the device were open and needed to be sealed to make the balloons.

To seal the microchannels, a 58  $\mu\text{m}$ -thick PDMS layer was created separately with spin-coating. A transparency film was first cut to be approximately 50 mm by 75 mm, cleaned with 90% IPA, dried, and placed into the spin-coater (Laurell Technologies Corporation, WS-650MZ-23NPPB). Once secured to the spin-coater, 3 grams of 10:1 degassed PDMS was poured onto the center of the transparency film. Care was taken to prevent the introduction of air bubbles into the PDMS when pouring. The transparency film and PDMS were then spun at 1,000 rpm for 1 minute. Spinning the PDMS on the transparency film evenly spread the PDMS over the top surface of the transparency film. The PDMS was allowed to rest for 10 minutes before curing. This improved the consistency of the PDMS thickness.

The speed at which degassed PDMS was spun determined the overall thickness of the resulting PDMS membrane. It was observed that the thickness of the PDMS after spin coating also depended on the amount of PDMS poured onto the transparency film and the size of the transparency film. As such, all of the measurements were conducted using the methodology stated previously. As the rotational speed of the spin coater increased, the

resulting thickness of the PDMS membrane decreased as shown in Figure 3-8 [48]. In this study, a spin coater speed of 1,000 rpm was used to produce balloon layer thicknesses of 58  $\mu\text{m}$ .

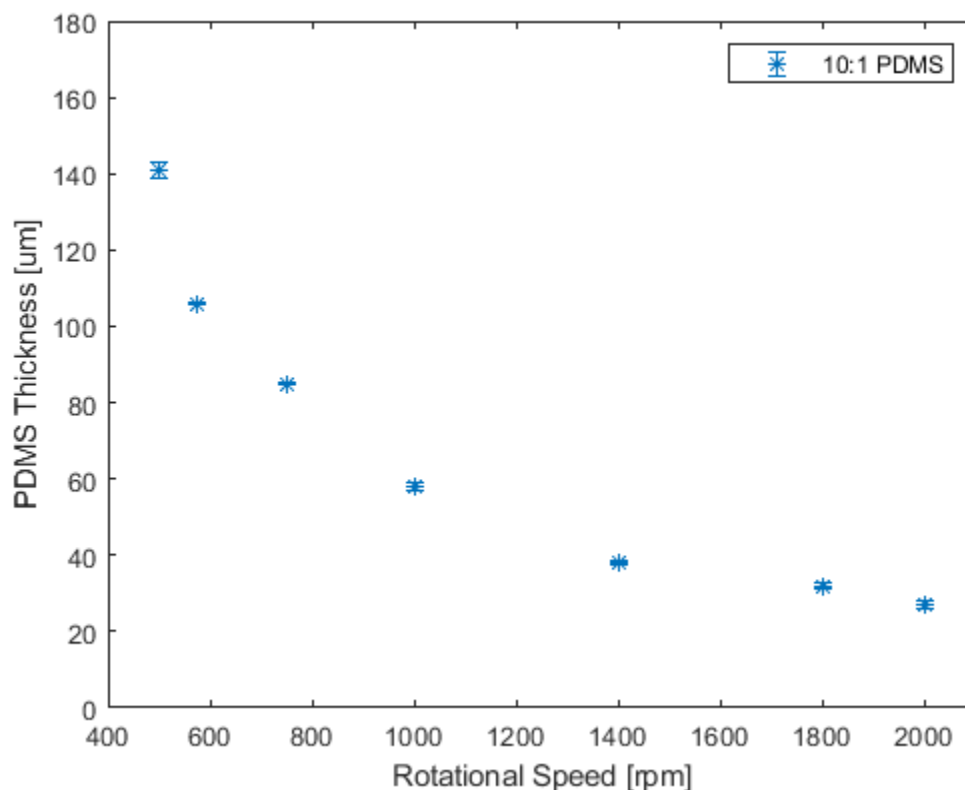


**Figure 3-8:** Effect of spin-coater rotational speed (rpm) on the thickness of the resulting PDMS membrane. PDMS was spun onto transparency films with dimensions of 25 mm by 75 mm. Error bars represent standard deviation ( $n = 3$ ).

After the PDMS body from the mold and the spin-coated PDMS had been prepared, the spin-coated PDMS was placed into an oven at 80°C for 25 minutes to become partially cured. Next, the PDMS body and the spin-coated PDMS were placed

into a plasma cleaner and plasma treatment was applied for 1 minute. After plasma treatment, the two parts were brought into contact and placed in an oven at 80°C overnight to finish PDMS solidification and bond the two parts together permanently. Using partially cured PDMS to seal the body of the microfluidic helped to create a tighter seal and prevent leakage from the balloons.

Separately, the connection port for the balloon part was prepared. The connector for the connection port (EB40-250, Pneumadyne Inc.) was placed vertically in a petri dish. PDMS was then slowly poured into the petri dish until approximately 60% of the connector was covered in PDMS. Care was taken when pouring PDMS to prevent knocking over the connector. Once the PDMS was poured, the PDMS was cured in an oven at 60°C overnight. Finally, a connection port was plasma bonded onto the device.

Separately, the mold for the mixing channel part and soft lithography was used to fabricate the mixing channel part of the device. Similar to the process used for the body of the balloon part, PDMS was poured into the mold and cured at 60°C overnight. The PDMS was then removed from the mold and plasma bonded into the previously fabricated balloon device. Because of the design of the motherboard and the mixing channel, no connection ports needed to be added to the device.

### **3.3 Motherboard and Module Assembly**

Once the microfluidic modules and the motherboard had been fabricated, the following procedure was implemented to assemble the components. Due to the design of the motherboard and modules, connecting the two was very easy. First, vacuum grease

(High Vacuum Grease, Dow Corning) was applied to the connection pegs of the motherboard. The vacuum grease helped prevent leakage between the motherboard and the connected modules. Next, the modules were aligned with the connection pegs, and a light uniform force was applied to the module until it snapped into connection. After usage, the microfluidic modules were removed by grabbing the module and pulling it while gently wiggling the connection area. The operation of the modular platform and its implementation for a mixing experiment is discussed in depth in Chapter 6.

## **Chapter 4: Balloon Inflation Characterization**

### **4.1 Motivation for Characterizing Balloon Height Response**

The microfluidic balloon device in this study consists of a flexible PDMS membrane that can inflate like a balloon under an applied pressure (Figure 4-1A). The height to which the balloons of the device inflate to under an applied pressure (hereinafter called the balloon height) characterizes how well the device functions. Previously, it was shown that by modulating the balloon height, it is possible to apply varying magnitudes of compression to cells [48]. Additionally, they showed that balloon height is highly dependent on balloon diameter. Due to the ability to modulate balloon height, applications of the device as a microfluidic mixer were investigated. Other studies involving microfluidic mixers with deformable membranes show that the level of membrane deflection controls the level of mixing [71, 72].

As such, to understand the mixing capability of the microfluidic balloon devices fabricated in this study, reliable methods for measuring balloon diameter and balloon height must be developed and implemented. Characterization of the balloon inflation will allow for prediction of mixing performance and allow for others to understand and utilize the device in future works.

The PDMS microfluidic balloon device (Figure 4-1C) was fabricated with a 3D printed mold (Figure 4-1B). As shown in Figure 4-1A, the device consists of three layers: a glass plate as the base of the device, a PDMS body consisting of microchannels and balloon chambers, and a thin PDMS layer forming balloons.

The device was designed to have three identical rows of balloons for greater efficiency when characterizing the device. To fabricate the device, PDMS was poured

into the mold to replicate the inverse of the mold. Therefore, the balloon pegs (Figure 4-1B) of the mold created the balloon cavity and controlled the balloon diameter of the resultant PDMS device. The diameters of the balloon pegs ranged from 0.5 mm to 2.5 mm in each row. After fabricating PDMS devices from the mold, it was found that the 0.5 mm diameter pegs would break. As such, only balloons with diameters greater than 0.5 mm were considered in this study. Therefore, each device contained twelve balloons per device (3 balloons for all 4 diameters). Finally, multiple microchannel paths to each balloon were added to reduce the likelihood of a blocked channel rendering the device inoperable.

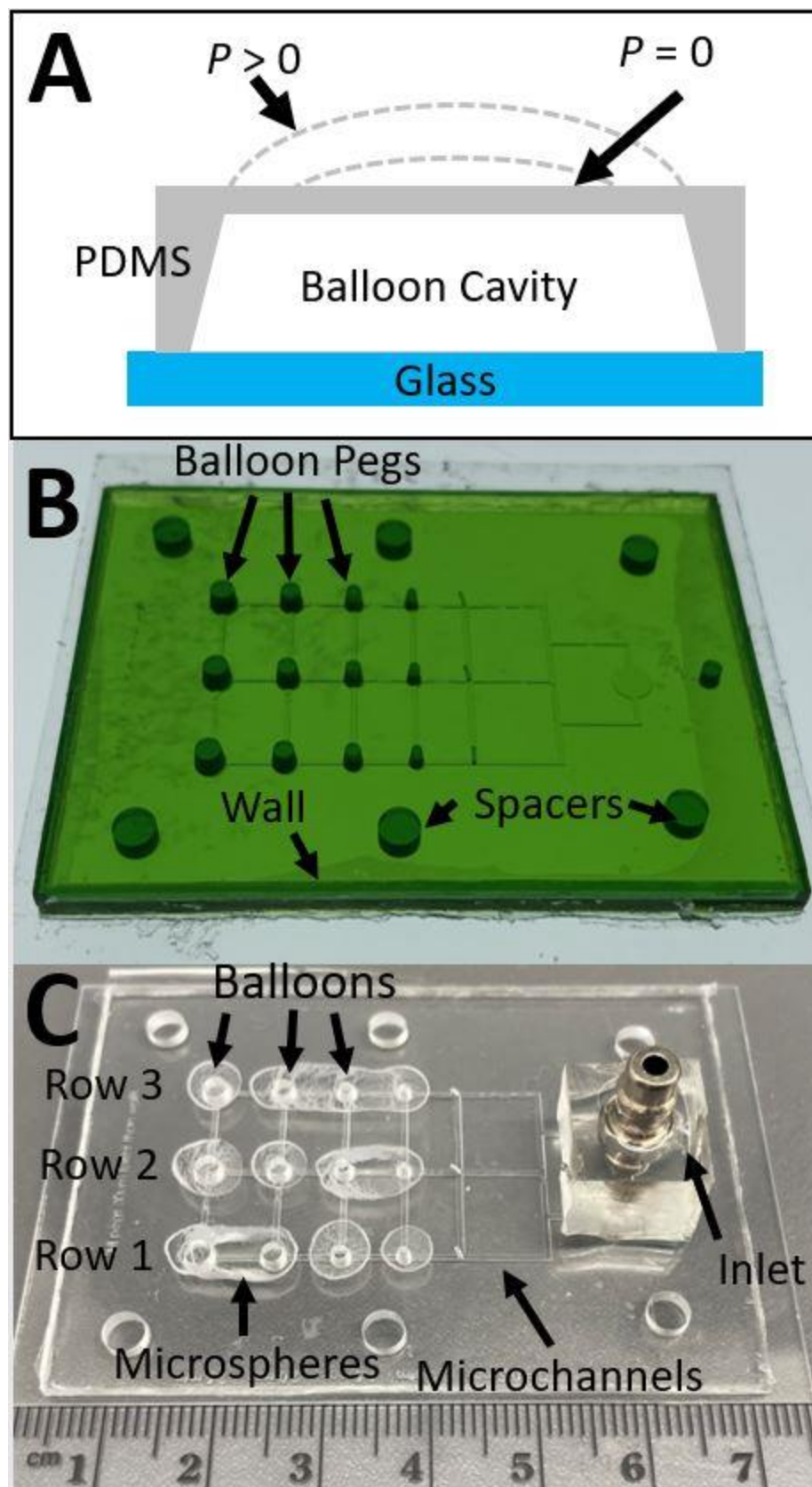


**Figure 4-1:** (A) Schematic of balloon inflation due to an applied pressure. (B) 3D printed mold used with soft lithography for device fabrication. (C) PDMS microfluidic cell compression device. The device consists of an inlet port, microchannel network, and an array of inflatable balloons with diameters ranging from 1.0 mm to 2.5 mm.

#### 4.2 Previous Balloon Characterization Methods

As shown in our previous study [48], the height of an inflated balloon depends on the diameter of the balloon. The balloon diameter was not always the same as the nominal balloon peg diameter due to over solidification of the resin by the 3D printer and expansion or shrinkage of the polydimethylsiloxane (PDMS) during fabrication. As such, the actual diameter of the balloons in this study needed to be measured accurately.

In a previous study [73], the following theoretical model to relate balloon height to various balloon properties was developed.

$$H = \left( \frac{3P \left(\frac{D}{2}\right)^4 (1-\nu)}{E(7-\nu)t} \right)^{\frac{1}{3}}, \quad (4-1)$$

where  $H$  is balloon height,  $P$  is applied pressure,  $D$  is balloon diameter,  $\nu$  is Poisson's Ratio of PDMS,  $E$  is Young's Modulus of PDMS, and  $t$  is balloon thickness. This equation suggests that any of the previously mentioned balloon parameters can be used to control balloon inflation. Our previous study only investigated the effects of  $D$  on  $H$ . As such, two devices with varying balloon thicknesses of 71  $\mu\text{m}$  and 132  $\mu\text{m}$  were developed to test the effect of balloon thickness ( $t$ ) on balloon inflation.

### 4.3 Confocal Laser Scanning Microscopy and Image Processing<sup>6</sup>

In the previous study, the effects of balloon diameter on balloon height was investigated by using confocal laser scanning microscopy to measure the balloon heights of a pressurized balloon device [48]. Although it was found that as balloon diameter increased balloon height increased according to the theoretical model, the method used of measuring balloon height suffered the following limitations. The diameter of the balloons was never measured and thus the actual diameter of the balloons on the device was not known. Additionally, to process the obtained scans, the microscope software (VK Analyzer, Keyence) was used which did not allow for a high level of control over data analysis.

As such, a new method of measuring balloon diameter using confocal and brightfield microscopy was developed. The method of analyzing balloon height data from confocal laser scanning microscopy was improved by implementing a MATLAB-based image processing code. To further characterize the balloons on the microfluidic device, the height of the balloons in response to different balloon diameters and different thicknesses was investigated [67].

#### 4.3.1 Diameter Characterization

The balloon pegs of the mold were imaged with a confocal laser scanning microscope (VK-X200K, Keyence) (Figure 4-2A) to measure their diameter. During

---

<sup>6</sup> Published in the American Society of Mechanical Engineers conference of International Mechanical Engineering Congress and Exposition 2023. C. Emeigh, R. Pineda, B. Harms, and S. Ryu (2023) The effects of balloon thickness on the viability of a microfluidic cell compression device, ASME IMECE 2023-113642.

imaging, the “fast” setting with a 5x objective lens ( $NA = 0.13$ ) and a  $z$ -step size of  $16\ \mu\text{m}$  was used for speed. Automatic image stitching within the software of the microscope (VK Viewer, Keyence) was used to image the entirety of each peg. From the imaging, a topographical map of the balloon peg of the mold was generated (Figure 4-2A). By looking at the diameter of the section of the image at the greatest  $z$ -value, the diameter of the balloon peg could be measured (Figure 4-2B).

The balloons of the PDMS microfluidic device fabricated with the imaged mold did not always have the same diameter as the diameter of the balloon peg due to the fabrication procedure of the device. Therefore, the balloons of the PDMS device were imaged under a digital microscope (Handheld USB Microscope, KMDES) (Figure 4-2C). ImageJ was used to measure the diameter of the balloons from the obtained images. The diameter was measured in four directions for each balloon and averaged to reduce error.

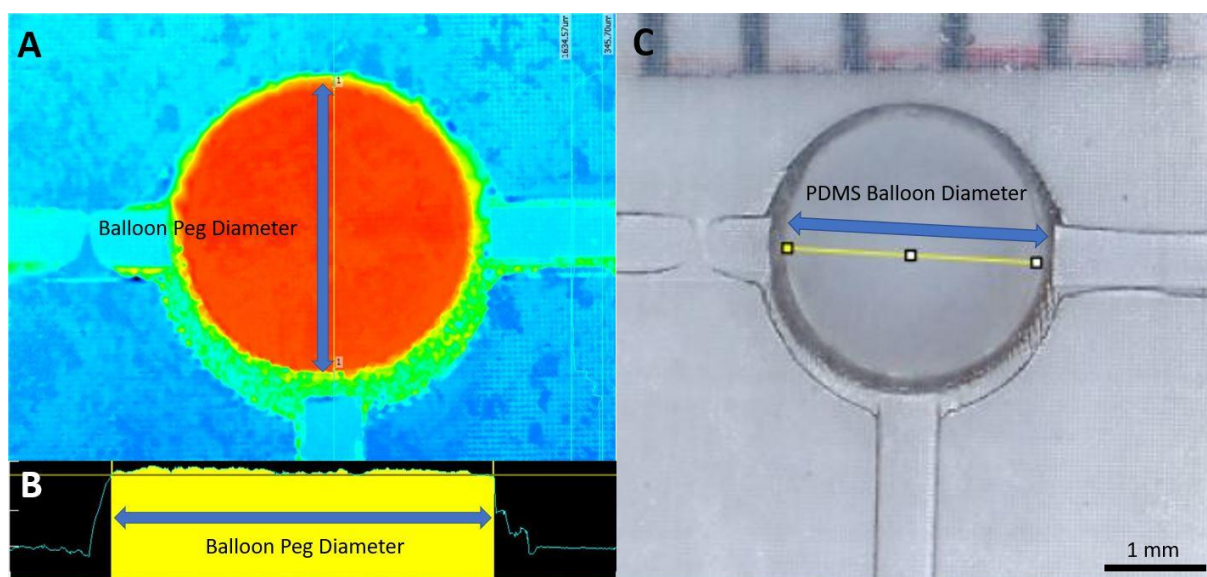


**Figure 4-2:** Measurements of the balloon diameter. (A) Surface topography image of one of the balloon pegs of the mold (top view). (B) Cross-sectional profile of the balloon peg. (C) Image of the PDMS balloon fabricated from the balloon peg in (A).

Once the methodology for measuring the diameter of the balloon pegs of the mold and the balloons of the PDMS microfluidic had been established, the process was repeated to measure all the balloon pegs and PDMS balloons of a single device. Balloon pegs and PDMS balloons with nominal diameters of 1.0, 1.5, 2.0, and 2.5 mm were measured, and each nominal diameter had three balloon pegs and three balloons.

#### **4.3.2 Balloon Height Measurement with Confocal Microscopy and Image Processing**

To measure the inflated balloon heights of the microfluidic device, the following procedure was implemented. An air pump (SP 500 EC-LC 4.5Vdc, Schwarzer) was used to pressurize the cell compression device. The voltage supplied to the pump by a DC power supply (HY3005D, Mastech) determined the applied pressure. The pressure supplied by the pump at a given voltage was measured by connecting the outlet of the pump to a pressure gauge (MGA-100-A-9V-R, SSI Technologies) and allowing the pressure to reach a steady state. With a supply voltage of 2.2 V, the resulting pressure was measured to be 33 kPa in gauge pressure.

The height to which balloons could achieve under an applied pressure was determined through topography imaging using a laser scanning confocal microscope (VK-X200K, Keyence). To improve image quality, the device was coated with a layer of powdered chalk (Metolius Super Chalk Sock) to make the device opaque as described in [62]. Inflated balloons were imaged individually on the ultra-fast setting. A magnification ratio of 5x was used for balloon diameters of 1.5, 2.0, and 2.5 mm, and a magnification ratio of 10x was used for balloons with a diameter of 1.0 mm. A z-step size of 16  $\mu\text{m}$  was

chosen to increase imaging speed. Brightness and intensity values were set automatically by the microscope. An area approximately four times the size of the balloon was imaged to ensure that a quality datum could be developed for balloon height measurement.

Then, images of inflated balloons were processed using an in-house MATLAB code to measure the height of the balloons (Appendix A). MATLAB, rather than the microscope software (VK Analyzer), was used to improve our control over image analysis. Repeated analysis of the same data in VK Analyzer revealed an unacceptable level of uncertainty between analyses for the same data set when selecting slightly different sections of the balloon for analysis. Therefore, we adopted our previous image processing method, used to determine the depth of a surface indented by a spherical probe, to determine the balloon height from the obtained images [74]. The image processing procedure is illustrated in Figure 4-3.

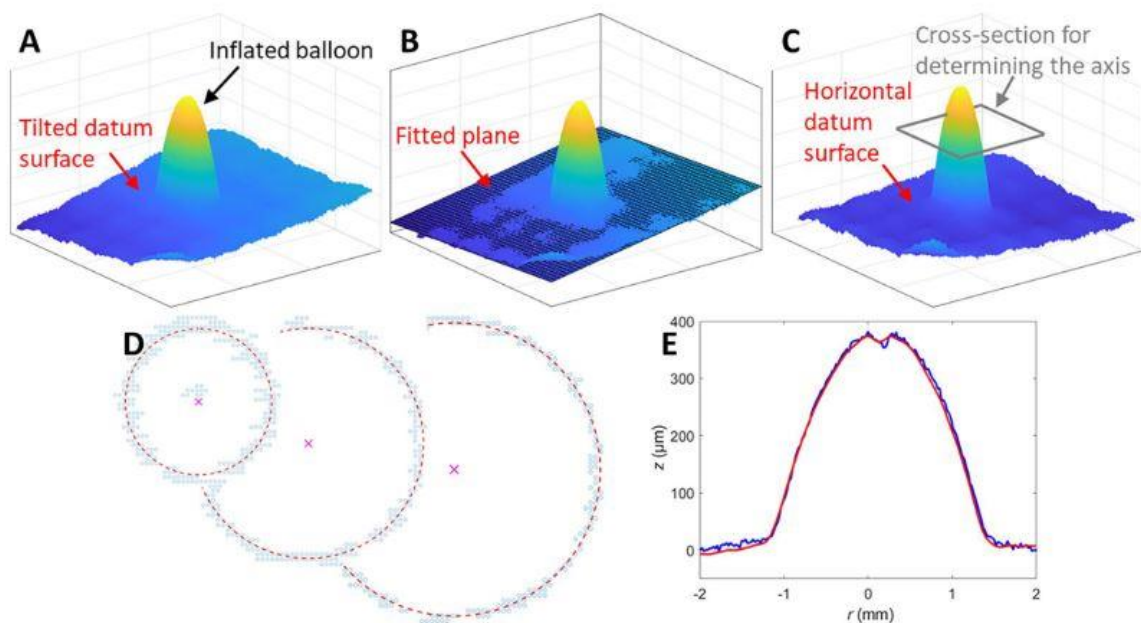


**Figure 4-3:** Image processing procedure. (A) Data from a surface topography image was imported into MATLAB and plotted (not to scale). The base surface (i.e., datum surface) was found to be tilted. (B) A representative plane was found by fitting it to the lower section of the image to correct image tilt. (C) After tilt correction, the datum surface became horizontal. (D) Top-view cross-sections of the balloon at three different  $z$ -values with fitted circles (red dashed circles). The found centers of the cross-sections agreed well with each other. (E) Side-view cross-sections of the balloon with respect to the found axis of symmetry of the balloon.

First,  $z$ -axis values were exported from the microscope software into a Microsoft Excel format. To save memory, only every fourth data point was exported. Second, the data was imported into MATLAB. A Gaussian noise filter was applied to the data to remove noise generated during imaging. The data was visualized and inspected to ensure that the proper file was transferred and to check for data loss (Appendix A lines 1 to 35). As Figure 4-3A shows, inflated balloons were imaged successfully, but the base surface (i.e., the datum surface) was found to be tilted in many cases.

To correct the tilting of the images, a plane to represent the tilted datum surface was found by fitting it to the data through linear least squares regression (Figure 4-3B). To find the plane that best represented the datum of the image, two planes were fitted (Appendix A lines 37 to 64). The first plane was fitted while none of the data was excluded. The second plane was fitted while data was excluded if it was greater than 25% of the maximum  $z$ -value, assuming that such data points belonged to the inflated balloon.

Comparing the two plane fittings, there was minor difference between the planes generated. Between the planes, there was an average difference of  $7\ \mu\text{m}$ , which was insignificant compared to the  $z$ -step size ( $16\ \mu\text{m}$ ) for the imaging. Therefore, it was decided to exclude none of the imported data, multiple plane fittings and tilt corrections were conducted to ensure that the found plane was the base of the image. Planes were fitted until the equation of the plane converged. Figure 4-10B shows that the found plane successfully represented the titled datum surface.

After plane fitting, the tilt of the image was corrected by subtracting the  $z$ -value of the plane from the  $z$ -value of the image at every point (Appendix A lines 65 to 78). This leveled the image as shown in Figure 4-3C and allowed for an accurate balloon height characterization.

Next, several top-view cross-sections (Figure 4-3C) were generated by isolating data at specific  $z$ -values relative to the maximum  $z$ -value (Appendix A lines 80 to 206). As Figure 4-3D shows, extracted data points formed a circular shape at each cross-section. As such, a circle was fitted to the points within each cross-section [75, 74]. The shape of the points and the center of the fitted circle were compared to check if the balloon was axisymmetric, and the circle centers from all cross-sections were averaged to find the center (i.e., axis of symmetry) of the entire balloon. The centers found for each of the cross-sections varied by a maximum of  $3\ \mu\text{m}$ . Compared to the balloon diameter, the center variation was negligible. The  $z$ -value at the found balloon center was designated as the maximum height of the balloon ( $H$ ).

Then, side-view cross-sections of the balloon were generated by plotting the  $z$ -values of the balloon data-column which corresponded to the center of the balloon

(Figure 4-3E). Then, four more cross-sections were generated by using the data within  $\pm$ two columns from the original column. This resulted in five cross-sections in a single direction. The five cross-sections were averaged. Next, this process was repeated by pulling  $z$ -values from the row corresponding to the center of the balloon. This generated a cross-section with a constant column value and a second one with a constant row value, which corresponded to  $xz$ - and  $yz$ -plane cross-sections of the balloon. Finally, the two cross-sections were aligned with respect to the axis of symmetry for comparison (Appendix A lines 212 to 267). The agreement between the cross-sections was an indicator that the balloon was axisymmetric.

#### **4.3.3 Young's Modulus Characterization of PDMS**

From Equation 4-1, it was also expected that Young's Modulus would affect the height response of the balloon to an applied pressure. As such, the Young's Modulus of PDMS was measured to compare this study's results with the theoretical model. Compression testing was performed on cylindrical PDMS samples using a compression tester (Cellscale, Univert) courtesy of Rose Pineda.

PDMS samples were prepared through the following steps. 20 g of PDMS mixed in a 10:1 ratio was poured into a centrifuge tube, which served as the mold, and then the PDMS was degassed for 1.5 hours. The PDMS was cured in an oven at 60°C for 6 hours. Then, the tube and PDMS was removed from the oven and cut into disks using a knife. Care was taken to ensure the cuts were perpendicular to the centrifuge tube to produce a smooth surface for testing. Finally, the remaining tube shell was removed from the

PDMS disk. This produced PDMS disks approximately 15 mm in diameter and 8 mm in thickness.

For the compression test, the PDMS disk was loaded between the plates of the compression tester. A preload was used to ensure full contact between the sample and the plates. Then, the PDMS disk was compressed until a strain of 20% was achieved. After testing, the force and displacement data with a strain below 10% was converted to stress ( $\sigma$ ) and strain ( $\epsilon$ ), and the Young's modulus of PDMS ( $E$ ) was determined by fitting Hook's law:

$$\sigma = E\epsilon \quad , \quad (4-2)$$

with the method of least squares using MATLAB (MathWorks). The criterion of 10% strain was chosen as it was estimated that the balloons of the device would experience lesser strains and show linear-elastic behavior. The procedure was repeated for four samples.

#### **4.3.4 Balloon Diameter Results**

Balloon device molds fabricated with 3D printing were found to have a lower tolerance than previous molds fabricated with photolithography [48]. For the balloon peg imaged and shown in Figure 4-2, with a nominal diameter of 2.5 mm, the diameter was measured to be 2.578 mm. After microscopy imaging of the balloon pegs of the mold, it was seen that the taper added to the pegs slightly misaligned the peg from the microchannel network. This was observed for all balloon pegs of the mold.

The tolerance and printing errors observed are suspected to have two main causes. First, partially cured resin in the printer could obstruct UV light from reaching the region of interest at full intensity. Second, marks on the UV glass of the printer from previous use may impact the UV light. Both of these causes would scatter the UV light, reduce its intensity, and cause tolerance problems during printing. Cleaning of the material vat and UV filter was found to improve the print quality as described in Chapter 2.2, but minor problems still remained.

Since the height of inflated balloons depended on the diameter of the balloons (Equation 4-1) [48], the diameter of the fabricated balloons was measured. As the nominal diameter of the balloons increased, so did the measured diameter for both the mold and the PDMS device. The diameter of the top surface of the air chamber pegs (Figure 4-2A and B) was close to the nominal values of the balloon diameter (Figure 4-4A) since data points are aligned along the red dashed line showing equivalence between two diameters. Also, balloon pegs with the same nominal diameter were found to have similar measured diameters between the three rows. In contrast, the actual balloon diameters measured from the fabricated device (Figure 4-2C) showed some variations for each nominal diameter, and most of them were smaller than nominal values (Figure 4-4B). The actual balloon diameter varied by an average of 7.6% with respect to the nominal diameters.

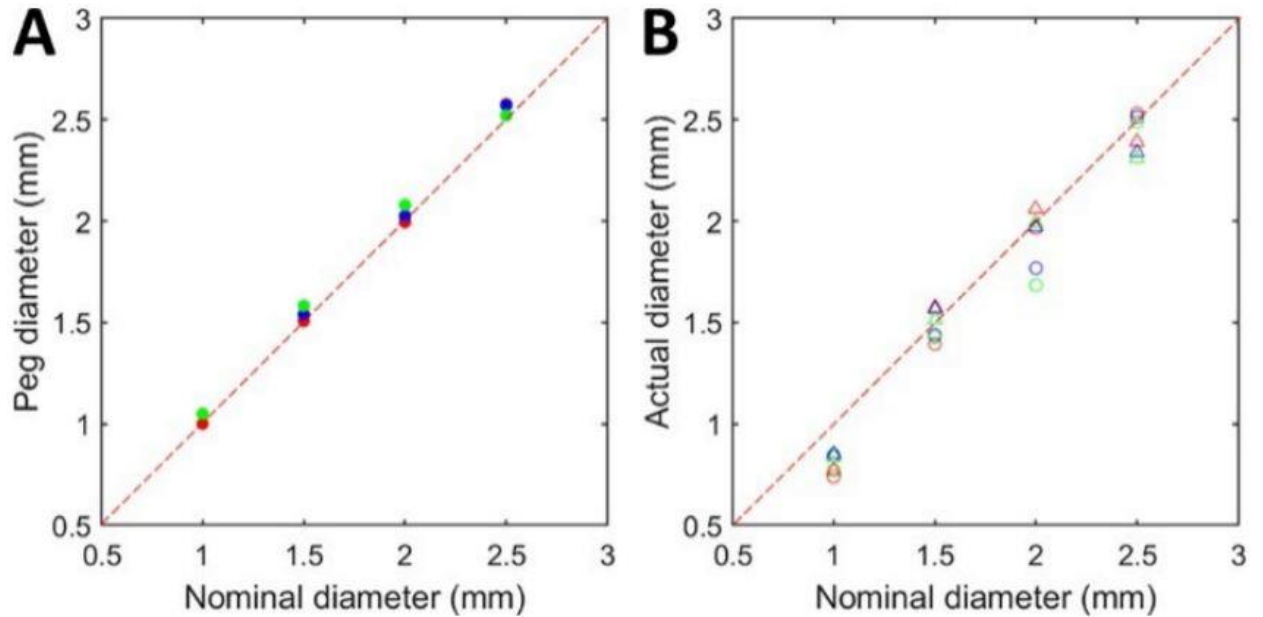


**Figure 4-4:** Comparison with nominal balloon diameters. (A) Measured diameters of the top surface of balloon pegs. (B) Measured diameters of PDMS balloons. Red, blue, and green colors indicate the balloon rows numbered 1, 2, and 3 in Figure 4-1B, respectively.

Variations in the balloon diameter may be caused by the taper on the balloon cavity or tearing of the PDMS when removing it from the mold. Tapering of the balloon cavity may have slightly increased the diameter of the balloons causing thinner regions of PDMS. Tearing of the PDMS during removal from the mold may have increased the effective diameter of the balloons as well by increasing the size of the balloon cavity. Due to these reasons, the diameter of the balloon was taken to be the diameter measured from the PDMS body of the device.

#### 4.3.5 Balloon Height Results from Image Processing

In this study, the balloon microfluidic devices with different balloon thicknesses ( $t = 71$  and  $132 \mu\text{m}$ ) were fabricated and tested for the dependence of the balloon height on the balloon thickness. The applied gauge pressure was 33 kPa in this study.

The developed in-house MATLAB code for automated image processing could measure the balloon height successfully. It was found that tiling correction was crucial for consistent and accurate measurements of the balloon height (Figure 4-3A to C). Without tilt correction, the balloons did not appear symmetric when observing their top-view cross-sections. Additionally, the side-view cross-sections appeared skewed.

After tilt correction, the inflated balloon appeared to be a symmetric spherical cap. Circle fitting to top-view cross-sections of the balloon confirmed that the inflated balloon had circular cross-sections and was axisymmetric because the centers of the fitted circles were close to each other (Figure 4-3D). This enabled determining the axis of symmetry of the balloon, measuring the balloon height, and plotting side-view cross-sections [74]. As shown in Figure 4-3E, two side-view cross-sections agreed well with each other and were symmetric with respect to the axis of symmetry. Therefore, the inflated balloon was axisymmetric.

A small dent was observed at the peak of the balloon in Figure 4-3E, but it should be pointed out that this dent is exaggerated considering the scale difference between the vertical and horizontal axes. When plotted with the same scale for the two axes, this dent appeared rather flat. Such dents appeared on 10% of the samples. This dent appeared to be an imaging artifact and did not affect the measurement quality of  $H$  because the

maximum depth of dents ( $6\ \mu\text{m}$ ) was smaller than the  $z$ -step size of microscopy imaging ( $16\ \mu\text{m}$ ).

The measured values of balloon height are shown in Figure 4-5. The current microfluidic device had balloon heights ranging from  $28\ \mu\text{m}$  to  $380\ \mu\text{m}$  with an applied pressure of  $33\ \text{kPa}$ . Overall, the balloon height increased with the balloon diameter. Note that the shown diameter values are actual balloon diameters, not nominal ones. For the largest balloons ( $D = 2.5\ \text{mm}$ ), the balloon height varied significantly while actual balloon diameters did not. In contrast, the other cases showed relatively similar heights for similar diameters.

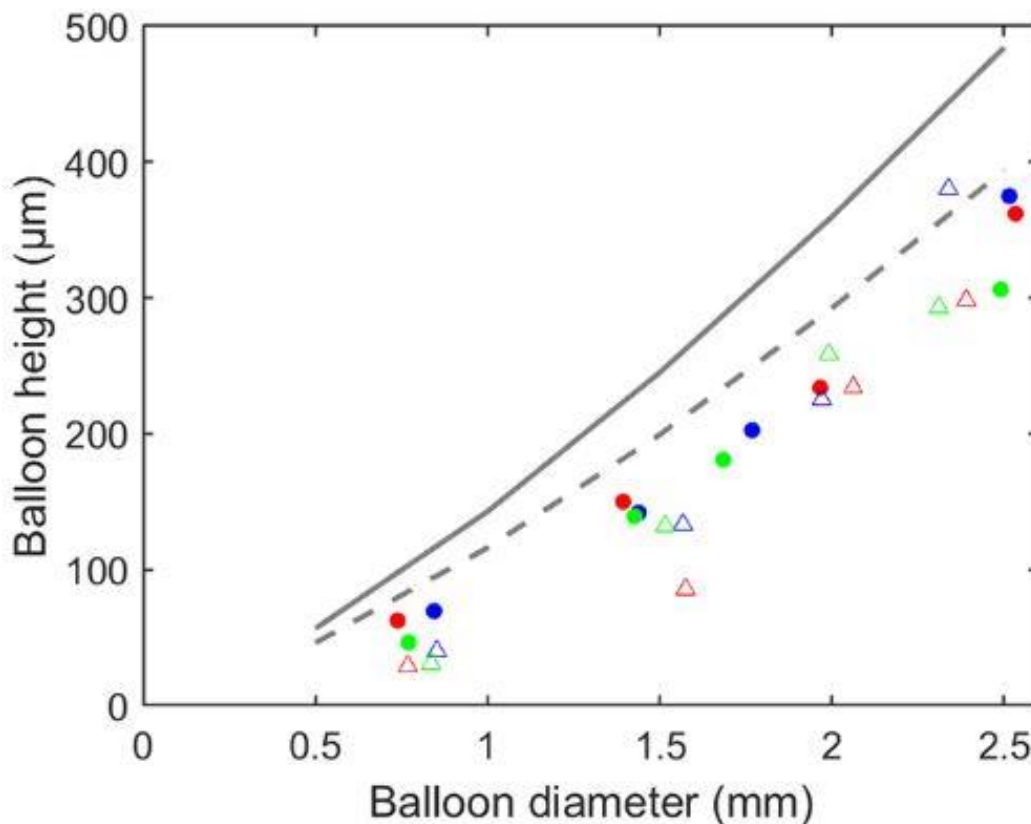


**Figure 4-5:** Measured height of the inflated balloon found through image processing ( $H$ ) as a function of the measured balloon diameter from the PDMS body ( $D$ ). A gage

pressure of 33 kPa was applied to two cell compression devices with balloon layer thicknesses of  $t = 71 \mu\text{m}$  (circles) and  $132 \mu\text{m}$  (triangles). Red, blue, and green colors indicate the balloon rows numbered 1, 2, and 3 in Figure 4-1B, respectively. The solid and dashed gray curves show theoretical predictions of  $H$  for  $t = 71 \mu\text{m}$  and  $132 \mu\text{m}$ , respectively.

Although our results show overall dependence of the balloon height on the balloon diameter, as expected, the dependence of the height on balloon thickness was not clear. In Figure 4-5, balloon height values did not show significant differences between the device with  $t = 71 \mu\text{m}$  and the device with  $t = 132 \mu\text{m}$ . Smaller balloons (i.e.,  $D \leq 1.5 \text{ mm}$ ) showed lower  $H$  with an increase in  $t$  as expected whereas larger balloons (i.e.,  $D > 2 \text{ mm}$ ) did not.

The measured diameters of the balloons fabricated from the same balloon peg of the mold showed disagreement as shown in Figure 4-4B. This mismatch would impact the height of the balloons due to their dependence on balloon diameter (Equation 4-1), as well as increase the difficulty of data analysis for the dependence of the balloon heights on balloon layer thickness.

Although some balloons had similar measured diameters with the same thickness, they still showed different heights. This may indicate that the balloon heights have a relatively weak dependence on the balloon thickness compared to the other parameters that determine balloon height. Using Equation 4-1, the following dependence of  $H$  on  $t$  and  $D$  can be seen.

$$H \sim D^{\frac{4}{3}} t^{-\frac{1}{3}}, \quad (4-3)$$

Therefore,  $D$  will have a much greater impact on  $H$  compared to  $t$ . Error introduced during imaging, image processing, and PDMS diameter measurements could have also contributed to the deviation of the balloon heights from the theoretical model, which is introduced in the following section, and each other.

#### 4.3.6 Young's modulus of PDMS

Compression testing of PDMS was conducted to determine its  $E$  value for use in Equation 4-1 as described previously. The stress-strain data of an exemplary case is shown in Figure 4-6. The data showed slight non-linear behavior, which was also observed in our previous compression test on PDMS [76]. With linear elasticity being assumed, Equation 4-2 was fit to the data. The determined  $E$  value was  $2.31 \pm 0.15$  MPa ( $n = 4$ ). This value agreed well with our previous elasticity measurement of PDMS ( $2.90 \pm 0.16$  MPa for the 10:1 ratio) [76] and was used for predicting  $H$  using the theoretical model.

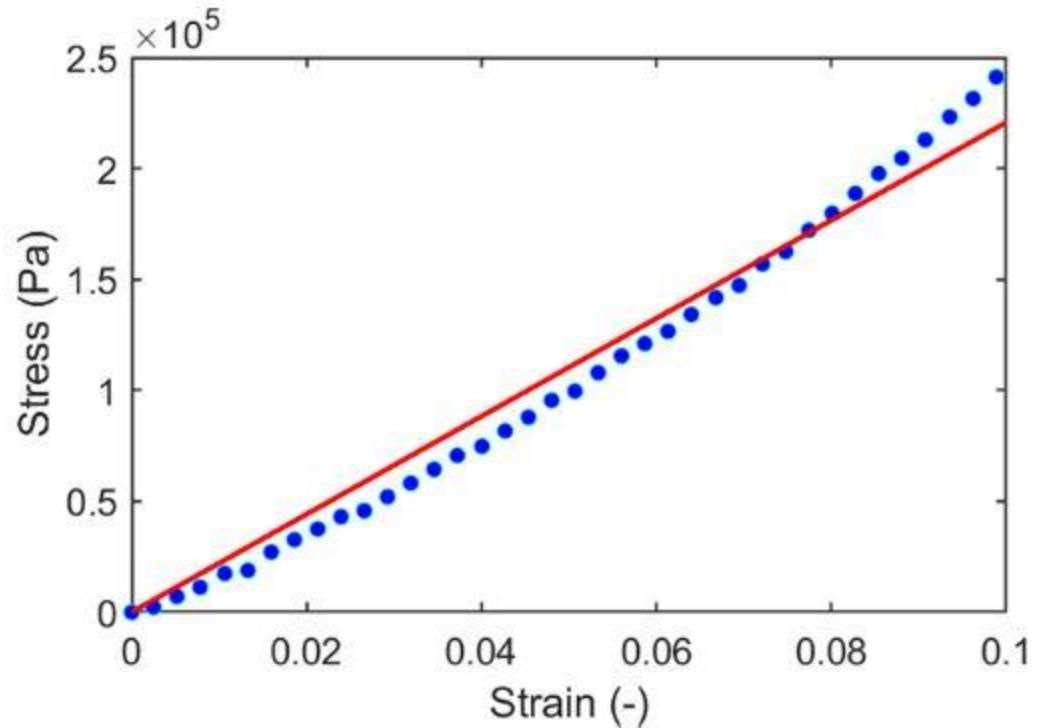


**Figure 4-6:** Experimentally measured stress-strain data of a PDMS sample with a diameter of 13.7 mm via the compression test. Red line: Hook's law (Equation 4-2).  $E = 2.21$  MPa. The shown stress and strain are magnitudes of compressive stress and strain.

#### 4.3.7 Comparison with a Theoretical Prediction

Previously we used Equation 4-1 for estimating the height of inflated balloons [73]. In our previous study, this model underpredicted the balloon height but it qualitatively agreed with experimentally measured balloon heights [48].

Figure 4-5 shows balloon heights predicted using Equation 4-1 in this study. Overall, Equation 4-1 overpredicted the balloon height in comparison to the experimentally measured  $H$  values. The theoretical model predicted that the device with  $t = 132$   $\mu\text{m}$  should have 19% smaller  $H$  than one with  $t = 71$   $\mu\text{m}$  for the same  $D$ . However,

the heights measured from the inflated device were not characteristically different as the theoretical model predicted.

The disagreement of the experimental data to Equation 4-1 may be due to the assumptions used when developing the equation. Equation 4-1 assumes that  $H \ll D/2$  and that the balloons are perfectly symmetric. As Figure 4-5 shows, the height of the balloon was typically around 25% of the balloon diameter, which may not satisfy the first assumption. Additionally, the disagreement may be caused by uncertainty during imaging and tilt correction during image processing. Although the generated planes show good agreement, it was not confirmed to be the true base of the device.

The quality of fabricated microfluidic cell compression devices may affect the reliability of the theoretical model as the model heavily depends on the diameter and symmetry of the balloons. Although the cross-sectional views of the balloons point towards good balloon symmetry (Figure 4-3E), there were still variations in the balloon diameter in different directions for certain balloons.

Although confocal laser scanning microscopy and image processing was used to measure balloon diameter and balloon height, it was not ideal for characterizing the balloon microfluidic device for the following reasons. First, the balloon diameter and balloon height measurements were time consuming. Measuring balloon diameter and height measurements took approximately 3 to 4 hours for a single device. Additionally, the results from the diameter and height measurement varied significantly from the theoretical model. Later this method was found to need improvement due to the level of noise in the obtained image and the level of data smoothing required to process the

image. As such, a faster and more accurate method for balloon diameter and height characterization using brightfield microscopy was developed.

#### **4.4 Inverted Brightfield Microscopy for Balloon Characterization<sup>7</sup>**

To improve the characterization of the balloons of the microfluidic device, brightfield imaging with an inverted microscope (Olympus IX81) was used to measure the diameter and height of the balloons of the microfluidic balloon device. The following procedure could be used for balloons with diameters between 1.0 mm to 2.5 mm. The following sections describe the improved methodology for measuring diameter and height of the balloons and their results.

##### **4.4.1 Balloon Diameter Measurement**

To characterize the balloons, the diameter was measured first as described in [69]. First, the inverted brightfield microscope was used to image a scale reference and the balloons. Imaging of the scale bar and balloons occurred under a magnification of 4× to ensure that the entire balloon could be seen within a single image. Balloons with a nominal diameter of 1.0, 1.5, 2.0, and 2.5 mm were imaged.

After imaging, the balloon diameter was measured by fitting a circle to the circumference of the balloon using Kasa's method [75] and an in-house MATLAB code as shown in Appendix B. First, the image of the balloon and the scale was loaded into

---

<sup>7</sup> Accepted for presentation in the American Society of Mechanical Engineers conference of Fluids Engineering Division Summer Meeting 2024. C. Emeigh and S. Ryu, Using brightfield microscopy to assess the balloon expansion performance of a microfluidic cell compression device, ASME FEDSM 2024-130787.

MATLAB (Appendix B lines 1 to 16). Second, three points along the balloon's circumference were manually input into the code through clicking the image (Appendix B lines 18 to 27). Finally, the circle was generated and plotted on top of the image as seen in Figure 4-7 (Appendix B lines 31 to 72).

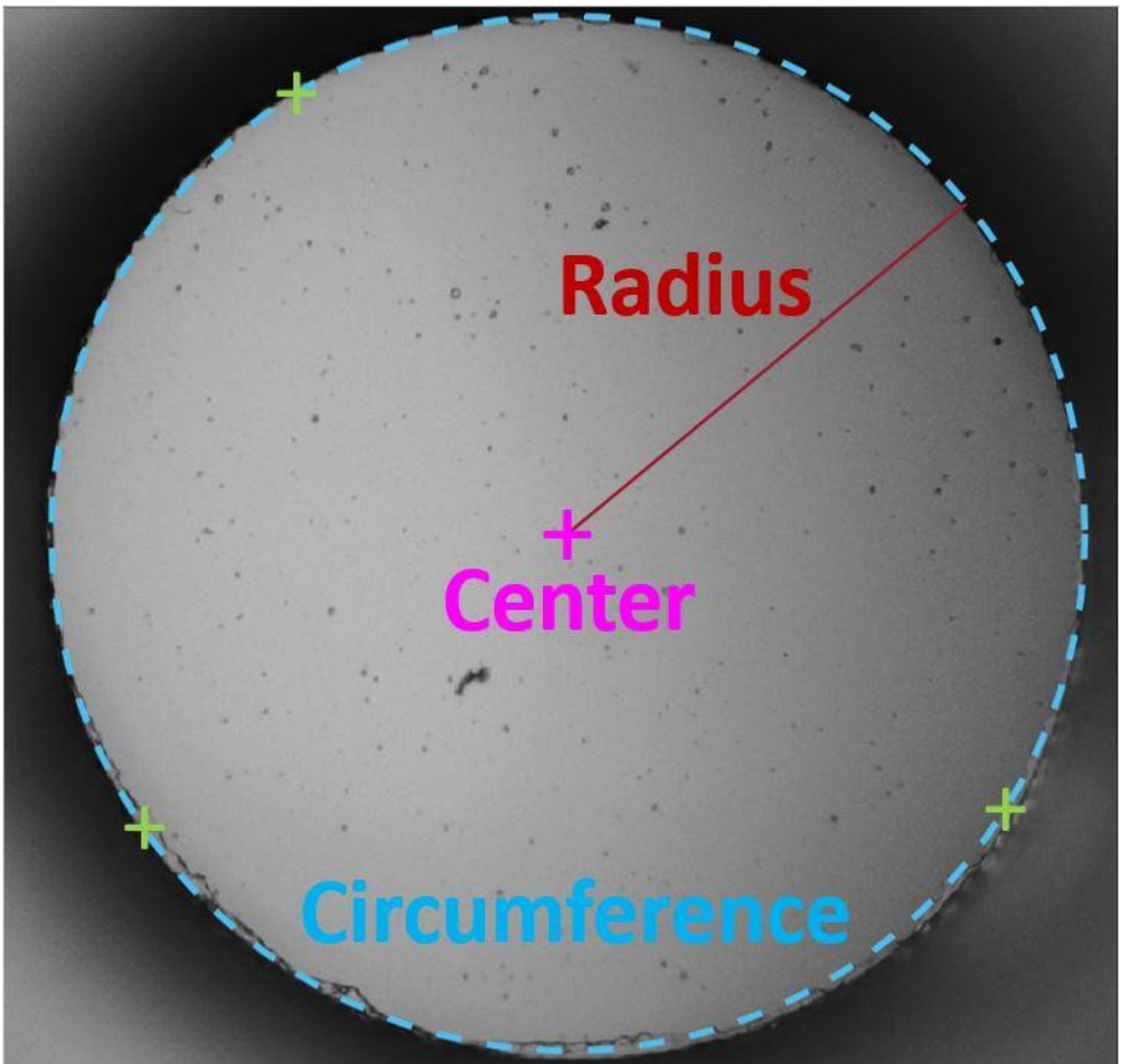


**Figure 4-7:** Balloon diameter measurement using circle fitting [75]. This balloon had a nominal and measured diameter of 2.5 mm and 2.55 mm, respectively.

The radius of the fitted circle was assumed to represent the radius of the balloons, and it is shown as a red line in Figure 4-7. The center of the circle and the circumference of the circle is shown as a pink “+” and a blue dashed line, respectively. The green “+” represents the manually chosen locations for circle fitting. For the diameter measurement shown in Figure 4-7, the nominal and measured diameters were 2.5 mm and 2.55 mm, respectively. The difference between the nominal diameters and the measured diameters was similar when using the MATLAB-based approach or the ImageJ method.

#### **4.4.2 Top-View Imaging of the Inflated Balloons**

Once the balloon diameters had been measured, the balloons were prepared for height measurement. For more accurate measurements of balloon heights, the balloons of the microfluidic device were first coated with microspheres to allow for easy focusing of the upper surface of the balloon and the base of the device (Figure 4-1C). A 25% concentration of 10  $\mu\text{m}$ -diameter polystyrene microspheres (Phosphorex) was deposited onto the top surface of the device. Microspheres with a diameter of 10  $\mu\text{m}$  were chosen as they were the smallest microspheres that could be seen at 4 $\times$  while still minimizing error in the height measurements due to the microsphere application. A concentration of 25% was used as we could see individual microspheres while still being able to coat the entire balloon. When applying the solution, care was taken to ensure that the entire balloon, as well as some of the base surface, was coated with microspheres. Next, the microsphere solution was dried by placing the device in a vacuum for 2 hours.

After applying microspheres to the device, the cell compression device was pressurized. Hydrostatic pressure was used to inflate the balloons instead of the previously used pneumatic pump, as hydrostatic pressure is steady and easily controllable. The application and level of the hydrostatic pressure was controlled by suspending a water bath at a specific height above the microfluidic device and connecting the two with plastic tubing. In this study, 14 kPa of hydrostatic pressure was applied by having a 1.43 m height differential between the water bath and microfluidic device. The device was left overnight, connected to the hydrostatic pressure, to fill the device with water and to remove any air bubbles entrapped in the device.

To measure the balloon height, the device was placed under the same inverted microscope for top view imaging as shown in Figure 4-8A. Figure 4-8B to 4-8E shows images of a balloon with a nominal diameter of 2.5 mm when the microscope's focal plane was at different  $z$ -values. First, the center of the balloon was determined by observing the balloon in 4 $\times$  and moving the focal plane of the microscope up and down. When moving the focus of the microscope, rings at a specific height were in focus. As the focus was moved up, the focused ring of microspheres converged to a single point which was assumed to be the center of the balloon (Figure 4-8B to Figure 4-8E).

Next, the microscope was iteratively moved from 4 $\times$ , to 10 $\times$ , and to 20 $\times$  magnification to ensure the center of the balloon was still within the image. Köhler illumination was performed when switching between microscope objectives to ensure even illumination and maximum contrast [77, 78]. Once at 20 $\times$ , the focal plane of the microscope was adjusted such that the microspheres at the center of the balloon were in

focus (Figure 4-8E inset). The  $z$ -value of the focal plane was read using the software of the microscope (CellSens Dimension, Olympus).

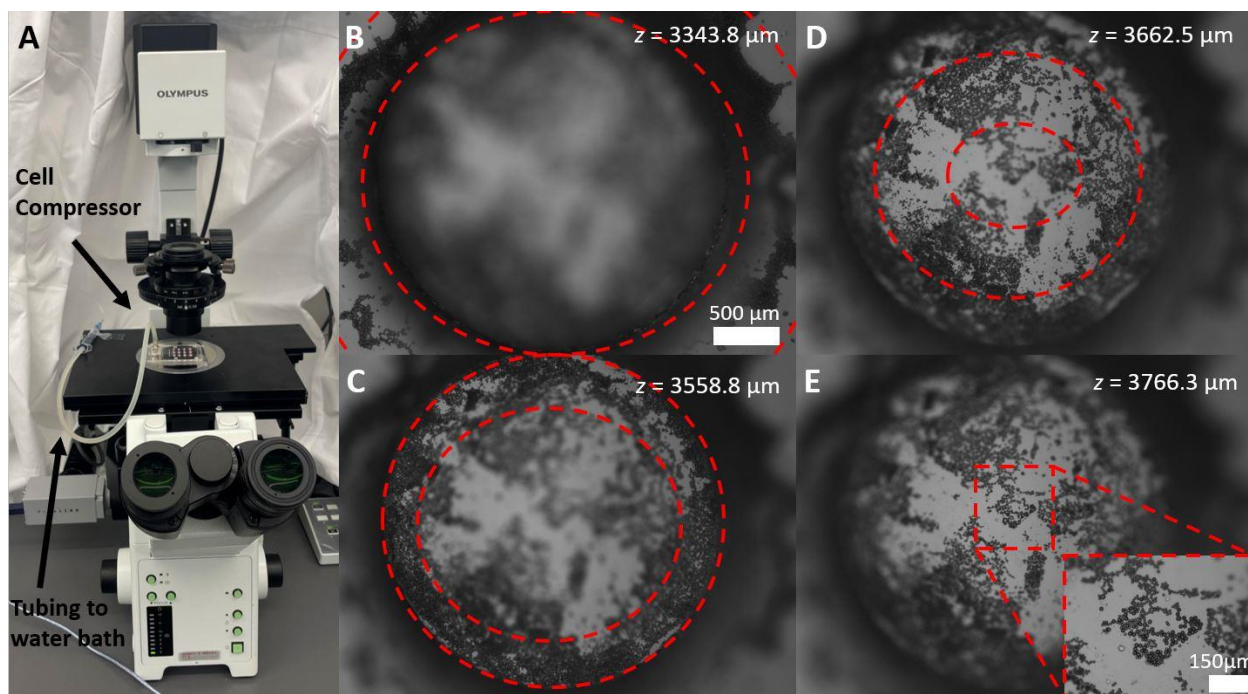


**Figure 4-8:** (A) Brightfield microscopy imaging setup for balloon height measurement.

The water bath was placed 1.43 m above the device to inflate the balloons of the device.

(B-E) Top-view images of an inflated balloon (nominal diameter: 2.5 mm, and height: 515  $\mu\text{m}$ ) at 4x. The area of focused microspheres, which is indicated as the region between the red dashed circles, changed as the  $z$ -location of the focal plane changed.

Inset in (E): 20x view of the center of the balloon.

Next, the  $z$ -value of the base of the device was measured in the same way. The difference in  $z$ -values between the center of the balloon and the base of the device was

taken to be the height of the balloon. Measurement of the balloon height of the same device was conducted 3 times to show repeatability.

To convert the balloon height value measured from the microscopy imaging to a true physical value, a correction factor was measured by imaging glass coverslips coated with microspheres as a gauge sample. First, two glass coverslips were coated with microspheres. The coverslips were placed together with the microsphere-coated sides facing outward. The thickness of the coverslip stack was measured using a micrometer and then the microscopy imaging method. This process was repeated for stacks of 2 to 5 coverslips. From the data, a correction factor ( $X_{air}$ ) of 1.215 was found to convert the  $z$ -values from the microscope into physical values as shown in Figure 4-9. Upon repeating this coverslip calibration twice, this correction factor was found to be consistent.

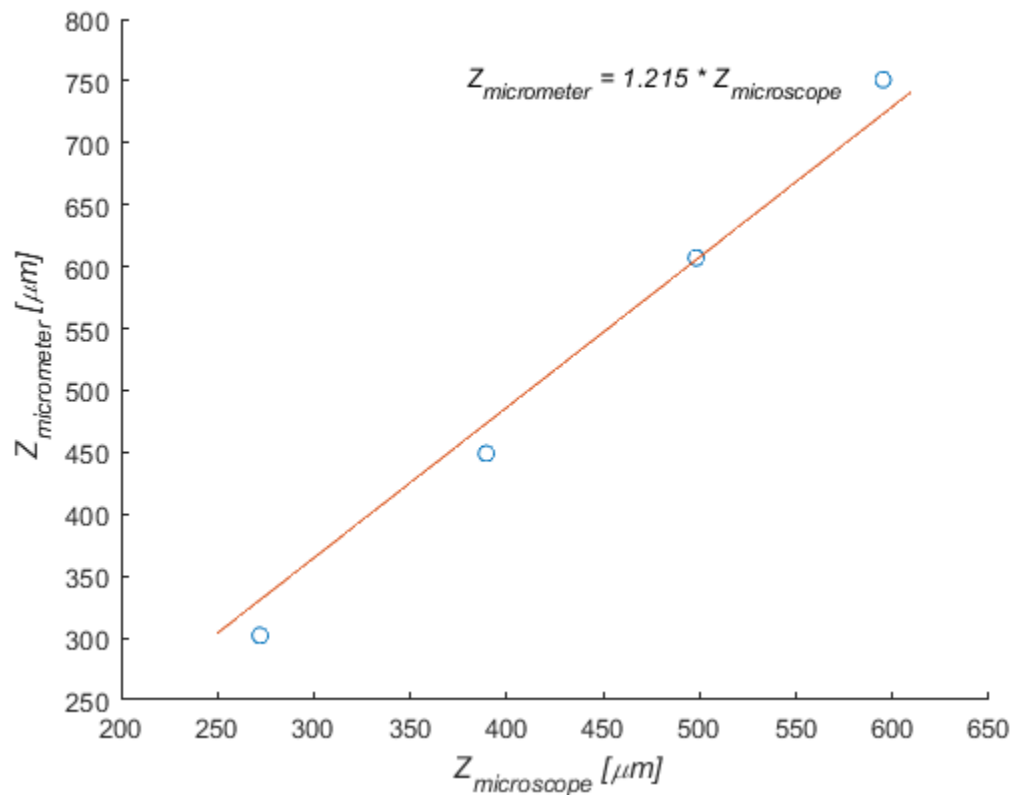


**Figure 4-9:** Coverslip calibration data to convert  $z$ -values from the microscope software into physical  $z$ -values. The correction factor was found to be  $X_{air} = 1.215$ .

#### 4.4.3 Side-View Imaging of the Inflated Balloons

For side-view imaging of the balloons a goniometer (Attention Theta, Biolin Scientific) was used. Once pressurized by 14 kPa of hydrostatic pressure as aforementioned, the device was placed onto the stage of the goniometer. A syringe was placed within the frame of the image to serve as a reference scale (Figure 4-10). The device was then moved such that the balloon of interest was in focus. The device was also rotated so that balloons on other areas of the device did not impact imaging of the balloon of interest. Once in focus, an image of the balloon was taken. Only balloons with a diameter of 2.5 mm were imaged because balloons with smaller diameters did not inflate enough for sideview imaging. After imaging, ImageJ was used to determine the height of the balloon by measuring the distance between the top of the balloon and the base of the device (Figure 4-10).

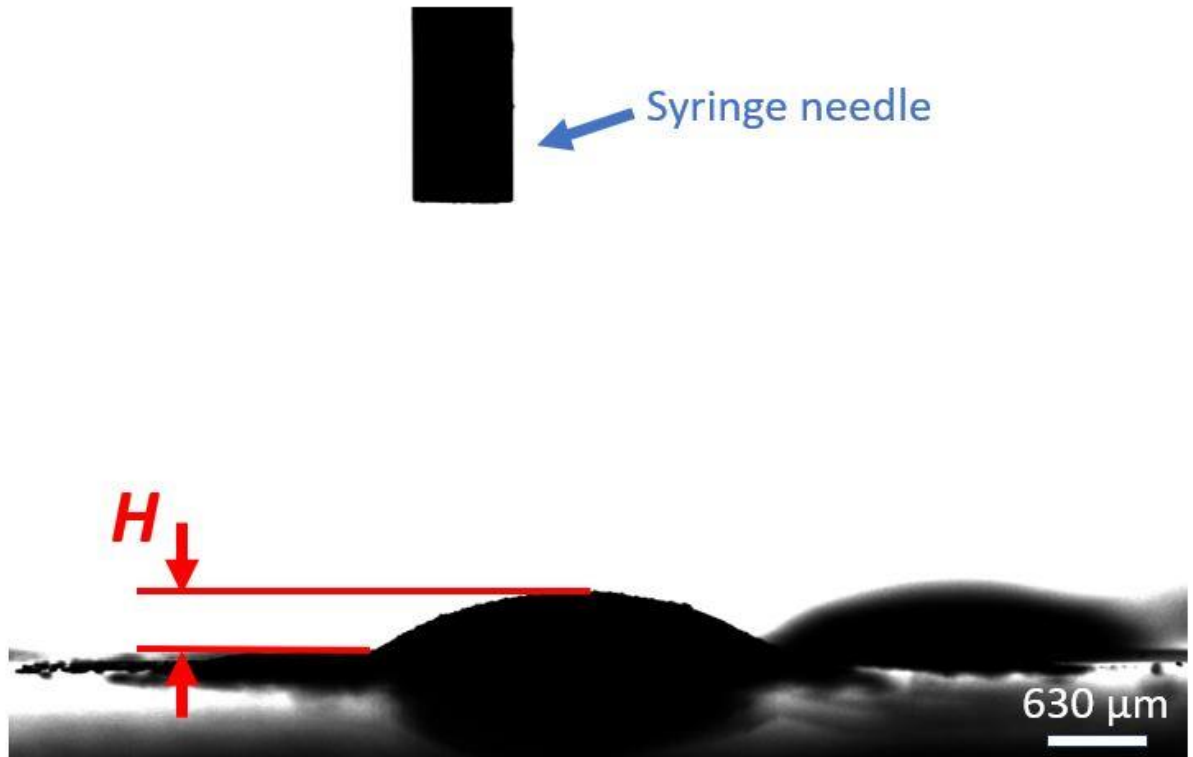


**Figure 4-10:** Side-view imaging of a 2.5 mm-diameter balloon using the goniometer camera. The height was found to be  $493 \pm 6 \mu\text{m}$ . A syringe needle is included in the image as a scale.

#### 4.4.4 Results of Diameter Measurement

The fabricated devices had easily controlled, highly consistent balloon diameters as shown in Figure 4-11: as the balloon's nominal diameter increased, the measured diameter also increased nearly proportionally to the nominal diameter. The variation in balloon diameter was similar regardless of the nominal balloon diameter. When comparing the measured diameters to the nominal diameters, the average error was 5.0% with a standard deviation of 0.8% ( $n = 3$ ). Less diameter variation was observed using

Kasa's method and MATLAB compared to previous methods using ImageJ as shown in Figure 4-4B. Additionally, the device fabrication was slightly changed by increasing the height of the balloon pegs of the mold to remove PDMS from above the balloon cavity.

Because the diameter of the balloons has a high level of control on the final balloon height, improving the balloon fabrication method and the diameter measurement method proved beneficial in predicting the balloons' behavior. Changing the mold design such that its balloon pegs were 30  $\mu\text{m}$  taller than the spacers or the outer wall improved the balloon diameter control. Additionally, curing each layer of the 3D printed mold for 4.5 seconds improved the 3D printer's ability to print small channel features. Increasing the layer curing time may also have increased the likelihood of over solidification when fabricating the mold, and thus slightly increasing the diameter of the balloons, and reducing the resolution of the 3D printer.

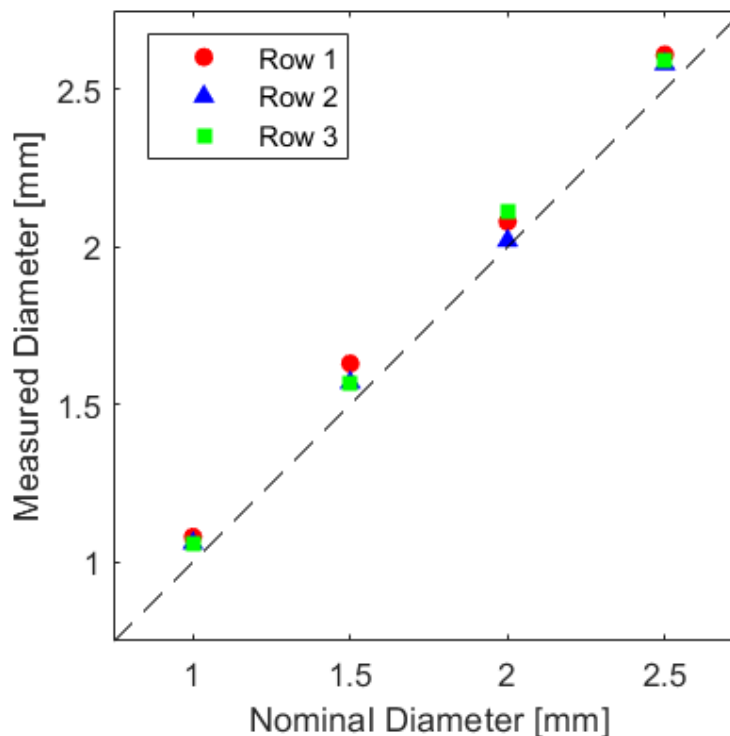


**Figure 4-11:** Measured balloon diameters compared to nominal balloon diameters. The dashed line indicates the ideal case where the measured balloon diameters equal the nominal balloon diameter values.

Although the new design of the 3D printed mold and improved fabrication procedure reduced balloon diameter variation, the balloon diameters still varied. Variations in the balloon diameters of the device may be caused by over solidification of resin by the 3D printer. Incomplete removal of the PDMS above the balloon chambers when removing the PDMS body from the mold may also impact the effective diameter of the balloons. Separation of the spin-coated PDMS layer and the PDMS body during use may also affect the balloon diameter.

Even with this limitation, 3D printing is still an attractive alternative to photolithography as 3D printing has the following advantages. First, the design flexibility of 3D printing is much higher due to easy design changes and the ability to create more complex 3D geometries. Second, 3D printing is much faster than photolithography. Photolithography usually takes about a week to create a high-resolution photomask and to fabricate a master mold. In contrast, 3D printed molds can be designed and completed in less than 5 hours total. Third, 3D printing is much cheaper than photolithography. A 3D printed mold costs approximately \$5 per mold while photolithography molds cost far more while requiring more expensive equipment.

#### 4.4.5 Inflated Balloon Height vs Balloon Diameter

In this study, we measured balloon height through top-view imaging using an inverted brightfield microscope and microspheres for ease of focusing, and side-view imaging using a goniometer camera. Balloons with diameters of 1.0, 1.5, 2.0, and 2.5 mm were imaged in the top view. For side-view imaging, only balloons with a diameter of 2.5 mm could be imaged due to the resolution of the goniometer's camera. Three balloons were measured for each diameter, and the top-view imaging was conducted three times for each balloon, while the side-view imaging was conducted twice, to show repeatability in the imaging technique.

Overall, it was found that as the balloon diameter increased, balloon height also increased as shown in Figure 4-12. Balloons with a nominal diameter of 1.0, 1.5, 2.0, and 2.5 mm had an average height of  $204 \pm 3.3 \mu\text{m}$ ,  $287 \pm 7.1 \mu\text{m}$ ,  $386 \pm 9.8 \mu\text{m}$ , and  $509 \pm 8.6 \mu\text{m}$ , respectively. Repeated measurements show little variation.

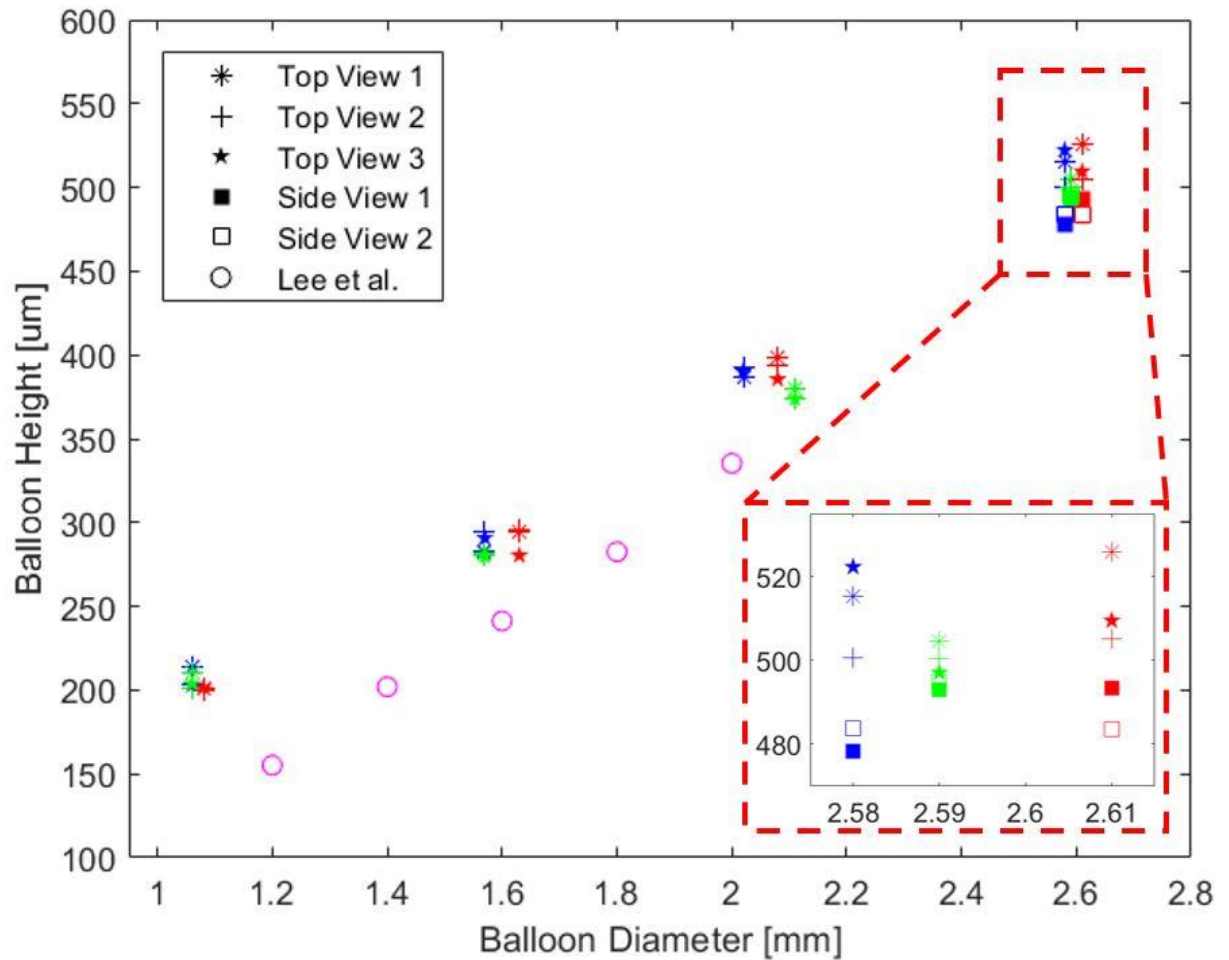


**Figure 4-12:** Measured inflation height of the balloons ( $H$ ) as a function of balloon diameter ( $D$ ). Balloons with  $58\ \mu\text{m}$  thickness and nominal diameters of 1.0, 1.5, 2.0, and 2.5 mm were measured under an applied hydrostatic pressure of 14 kPa in the top-view. Previously obtained data from Lee et al. are included for comparison [48]. Inset: Magnified view of measurements for the balloon with a nominal diameter of 2.5 mm. See the legend of Figure 4-11 for colors.

Comparing the data obtained from top-view imaging and side-view imaging, it seems that there is little difference in the measured values. The top-view imaging had an average balloon height value of  $509 \pm 10\ \mu\text{m}$  while side view imaging had an average

height of  $488 \pm 9 \mu\text{m}$ . As such, between the two measurement methods, there was an error of 4.1%. Top-view imaging was preferred over side-view imaging due to its ability to image balloons of any diameter. The new measurement method appears to be repeatable and has been validated through the secondary side-view imaging measurement.

The found heights were compared with the data obtained previously [48]. In the previous study, the cell compression device was fabricated using photolithography, and the balloon heights were measured using confocal laser scanning microscopy. Additionally, the balloons had approximately the same thickness ( $58 \mu\text{m}$ ) and were subjected to approximately the same level of pressure (14 kPa). Overall, it appears that the data obtained in this study shows qualitative agreement with the previous data.

Although there is disagreement between the data sets, this was expected due to the following differences. First, the two devices had different fabrication techniques, different pressurization methods, and different balloon diameters. Additionally, the device fabricated with photolithography was imaged using confocal laser scanning microscopy, while the device fabricated with 3D printing used inverted brightfield microscopy.

In Section 4.3, laser scanning confocal microscopy and MATLAB-based image processing was used to measure the height of inflated balloons on the device [67]. Although confocal microscopy could produce the 3D image of inflated balloons, measurements with confocal microscopy did not show a high level of repeatability and the measurements contained a great amount of noise. Uncertainties within the confocal

microscopy image data may be due to the transparency of the device, small size of the device, image stitching effects, and image processing uncertainties.

As such, top-view imaging using brightfield microscopy was used as an alternative for balloon height measurement to improve accuracy and repeatability. This method is quicker, typically costs less, and is generally more accessible. Inverted brightfield microscopy has been validated using separate imaging techniques. Finally, surface preparation for brightfield microscopy was simpler and much quicker compared to that for laser scanning confocal microscopy.

#### **4.4.6 Discussion of the Top- and Side-View Imaging Methods**

During balloon height measurement with top-view microscopy imaging, the following sources of error may have impacted the measured height. First, although the size of the microspheres was minimized and imaging magnification was maximized to reduce error, the microspheres applied to the balloon may introduce error. Microspheres with a diameter of 10  $\mu\text{m}$  and a concentration of 25% were used to coat the balloons of the device as individual particles could be identified during imaging while the size was comparable to the thickness of the focal plane. Additionally, a particle concentration of 25% was used to prevent particles from stacking on-top of each other, which would further introduce error. Despite these considerations, the microspheres may have increased the measured height of the balloon due to their application.

Second, focusing on the sample may introduce error due to the thickness of the focal plane. During volumetric illumination, microspheres near the edge of the focal

plane may also appear in focus. To minimize this error, a 20x objective lens was used to minimize the thickness of the focal plane while still being able to image the top of the balloon. Although a 40x objective lens was available, its working distance was too small to image the tallest balloons. When imaging with the 20x objective, the focal plane thickness (*DOF*) was calculated to be approximately 11  $\mu\text{m}$  using the following equation [77, 78].

$$DOF = \frac{3\lambda n}{NA^2} + \frac{n}{M*NA} e \quad , \quad (4-4)$$

where  $\lambda$  is the wavelength of light used for illumination,  $n$  is the refractive index of the media between the objective and the sample (1 for air),  $NA$  is the numerical aperture of the microscope objective (0.45),  $M$  is the magnification (20x), and  $e$  is the smallest resolvable distance of the camera sensor (0.5  $\mu\text{m}$ ). Since white light ( $\lambda = 300\text{-}780 \text{ nm}$ ) was used for illumination in this study, a  $\lambda$  of 780 nm was used for a conservative estimation.

During side-view imaging of the balloon height, the following sources of error may impact the height measurement. First, the resolution of the camera limited the minimum height difference able to be measured. From the side-view images, the size of each pixel was calculated to be near 5  $\mu\text{m}$ . As such, the smallest balloons were less than 40 pixels and could not be seen during analysis. Second, when imaging a balloon of interest, interference from other balloons on the device may reduce image quality and affect the measured height. Third, processing the images with ImageJ may have

introduced uncertainty into the found results due to manually locating the base surface in the side-view images.

Overall, despite these sources of error, our measurements were shown to be repeatable and have been validated using two different methods. As such, balloon height measurement using top-view microscopy imaging can be used reliably and proves to be an efficient method.

## Chapter 5: Flow Characterization Using PTV

### 5.1 Introduction (What is PTV?)

To understand the level of wall shear stress within a microfluidic channel, the flow field must be characterized. Particle tracking velocimetry (PTV) is a common technique for measuring the velocity field of a flow by imaging tracer particles within the flow and individually tracking each particle [79]. PTV requires that the imaged flow has a low number density of particles [80]. A schematic overview of PTV is shown below in Figure 5-1.

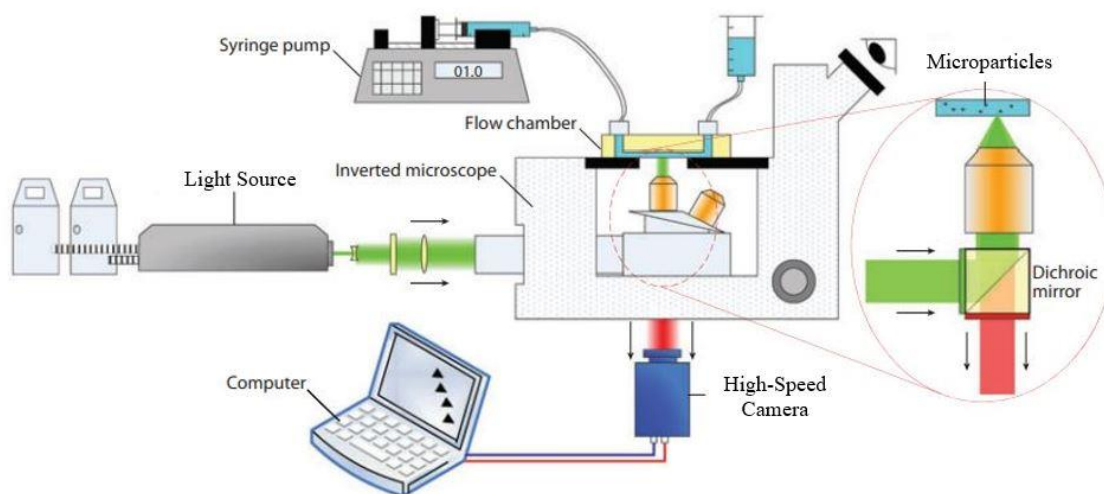


**Figure 5-1:** A schematic overview of a typical PTV experiment. An inverted microscope is used to image tracer particles within the flow of a microchannel. The image is recorded by a high-speed camera for further data analysis. Adapted from [81].

PTV analysis requires two components, imaging of tracer particles within a flow and image processing. Tracer particles can either be naturally in the fluid or artificially

added. To ensure the particles imaged during PTV accurately trace the flow and can be imaged with a high signal-to-noise ratio, tracer particles must be neutrally buoyant, large enough to negate the effects of Brownian motion, and smaller than the characteristic length of the flow [82, 83]. After imaging, the velocity of the flow at the imaging location can be determined by comparing multiple image frames and correlating the position of the particles within each frame.

During brightfield microscopy imaging, the flow field is imaged through volumetric illumination as shown in Figure 5-2. In other words, a small volume of the flow is illuminated and in-focus in the resulting image, which is known as the focal plane. As such, only tracer particles within the focal plane are in-focus. Therefore, during imaging, only a small portion of the channel can be imaged laterally and depth-wise. When performing PTV, imaging must be repeated with the focal plane at various channel  $z$ -values to fully understand the velocity profile of the flow at the particular imaging  $xy$ -location.

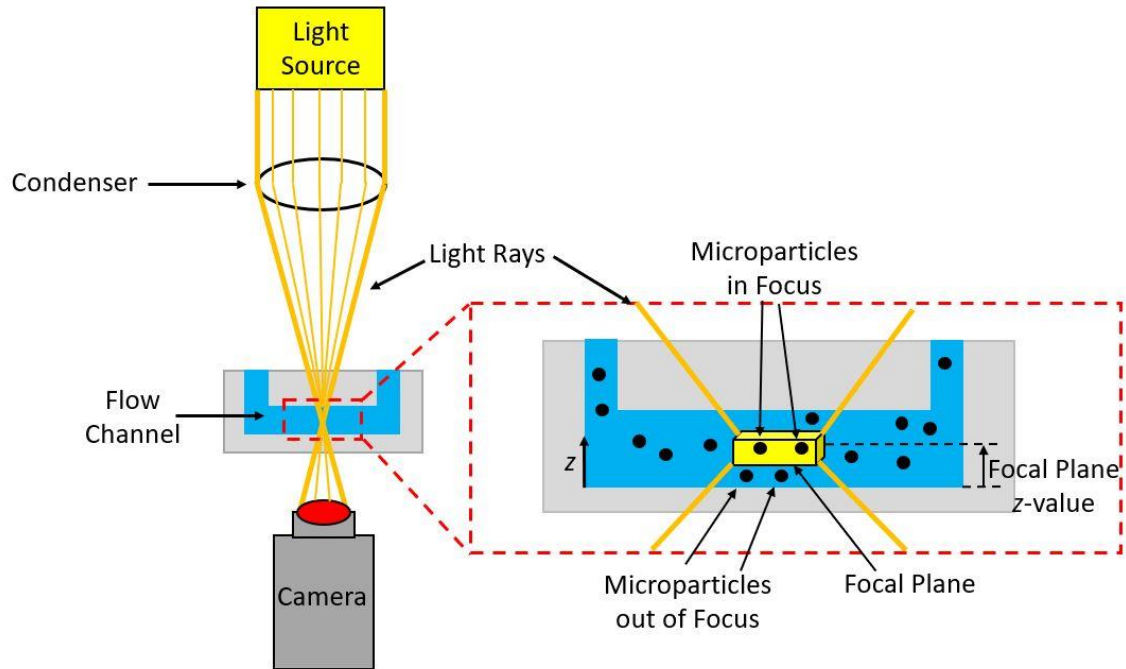


**Figure 5-2:** A schematic diagram of volumetric illumination. Light originating from a light source is focused by a condenser, passes through the sample, and is collected by the camera. A focal plane within the sample is illuminated and in-focus. Particles within the focal plane are able to be tracked during PTV. Imaging occurs at many different focal plane  $z$ -values to quantify the velocity field within the microchannel.

After imaging, image processing was used for data analysis. During image processing, position data for each particle was extracted across the frames of the video, tracer particles were matched between frames, the time information of each frame was added, and velocity was computed using the following equation:

$$\vec{u} = \frac{\overline{\Delta x}}{\Delta t}, \quad (5-1)$$

where  $\vec{v}$  is the computed velocity,  $\overline{\Delta x}$  is the change in position of an individual particle between two consecutive frames, and  $\Delta t$  is the time between frames (1/frames per second). Imaging was conducted at 60 frames per second (fps), therefore  $\Delta t$  was 0.01667 seconds. Averaging of the velocities for all particles within the focal plane determined the flow velocity at the particular channel  $z$ -value. This process was repeated for multiple relevant channel  $z$ -values at the same  $xy$ -location of imaging.

## 5.2 Measuring Channel Height

To accurately measure and predict the velocity profile of the flow within the straight channel microfluidic module which would later become the shear module, its channel height must be known. Knowing the true channel height of the straight channel module allowed for higher quality imaging, a correct measurement of the wall shear stress, and a more accurate comparison of the obtained data to the known analytical model of the velocity profile. As such, the channel height of the straight channel module for applying shear stress as shown in Figure 5-3 was measured using brightfield microscopy as described in Chapter 4.4.2.

To measure the channel height of the straight channel module, the microscope was first calibrated. An inverted brightfield microscope (Olympus IX81) was used with a control software (CellSens Dimension, Olympus) that displayed the  $z$ -location of the objective lens of the microscope relative to the lowest position of the objective. To calibrate the microscope  $z$ -values, the  $z$ -value displayed by the microscope was compared

to a sample with a known height, a gauge sample. The correction factor in air ( $X_{air}$ ) was found to be 1.215 as shown in Figure 4-9.

Once  $X_{air}$  had been found, the height of the straight-channel was measured using brightfield microscopy. The difference in  $z$ -values of the microscope objective when the objective was focused on the top and bottom of the channel was recorded. The difference in  $z$ -values was used with  $X_{air}$  to find the true channel height. The true channel height was found to be 2250  $\mu\text{m}$ .

When conducting PTV, the channel was filled with water. It was found that when the channel was filled with water, the correction factor to convert microscope objective  $z$ -values into true height values was different. The difference between the correction factor when the channel was filled with air ( $X_{air}$ ) and the correction factor when the channel was filled with water ( $X_{water}$ ) may be due to the refractive index difference between air and water. As such,  $X_{water}$  was found through a similar process.

To find  $X_{water}$ , the straight-channel was filled with water and the height of the channel was measured by comparing the  $z$ -value difference when the microscope objective was focused on the top and bottom of the channel. The height measured by the microscope objective when the channel was filled with water was compared to the channel height previously found when it was filled with air. The heights of the channel when it was filled with air and water was used to find  $X_{water}$ , which was found to be 1.626. Once  $X_{water}$  was found, we were then able to determine the channel  $z$ -value imaged during PTV experimentation by looking at the  $z$ -value of the microscope objective.

### 5.3 Particle Selection and Imaging Methods

When deciding what microparticles to use during flow characterization of a microchannel, the size, density, and concentration of the particles must be considered. To obtain high quality results and reduce errors in PTV measurements, proper particle selection is critical. Failure to choose the right particle parameters will result in an increase in error, inability to image particles, or particles that do not trace the flow of interest [84, 85].

When deciding what particle size to use for PTV, the following considerations must be taken. First, particles should be large enough to be seen through microscopy imaging. The ability to distinguish individual particles when they are observed under a microscope is dependent on the magnification of the microscope objective and the resolution of the camera used. Often it is beneficial to calculate the pixel size in the obtained image by imaging a scale. Ideally, the microspheres will be at approximately 2-3 pixels in diameter as microspheres in this size range minimize the amount of error when estimating the particle centroid [86].

Second, particles should be large enough to prevent Brownian motion from impacting the resulting velocity measurements. Brownian motion, or the thermally driven random motion of particles, may introduce error into the PTV measurement. Brownian motion can be quantified based on the Stokes-Einstein diffusion equation, and the error from Brownian motion can be described as shown below [87, 82, 88].

$$\varepsilon = \frac{1}{u} \sqrt{\frac{2D}{t}} = \frac{1}{u} \sqrt{\frac{2}{\Delta t} \frac{k_B T}{3\pi\mu d_p}} \quad , \quad (5-2)$$

where  $\varepsilon$  is the error due to Brownian motion,  $D$  is the Stokes-Einstein diffusion coefficient,  $\Delta t$  is total imaging time,  $k_B$  is the Boltzmann Constant ( $1.381 \times 10^{-23}$  J/K),  $T$  is the temperature in absolute units (293 K),  $\mu$  is the dynamic viscosity of the liquid of which diffusion is occurring ( $10^{-3}$  Pa·s for water), and  $d_p$  is the particle diameter (2  $\mu\text{m}$ ). Through Equation 5-2, it is known that diffusion due to Brownian motion can be limited by decreasing the temperature ( $T$ ) of the setup, increasing the viscosity of the liquid ( $\mu$ ), or increasing particle size ( $d_p$ ). Since temperature and viscosity of the liquid are usually fixed, changing the particle size is typically easiest.

Finally, when deciding on particle size, the particles should be small enough that they trace the flow of interest well. It is recommended that diameter of the particles ( $d_p$ ) used to trace the flow should be at least two orders of magnitude smaller than the characteristic length scale ( $L_{char}$ ) of the flow ( $d_p \ll L_{char}$ ) [82]. The particles density is also an important consideration for determining if the particles will trace the flow. Particles should be neutrally buoyant to negate the effects of gravity on the tracer particles. By ensuring particle density and surrounding fluid density is approximately equal, gravity will not affect the trajectory of the particle.

The concentration of the tracer particles is also highly important when conducting PTV measurements. Ideally, the concentration should be high enough that particles can be easily imaged in a flow, but low enough that the particles outside of the focal plane do not introduce unnecessary noise into the imaging. The signal-to-noise ratio of the output image can be maximized by decreasing the particle concentration, decreasing the thickness of the microchannel, or by decreasing the thickness of the focal plane [89].

In this study, 2  $\mu\text{m}$ -diameter polystyrene microspheres (Phosphorex, Polyspherex Microspheres) were used as tracer particles at a concentration of 0.1%. The particles were imaged under an inverted brightfield microscope (Olympus, IX81) using a high-speed camera (Phantom MIRO M310, Vision Research) at 60 fps under a 40x objective lens with a numerical aperture of 0.60 (Olympus, LUCPlanFLN 40x). Due to the chosen particles and their imaging conditions, it was found that the error due to Brownian motion ranged from 0.16% to 3.30%. Error due to Brownian motion was maximum for particles near the wall and lowest for particles in the center of the channel due to their velocities. Particles attached to the wall did not experience Brownian motion.

The 2  $\mu\text{m}$ -diameter particles imaged under a 40x objective lens in this study had a diameter of 4 pixels and a density of  $1.06 \text{ g/cm}^3$ . The 2  $\mu\text{m}$ -diameter particles were significantly smaller than the 2250  $\mu\text{m}$  height of the channel ( $d_p \ll h$ ), and the density of the particles was close to the density of water ( $0.997 \text{ g/cm}^3$ ). Therefore, the particles used in this study can be assumed to trace the flow of interest while being compatible with PTV image processing algorithms.

The imaging was conducted 27 mm downstream from the inlet at the center of the channel to ensure that entrance and boundary effects would not impact the measurement. To determine the entrance length of the flow, the following equations were used [90].

$$D_H = \frac{4A}{P_{wet}} , \quad (5-3)$$

$$Re_D = \frac{\rho U_{avg} D_H}{\mu} , \quad (5-4)$$

$$L_e = 0.0575 Re_D D_H , \quad (5-5)$$

where  $D_H$  is the hydraulic diameter of the channel,  $A$  is the cross-sectional area of the channel ( $1.125 \times 10^{-5}$  m),  $P_{wet}$  is the wetted perimeter of the channel (0.0145 m),  $Re_D$  is the Reynolds Number based on the diameter of the channel,  $\rho$  is the density of the water ( $997 \text{ kg/m}^3$ ),  $U_{avg}$  is the average velocity through the channel ( $1.48 \times 10^{-4}$  m/s),  $L$  is the channel length (38 mm),  $\mu$  is the viscosity of the water ( $10^{-3}$  Pa s), and  $L_e$  is the entrance length of the channel. The average velocity through the channel ( $U_{avg}$ ) was assumed to be the bulk velocity of the flow and was found by dividing the volume flow rate ( $Q$ ) flowing through the channel by the cross-sectional area ( $A$ ) of the channel (i.e.  $U_{avg} = Q/A$ ) The flow through the microchannel in this study had a  $Re$  of 0.46 and thus an  $L_e$  of 0.38 mm.

The channel  $z$ -values imaged were 19, 115, 210, 306, 402, 605, 808, 1055, 1215, and 1459  $\mu\text{m}$  from the bottom of the channel. During imaging, only the lower half of the channel was imaged due image interference from the patterning of the PDMS in contact with the mold during curing. The PDMS in contact with the mold during curing had a grid pattern. The grid pattern is thought to be due to the grid array of LEDs used in the 3D printer to cure the mold resin. It was assumed the flow velocity would be symmetric across the channel midplane in the  $z$ -direction. An image of the channel and a schematic of the cross-section and focal planes is shown below in Figure 5-3.

For imaging conducted with out high-speed camera (MIRO M310, Phantom Vision Research) with a 40x microscope objective, the depth of field ( $DOF$ ) of the focal plane was 6.52  $\mu\text{m}$ . Because the  $DOF$  was very small compared to the channel height of 2250  $\mu\text{m}$ , the effects of the  $DOF$  were assumed to be negligible. After imaging, an in-house MATLAB code was used to process the data.

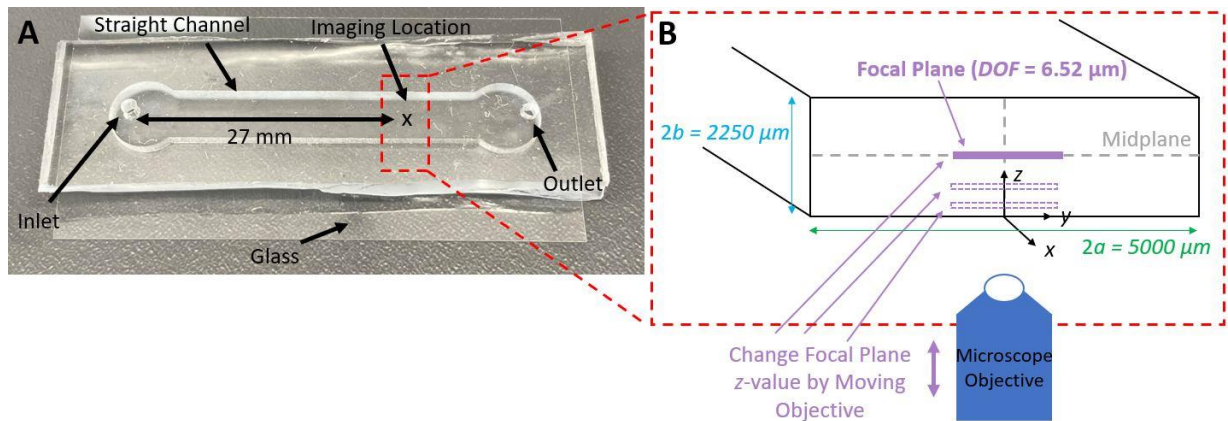


**Figure 5-3:** Image of straight channel microfluidic device. (A) Image of the straight channel device with critical parts labeled. The ‘x’ represents the imaging location for PTV measurements. (B) Channel cross-section schematic describing dimensions and coordinate system. Focal planes during imaging are shown in purple and can be moved by moving the microscope objective up and down.

#### 5.4 MATLAB-Based Image Processing

In this study, images of microspheres obtained from brightfield microscopy were analyzed using an in-house MATLAB code with PTV functions from [91]. The MATLAB code tracked the particles and calculated the velocity of each particle, as shown below in Figure 5-4.

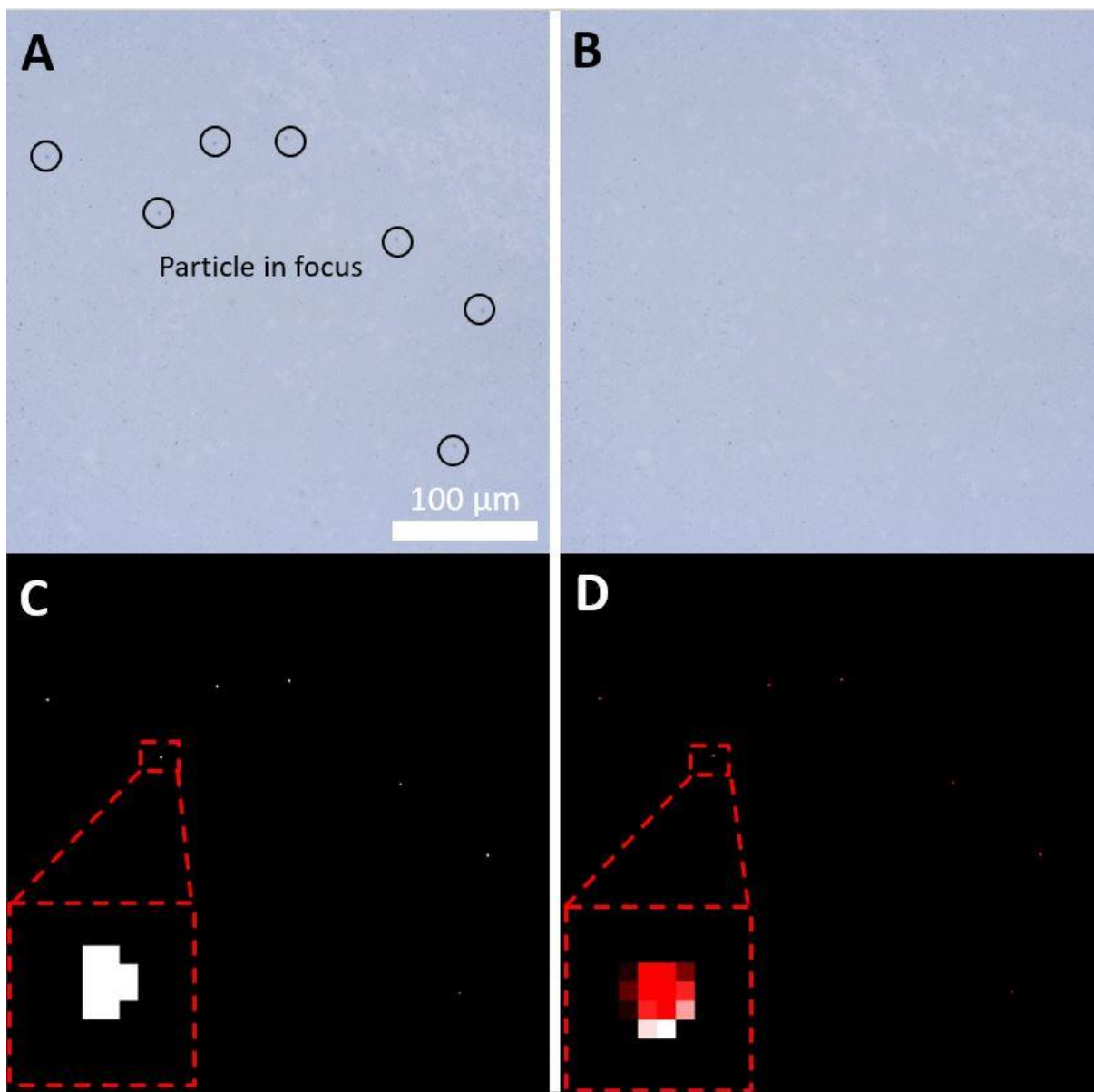


**Figure 5-4:** PTV image processing procedure. (A) Original image at the channel center loaded into MATLAB. In-focus particles are circled and tracked in the following images. (B) The background image generated by averaging 100 frames. (C) The filtered image containing only particles. The image was generated by subtracting the background image (B) from the original image (A) and applying a threshold value to isolate the particles. The image intensity was then flipped so the particles were white. The inset image shows a zoomed-in view of an individual particle. (D) The image of the particles with the

calculated centroids plotted on top. The inset image shows a zoomed-in view of an individual particle with its centroid distribution plotted on top.

First, raw images obtained at a specific channel  $z$ -value were exported as a multipage tiff image through the Phantom Control Software (PCC). The multipage tiff image was then uploaded into MATLAB (Figure 5-4A). The frame rate (60 fps) and scale (0.50275  $\mu\text{m}/\text{pixel}$ ) of the image was also input as shown in lines 9 through 23 of Appendix C.

Second, a background image (Figure 5-4B) was generated through the following as shown in lines 25 through 47 of Appendix C. Each frame was converted into MATLAB's double data type. Through this conversion, each frame of the image was converted into a 3-dimensional matrix where the red, green, and blue (rgb) intensity values are each of the dimensions, respectively. The rgb intensity values from all the frames were then averaged. After averaging, stationary objects in the image had the highest intensity values, whereas moving objects in the image had negligible effect on the average intensity. As such, the rgb intensity averaged image served as the background image. This background image was subtracted from the original image, leaving only the moving objects, and thus particles. The background image was saved as a tiff image.

After subtracting the background image from the original image, the new image contained only the tracer particles. Next, the new image was converted to grayscale and its intensity values were flipped (e.g. black pixels became white pixels) as shown in lines 49 to 66 of Appendix C. Converting the image to grayscale simplified the image, reduced

the computational power required for further image processing, and made the image compatible with the tracking commands used to trace the particles. The intensity values of the image were flipped because the tracking commands used later in the code from [91] required the particles to be lighter than the background.

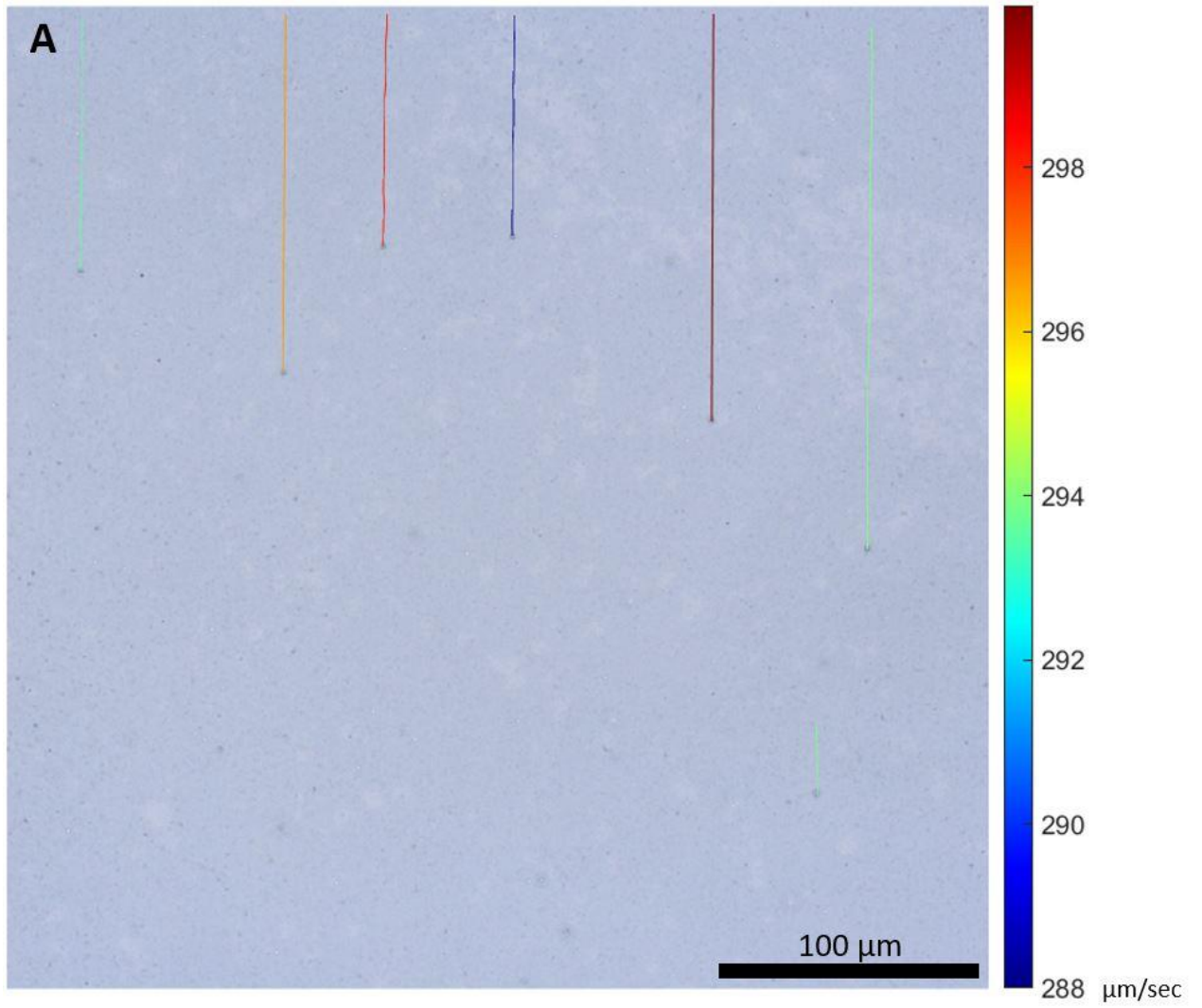
Next, the image was spatially filtered using a bandpass filter algorithm from [91] as shown in lines 75 to 83 of Appendix C. Filtering the image smoothed the intensity values of the particles and made all other pixels in the image black (intensity value of 0). In the remaining image, the particle intensity values followed a gaussian distribution where the center of the particle had the highest intensity value, and the intensity value decreased moving away from the center in any direction. The remaining image was then binarized to a logical array where 0 meant there was not a tracer particle and 1 meant a tracer particle (Figure 5-4C). Binarization removed the Gaussian distribution, further simplifying the image.

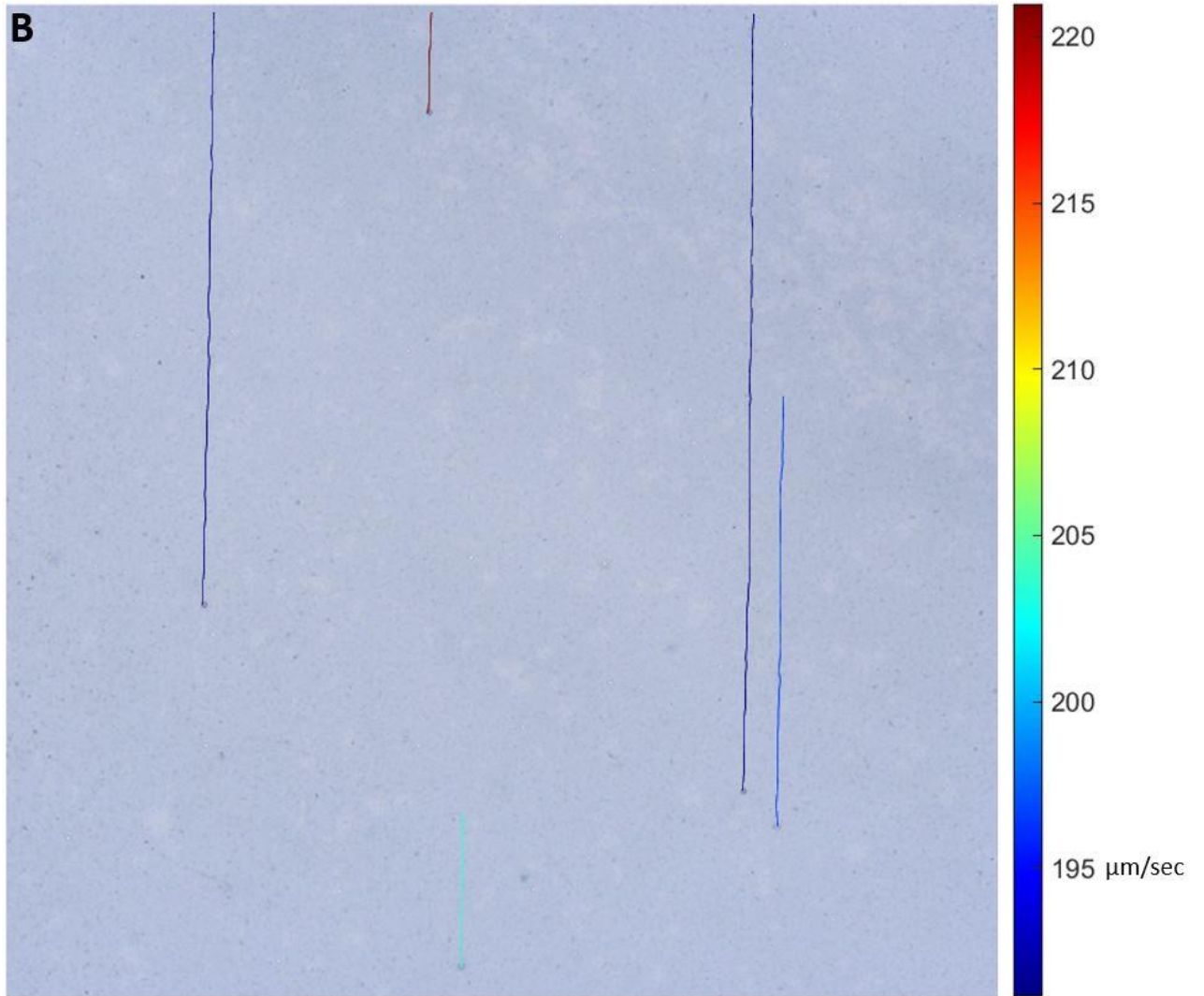
After each frame of the image had been binarized, the image went through two levels of particle center estimation using particle finding algorithms from [91] as shown in lines 85 to 102 of Appendix C. First a pixel-level accurate guess of the particle center was generated by taking a basic average of the pixels with a intensity value of 1 for each particle. Next, a sub-pixel accurate estimation of the particle center was generated by finding the centroid of each particle (Figure 5-4D). For further data analysis, the centroid of the particle was assumed to be the center of the particle.

Once the centroid of each particle in every frame of the image had been identified, the  $x$  and  $y$  coordinates of the centroids were compiled into a matrix. Time values were added to the centroid locations based on what frame of the image each

centroid was from and a particle ID was added to track a particle through multiple frames. Next, the particles were correlated to each other in every frame by estimating the maximum distance the particle would move in a single frame using the tracking command from [91] as shown in lines 104 to 108 of Appendix C.

Once the particle had been tracked and correlated to itself across multiple frames, the velocity of the particle could be calculated using Equation 5-1 by dividing the distance travelled by the particle between two frames by the length of time between each frame as shown in lines 110 to 146 of Appendix C. The particle streamlines were then plotted on top of the original image to visually check the found velocities and trajectories as shown in Figure 5-5.





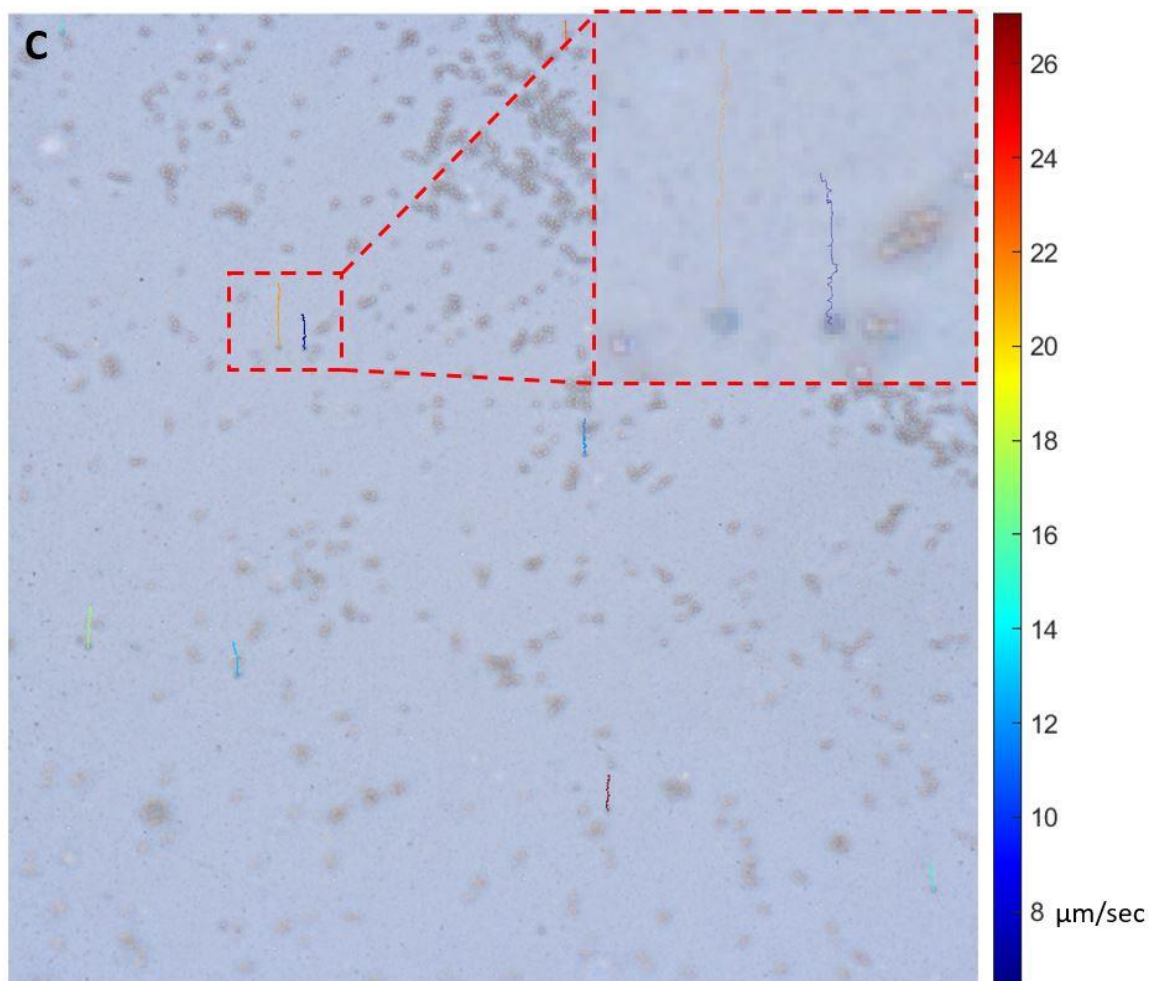


**Figure 5-5:** Results from PTV code. Streamlines are plotted over the original image. Color bars are all shown in  $\mu\text{m}/\text{sec}$ . (A) Streamlines from particles imaged near the center of the channel at a  $z$ -value of  $1050 \mu\text{m}$  with respect to the bottom of the channel. (B) Streamlines from particles imaged at a channel  $z$ -value of  $402 \mu\text{m}$  with respect to the bottom of the channel. (C) Streamlines from particles imaged at a channel  $z$ -value of  $19 \mu\text{m}$  with respect to the bottom of the channel. Inset shows streamlines of two particles zoomed in.

The velocities of all particles was then averaged over all frames of the tiff image. This average velocity value was assumed to be the velocity of the flow at the specific channel  $z$ -value imaged. Imaging and image processing was then repeated at multiple channel  $z$ -values to create a velocity profile of the channel at the specific  $xy$ -location of imaging.

To ensure the code was working properly, the velocities for three particles at an arbitrary channel  $z$ -value were calculated manually using ImageJ and compared to the found results from MATLAB. To measure their speed using ImageJ, the displacement of the particles was identified by looking at the location of the particle in the first frame and the last frame of the image in which the particles appear. Next, the time between the first frame and the last frame was calculated based on the camera frame rate and the number of frames. Finally, the velocity was calculated using Equation 5-1. For the particles analyzed the average velocity for the flow was  $156 \mu\text{m/s}$  using the MATLAB-based PTV code. The velocities, of the same particles, measured manually with ImageJ were  $153.35$ ,  $154.90$ , and  $153.4 \mu\text{m/sec}$ , respectively. When comparing the velocity calculated through MATLAB, there were errors of  $1.70\%$ ,  $0.71\%$ , and  $1.67\%$  from the velocity measured manually with ImageJ, respectively. Because the velocity measured by MATLAB had a maximum error of  $1.70\%$  compared to the velocities measured manually by ImageJ, the MATLAB code was validated and could accurately measure particle velocity.

## 5.5 Results from PTV

In this study, the velocity profile of flow through a straight microchannel microfluidic device with a channel height of  $2250 \mu\text{m}$  and a channel width of  $5 \text{ mm}$  was

measured using PTV. A flowrate of 0.1 mL/min was supplied to the channel using a syringe pump (Fusion 200, Chemyx). Imaging and velocity measurements were conducted at 10 different  $z$ -values of the channel to fully characterize the flow as described in the previous section. The results are described below.

Overall, it was found that the flow within the characterized microchannel followed the expected analytical Poiseuille flow solution for flow through a rectangular channel as shown below [92].

$$u(y, z) = \frac{16a^2}{\mu\pi^3} \left( -\frac{dP}{dx} \right) \sum_{i=1,3,5,\dots}^{\infty} (-1)^{\frac{i-1}{2}} \left[ 1 - \frac{\cosh\left(\frac{i\pi(z-b)}{2a}\right)}{\cosh\left(\frac{i\pi b}{2a}\right)} \right] \frac{\cos\left(\frac{i\pi y}{2a}\right)}{i^3}, \quad (5-6a)$$

$$Q = \frac{4ba^3}{3\mu} \left( -\frac{dP}{dx} \right) \left[ 1 - \frac{192a}{\pi^5 b} \sum_{i=1,3,5,\dots}^{\infty} \frac{\tanh\left(\frac{i\pi b}{2a}\right)}{i^5} \right], \quad (5-6b)$$

where  $u$  was the velocity in the  $x$  direction of the fluid in the channel,  $a$  was half the total channel width (2.5 mm),  $dP/dx$  was the pressure gradient of the flow,  $z$  was the channel  $z$ -value of the imaging location based on the coordinate system in Figure 5-3B,  $b$  was half of the total channel height (1125  $\mu\text{m}$ ),  $y$  was the channel  $y$ -value of the imaging location based on the coordinate system in Figure 5-3B (0 mm), and  $Q$  was the volume flowrate through the channel (0.1 mL/min). Because a volume flowrate ( $Q$ ) was supplied using a syringe pump, Equation 5-6b was used to calculate  $dP/dx$ . Once  $dP/dx$  was calculated, it was plugged into Equation 5-6a to find the expected velocity profile ( $u$ ) for the flow within the rectangular channel.

Comparing the data obtained from PTV with the values calculated using Equation 5-6, as shown in Figure 5-6, it seems that the measured data followed a similar trend to the expected analytical solution. The velocity measurements near the center of the microchannel and the base surface showed little differences to the values calculated using Equation 5-6. The maximum measured velocity of 294  $\mu\text{m}/\text{sec}$  occurred near the center of the channel at a  $z$ -value of 1055  $\mu\text{m}$ , and the minimum measured velocity of 14  $\mu\text{m}/\text{sec}$  occurred near the channel wall at a channel  $z$ -value of 19  $\mu\text{m}$ . When comparing the measured values to the values obtained from Equation 5-6, the largest and smallest velocity differences of 31.86  $\mu\text{m}/\text{sec}$  and 3.22  $\mu\text{m}/\text{sec}$  occurred at channel  $z$ -values of 605  $\mu\text{m}$  and 1215  $\mu\text{m}$ , respectively. Near the channel wall at a  $z$ -value of 19  $\mu\text{m}$ , there was a velocity difference of 3.62  $\mu\text{m}/\text{sec}$ .

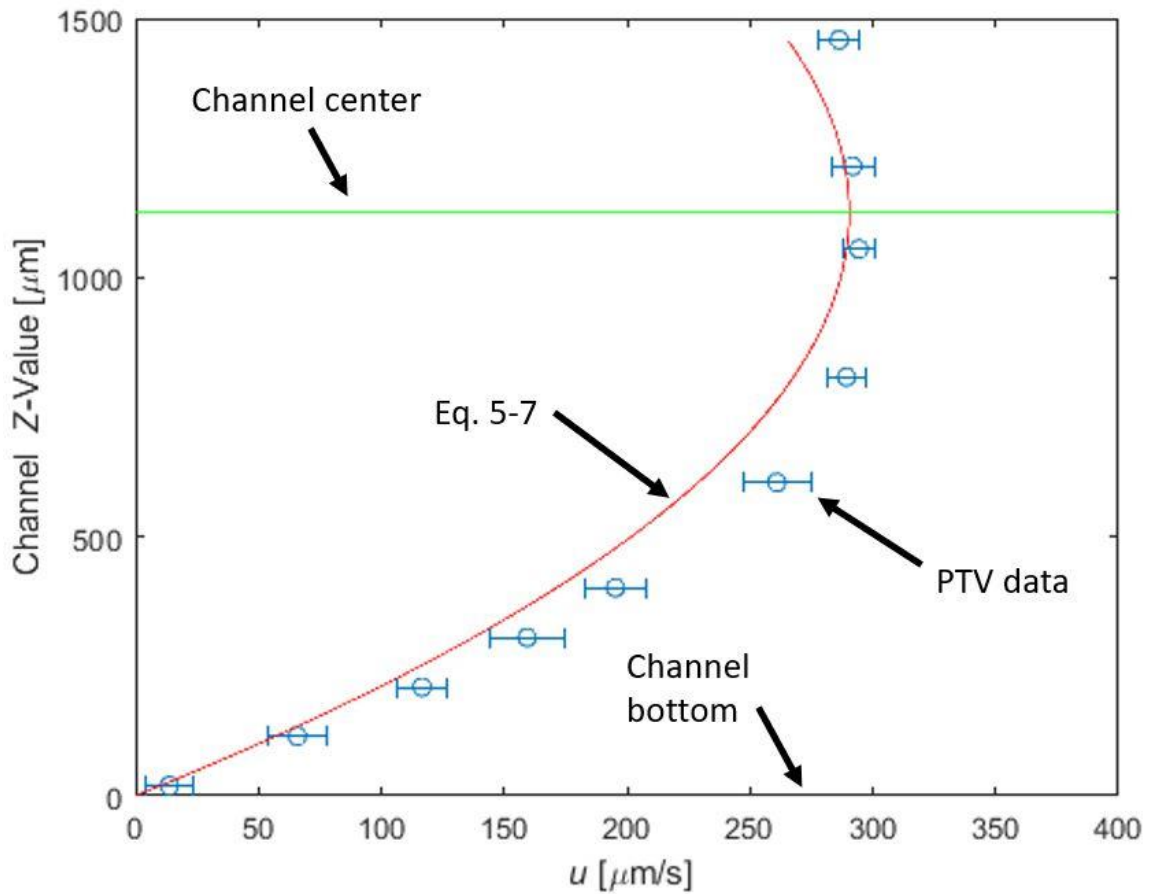


**Figure 5-6:** Comparison of PTV measurement with error bars (blue points) and the analytical solution for Poiseuille flow within a rectangular channel (red line). The channel center (green line) is at 1125 μm.

Once the velocity field of the flow had been measured, the wall shear stress at the imaging location was calculated. To calculate the wall shear stress at the imaging location, the following equation was used.

$$\tau_w = \mu \left. \frac{du}{dz} \right|_{z=0}, \quad (5-7)$$

where  $\tau_w$  is the wall shear stress, and  $du/dz$  is the velocity gradient in the  $z$  direction. From the measured velocity profile, it was found that the wall shear stress value at the imaging location was 0.054  $\mu\text{Pa}$ .

To check the found wall shear stress value, the calculated value was compared to the wall shear stress value found by approximating our channel to two infinite parallel plates. For two infinite parallel plates, the wall shear stress equation is as follows [90].

$$\tau_w = \frac{6\mu U_{avg}}{h} , \quad (5-8)$$

where  $U_{avg}$  is the average velocity of the flow found by dividing the volume flowrate and the cross-sectional area of the channel ( $Q/A$ ) and  $h$  is the channel height. From Equation 5-8 the wall shear stress was approximated to be 0.040  $\mu\text{Pa}$ .

Although the values for wall shear stress found from the measured velocity data and the approximation of infinite parallel plates have a difference of 26.9%, the values are within the same order of magnitude. The approximation of infinite parallel plates assumes that the height between the plates is much less than the width of the plates ( $h \ll 2a$ ) which is not satisfied by the microchannel in this study ( $h = 2250 \mu\text{m}$ ,  $2a = 5000 \mu\text{m}$ ). Therefore, the shear stress calculated using the infinite parallel plate approximation was expected differ from the shear stress calculated using the PTV data. As such, it was assumed that the wall shear stress calculated from the PTV velocity measurements was accurate.

Once the value for wall shear stress had been found and was 26.9% greater than the approximated value using the infinite parallel plate assumption, it was then assumed

that the shear stress applied to the wall of the microchannel could be modulated and predicted by changing the applied volume flowrate and thus the velocity of the flow.

## 5.6 Discussion

Error in the PTV measurements may be attributed to the following causes. First, the depth of field of the focal plane during imaging may have introduced error. When focusing on a specific channel  $z$ -value, particles at channel  $z$ -values slightly greater and slightly lower than the set channel  $z$ -value appeared in-focus due to the thickness of the focal plane. Particles at channel  $z$ -values slightly greater and lower than the set channel  $z$ -value will have different velocities than particles at the set channel  $z$ -value, leading to error in the velocity measurements. During brightfield microscopy imaging, the depth of field, or the thickness of the focal plane, is finite as described in Chapter 4.4.6 in Equation 4-4 [77, 78].

Therefore, when imaging particles, the focal plane had a thickness of approximately 6.52  $\mu\text{m}$ . Because the focal plane was thicker than the particles being imaged (2  $\mu\text{m}$ -diameter), particles at different channel  $z$ -values were included in the velocity measurement, which introduced error.

The effects of Brownian motion may have contributed to the error in the velocity measurements as well. As discussed previously, the error due to Brownian motion can be described by Equation 5-2. The error due to Brownian motion ranged between 0.16% and 3.30%, with the error from Brownian motion increasing close to the bottom of the

channel. Because the error due to Brownian motion was relatively small, the effects of Brownian motion were assumed to be negligible.

Error may have been introduced into the measurement through the image conversion when performing image processing. When converting the image into a binary image that contains only the particles, a threshold value was used to determine what areas were identified as particles. A constant threshold value of 5 was chosen as it appeared to consistently identify in-focus particles. Although particles were able to be identified, some particles which were identified initially were not identified in later frames of the video as shown in Figure 5-5A. Loss of identification of some particles may be due to slight misalignment between the microchannel and the focal plane. If the microchannel and the focal plane were slightly out of alignment particles may not have streamlines parallel to the focal plane, and as such exit the focal plane when flowing through the channel. Slight misalignment of the focal plane and the microchannel may introduce error due to the particles imaged residing along multiple streamlines and thus slightly different velocities.

Overall, despite these sources of error, the velocity measurements were shown to follow a similar trend as the expected values from Equation 5-6. The velocities also had little difference near the center of the channel and the bottom of the channel. Due to their agreement, the velocity measurement method using PTV was thus assumed to be accurate and represent the flow. Therefore, particle tracking velocimetry could be used to accurately measure the velocity profile of flow through our microchannel.

With the characterization of the flow through the straight channel microfluidic, it was then possible to predict the level of shear stress on the wall of the microchannel with

varying applied volume flow rates. Quick changes of applied shear stress to fit the required need are also possible by changing the volume flow rate, channel height, or working fluid.

## **Chapter 6: Applications of the Microfluidic Motherboard and Its Modules**

In this study, a microfluidic motherboard and multiple modules have been developed and characterized for use with each other to overcome some of the limitations of microfluidic lab-on-a-chip devices. In this chapter, the uses for which this device was developed will be discussed and future applications will also be suggested. The different microfluidic components characterized and ready for use are the motherboard, the balloon module, and a straight-channel module.

The combination of the motherboard and modules discussed was designed to serve as an active microfluidic mixer. The microfluidic motherboard developed serves as a standardized base for which any microfluidic module can be connected as long as the ports of the microfluidic module are compatible with the motherboard. Additionally, the motherboard can be easily reconfigured using computer aided design (CAD) software to fit the needs of the end-user. Because of its high level of modularity and ease of design change, the motherboard can be used for any microfluidic configuration the end-user may need.

The scenario for use of the active microfluidic mixer involves a hypothetical mechanobiological study using the microfluidic components developed in this study. The motherboard will serve as the platform for which the different microfluidic modules can interact. The first module consists of the balloon module, serving as an active microfluidic mixer. In the second module, cells would be cultured, and the sample mixed in the first module would apply shear stress to cells in the second module. In this scenario, the mechanobiological response of cells in the second module to shear stress

could be investigated while tightly controlling the cell culture media surrounding them as shown in Figure 6-1.

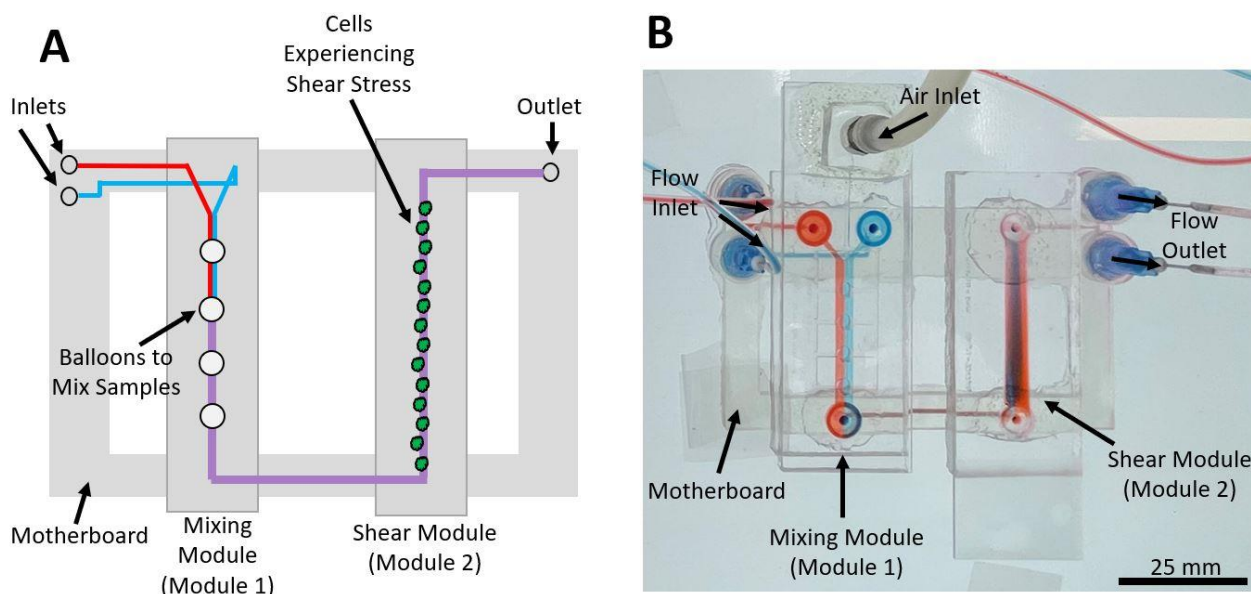


**Figure 6-1:** Hypothetical mechanobiology study overview. (A) Schematic of the experiment where two samples are mixed in the first module before applying shear stress to cells in the second module. The main components are the motherboard, mixing module, and straight-channel module. (B) Image of the microfluidic components for the hypothetical experiment.

### 6.1 Motherboard and Module Operation

To operate the device, both pressurization of the balloon part and flow through the mixing channel part of the device must be accomplished. To achieve dynamic inflation, the setup shown in Figure 6-2 was used. After connecting the modules to the

motherboard, a diaphragm pump (SP 500 EC-LC 4.5Vdc, Schwarzer) was connected to the connection port of the balloon part using silicone tubing. A voltage of 4V was supplied to the pump via a DC power source (HY3005D, Mastech) so that the balloons could reach near maximum pressurization achievable by the pump without risking damage to the pump.

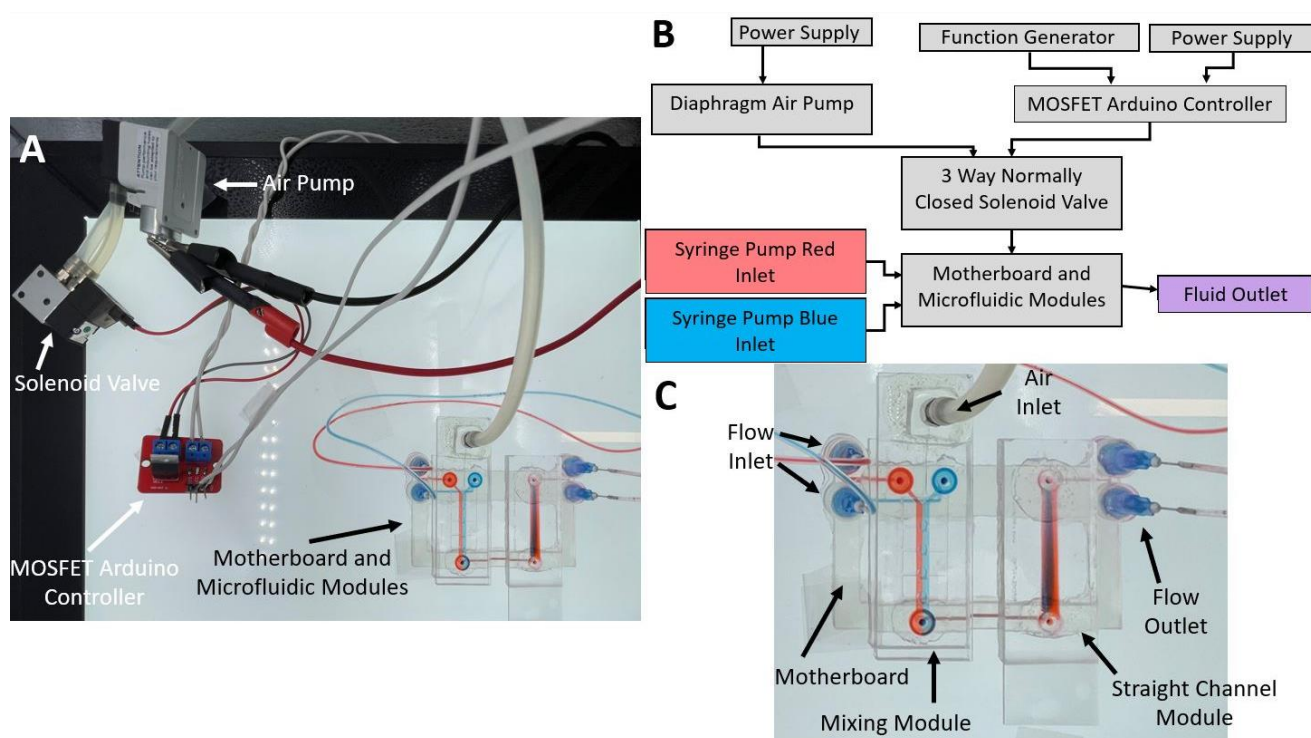


**Figure 6-2:** Experimental setup of mixing experiment with dynamic balloon inflation.

(A) An image of experimental setup. The balloons of the device are controlled via a solenoid valve, a MOSFET Arduino controller, and a diaphragm air pump. (B) A block diagram of the experimental setup used to facilitate the mixing module on the motherboard. (C) Close-up of the microfluidic motherboard and modules. The microfluidic mixing module is connected to the motherboard. The mixing module has

two inlets, one for red dye water and one for blue dye water. After the liquids mixed in the mixing module, they then flow through the straight channel module.

The pump was connected to a 3 way normally closed solenoid valve (S10mm-30-12-4a, Pneumadyne Inc.) via silicone tubing. The solenoid valve was connected to a function generator (SDG1025, Siglent) and a 12 V Arduino (MOSFET Arduino, HiLetGo). A square wave with a high amplitude of 10V and a low amplitude of 0V was supplied to the solenoid valve via the MOSFET Arduino controller. When the solenoid was powered, air from the pump could flow into the device until the maximum pressure supplied by the pump was reached. When the solenoid valve was not powered, air would flow out of the device until the pressure inside the balloon part of the device was in equilibrium with the ambient pressure. To control the solenoid valve, a function generator and MOSFET Arduino controller was used. A square wave with a high level of 10V and a low level of 0V was supplied to the MOSFET Arduino controller by the function generator. The signal was amplified by the MOSFET Arduino controller and fed into the solenoid. The MOSEFT Arduino controller was supplied 12V via a power supply (DC Power Supply 40532, Hiltex).

After the balloon pressurization system had been connected, the flow portion of device operation was set up (Figure 6-2C). To set up the device for flow, the inlet and outlet needles of the motherboard were inserted into tubing (Tygon Tubing AAD02103-CP, Cole-Parmer) connected to two separate syringes each within a syringe pump (Fusion 200, Chemyx Inc.). Each syringe was operated by a different syringe pump to ensure the generated flowrate was consistent. For the mixing experiment, one of the syringes

contained red dye (McCormick Culinary) water, and the other syringe contained blue dye water. A flowrate of 0.1 mL/min was generated for each color, for a combined flowrate of 0.2 mL/min. The frequency at which the balloons of the device are actuated during a mixing experiment is known as the mixing frequency. Mixing frequencies of 0 Hz, 1 Hz, 5 Hz, 10 Hz, and 15 Hz were tested in this study.

A time series of balloon inflation is shown below in Figure 6-3 for a balloon inflating at a mixing frequency of 1 Hz. In the below figure, the balloons of the device are initially deflated. Over the course of 0.066 seconds the balloons inflate, displacing the fluid above them. Then, over the next 0.066 seconds, the balloons deflate. The repeated process of balloon inflation and deflation mixes the fluids flowing above them. A single balloon inflation cycle took a total of 0.132 seconds. The experiment setup described in this section was used to perform a mixing experiment.

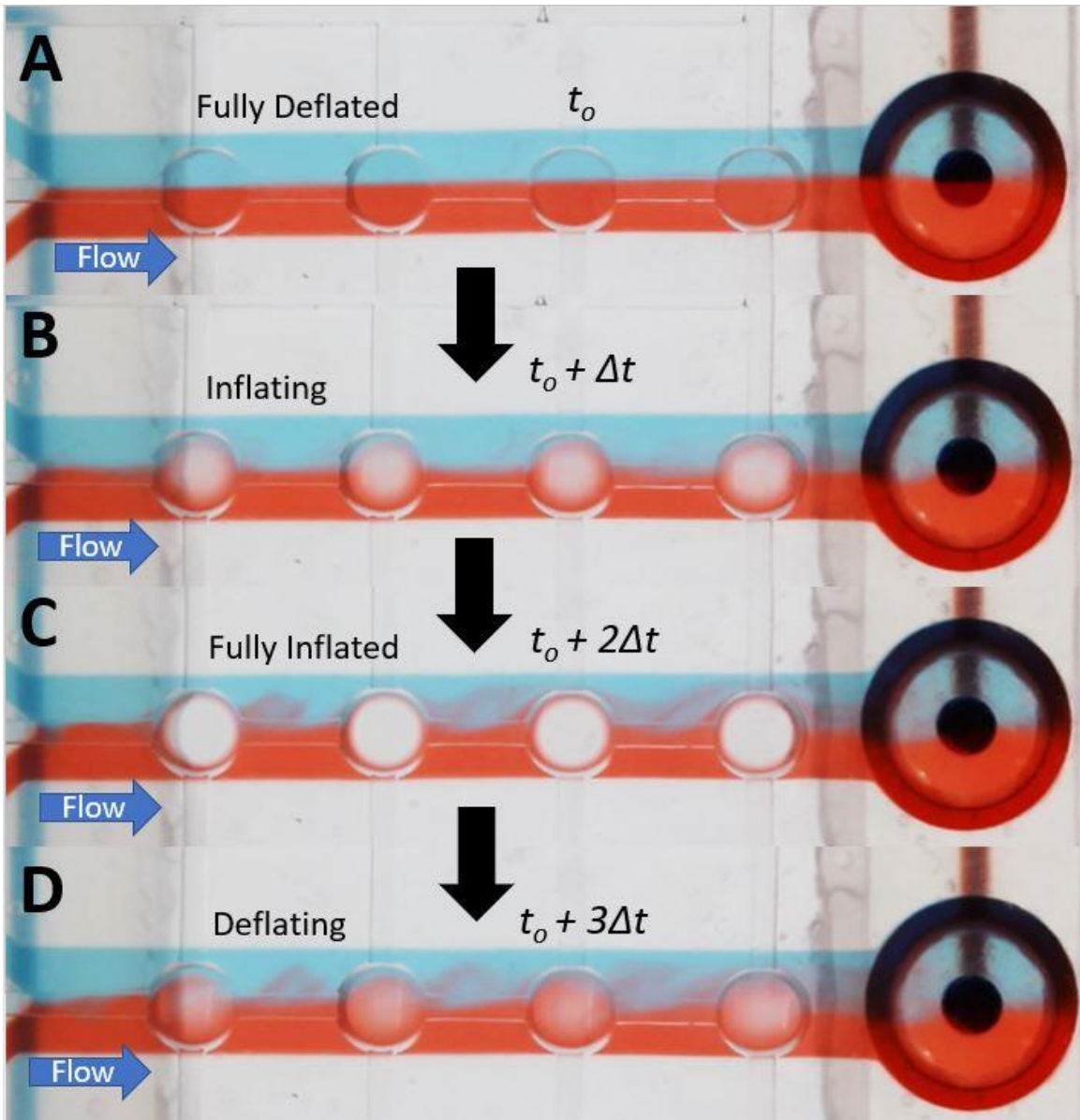


**Figure 6-3:** A time series of a balloon inflation cycle ( $\Delta t = 0.033$  sec) at a mixing frequency of 1 Hz. In all images the dye water is flowing left to right. (A) Initial time when balloons are deflated. (B) Image showing when balloons are inflating. (C) Image showing when balloons are fully inflated. Displacement of the red dye and blue dye are observed. Vortices are generated and show a similar pattern to Kármán vortices. (D) Image showing balloons as they are deflating.

## 6.2 Active Microfluidic Mixing

Mixing in microfluidics is well known to be limited due to the dominance of viscous effects in microchannels as described in Chapter 1.4. The small  $Pe$  found in microchannel flows indicates a long mixing timescale. Given the small microchannels, the timescale of the flow is small. Therefore, efficient mixing due to the flow does not happen within microchannels.

Due to limited mixing in microchannels, the microfluidic balloon module, consisting of a balloon layer and a flow layer, was designed to be an active microfluidic mixer. Through the previously described procedure, the active microfluidic mixer could be fabricated reliably and repeatedly using 3D printed molds and soft lithography as shown in Figure 6-2C.

The fabricated balloon layer had easily controlled, highly consistent balloon diameters. Also, the thickness of the balloons was easily controlled by varying the speed when spin-coating PDMS. Due to the tight control on balloon diameter and thickness, the balloons had easily predictable and highly consistent inflation heights. Dynamic inflation of the balloons could be achieved using the setup in Figure 6-2A.

To test the effectiveness of active mixing using the balloon module, the following experimental procedure was implemented. First, the motherboard and the modules were setup to performing the mixing experiment as shown in Figure 6-2C. The balloon module was connected to the first slot of the motherboard, and the straight-channel module was connected to the second slot of the motherboard. The balloon module for mixing had four balloons each with a diameter of 2.5 mm. Both the flow channel above the balloons and

the flow channel that served as the second module connected to the motherboard had a channel height of  $840\ \mu\text{m}$  and a width of  $3.5\ \text{mm}$ .

Next, the inlets to the motherboard were connected to two syringes, one with red dye water and one with blue dye water. The balloon layer of the balloon module for mixing was connected to the diaphragm pump controlled by a solenoid valve and function generator.

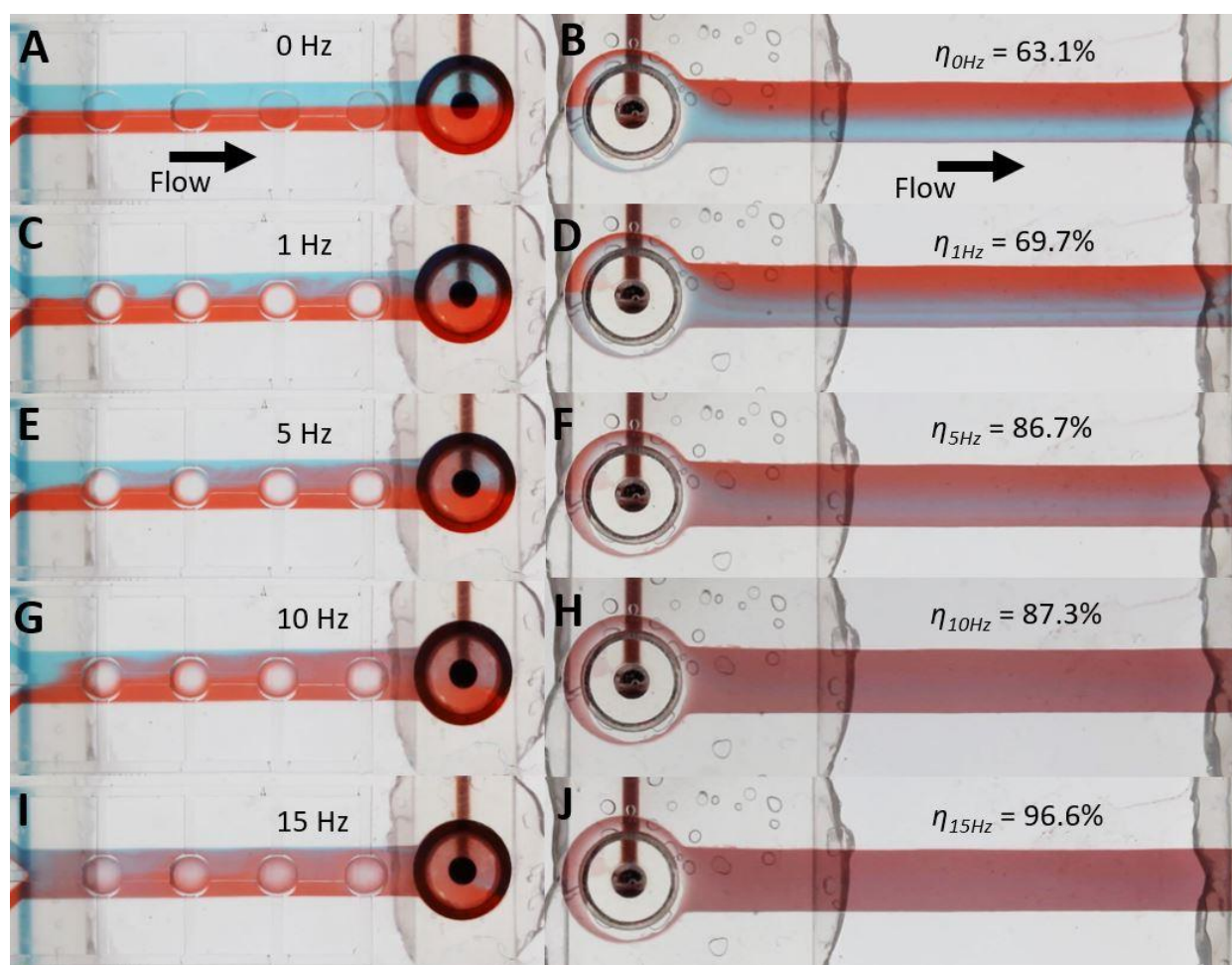


**Figure 6-4:** Balloon module for mixing and straight-channel module connected to motherboard for mixing experiment. A flowrate of  $0.2\ \text{mL}/\text{min}$  was supplied to both

modules. When the balloons were inflated at 0, 1, 5, 10, and 15 Hz, the mixing in the second channel had an efficiency of 63.1%, 69.7%, 86.7%, 87.3%, and 96.6%, respectively. (A, B) Modules with 0 Hz balloon inflation. (C, D) Modules with 1 Hz balloon inflation. (E, F) Modules with 5 Hz balloon inflation. (G, H) Modules with 10 Hz balloon inflation. (I, J) Modules with 15 Hz balloon inflation.

Once the motherboard and modules had been assembled, flow was generated through the motherboard and modules by the syringe pumps as shown in Figure 6-2. The syringe pumps each flowed in red dye water and blue dye water at a rate of 0.1 mL/min for a combined flowrate of 0.2 mL/min through each module. The balloons were modulated using a solenoid valve and a function generator. The balloons were actuated with a pump voltage of 4.0V (70 kPa) and at frequencies of 0, 1, 5, 10, and 15 Hz. To measure the mixing through the modules, both modules were imaged using a DSLR camera (EOS Rebel T3, Cannon) and a 100 mm macro lens (Macro Lens EF 100mm, Cannon) with a frame rate of 60 frames per second (fps).

Once the flow through the mixing module and shear module had been imaged (Figure 6-4), it was qualitatively seen that as the mixing frequency increased, the mixing generally increased as well. To quantify our results, an image-processing MATLAB code was used to quantify the mixing efficiency through each channel. Images taken when the balloon was at maximum inflation were analyzed using MATLAB.

The MATLAB code used to analyze the images obtained during the mixing experiment (Appendix D) began by reading in the image data and is shown in Figure 6-5.

Next, the image was rotated such that the channel was vertical in the image for consistency (Figure 6-5A). The image was then cropped so that only the channel remained in the image (Figure 6-5B) (Appendix D lines 1 to 40). For the balloon module, the mixing was analyzed after each balloon. For the straight channel module, the mixing through the whole channel was analyzed. Negligible mixing efficiency change was found when comparing different regions of the straight-channel in the direction of flow.

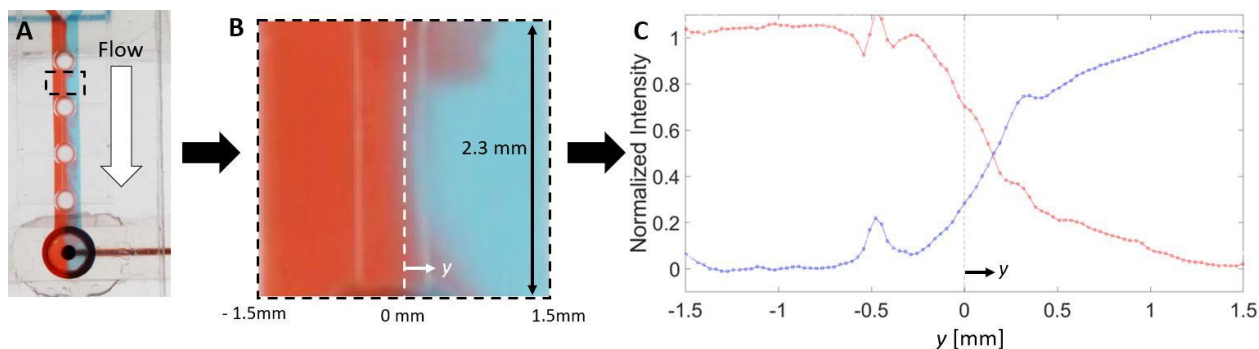


**Figure 6-5:** MATLAB image processing for mixing images. Process shows analysis of mixing after balloon 1, as shown by dashed box, at 1 Hz. (A) Original image rotated so that the channel was vertical. (B) Section of interest after balloon 1. (C) Average red and blue intensity values across the channel width after normalization.

Next, the red and blue pixel intensity values of the cropped image were averaged for each location along the channel width. Red dye water had high red pixel intensity values, while blue dye water had high blue pixel intensity values. Only the inner 3 mm of the channel, shown in Figure 6-5B, were analyzed due to error near the edge of the channel caused by reflection and the channel height decreasing near the edge. The

channel height is thought to decrease near the edge of the channel due to the graduate reduction of red or blue pixels at each respective edge of the channel. Due to UV light scatter when 3D printing the mold for the straight-channel, the edge of the channel may not be perfectly vertical and thus the height decreased near the edge of the channel.

The averaged intensity values for red and blue were normalized (Appendix D lines 42 to 76). The normalization factor was determined by finding the maximum red or blue value of the channel before mixing had occurred as shown below.

$$I_{normalized} = \frac{I_i - I_{min}}{I_{max} - I_{min}} , \quad (6-1)$$

where  $I_{normalized}$  is the normalized pixel intensity,  $I_i$  is the intensity of the  $i^{th}$  pixel,  $I_{min}$  is the minimum pixel intensity, and  $I_{max}$  is the maximum pixel intensity. Finally, the normalized red and blue intensity values were plotted with respect to the channel width (Appendix D lines 78 to 144).

The mixing within the microchannel was investigated after each balloon of the mixing device. The resultant mixing in the straight channel was also analyzed using the same procedure. To quantify the quality of the mixing, the mixing efficiency was calculated by imaging the second channel and using the following equation [93].

$$\eta = \left[ 1 - \frac{\sqrt{\frac{1}{N} \sum_{i=1}^N (I_i - I_\infty)^2}}{\sqrt{\frac{1}{N} \sum_{i=1}^N (I_o - I_\infty)^2}} \right] \times 100\% , \quad (6-2)$$

where  $\eta$  is the mixing efficiency,  $N$  is the number of pixels across the width of the channel,  $i$  is the  $i^{th}$  pixel of the channel width,  $I_\infty$  is the normalized intensity at complete mixing (0.3113), and  $I_o$  is the normalized intensity at no mixing (1). When calculating

mixing efficiency, a  $\eta$  value of 100% indicates complete mixing in the channel, and a  $\eta$  value of 0% indicates no mixing occurred within the channel.

For quantifying mixing efficiency, the red pixel intensity values were used because red pixel intensity values were visually dominant, therefore it was easier to qualitatively check the calculated efficiencies with the obtained images. Additionally, the normalized intensity at complete mixing ( $I_\infty$ ) was assumed to be the average red pixel intensity value within the second channel after the first channel mixed the dye at 15 Hz. The normalized intensity at complete mixing was found by averaging all pixels of the shear module after the dyes were mixed at a mixing frequency of 15 Hz. The effect of balloon inflation frequency on mixing was also investigated by analyzing the mixing in both channels at 0, 1, 5, 10 and 15 Hz. The results are summarized below.

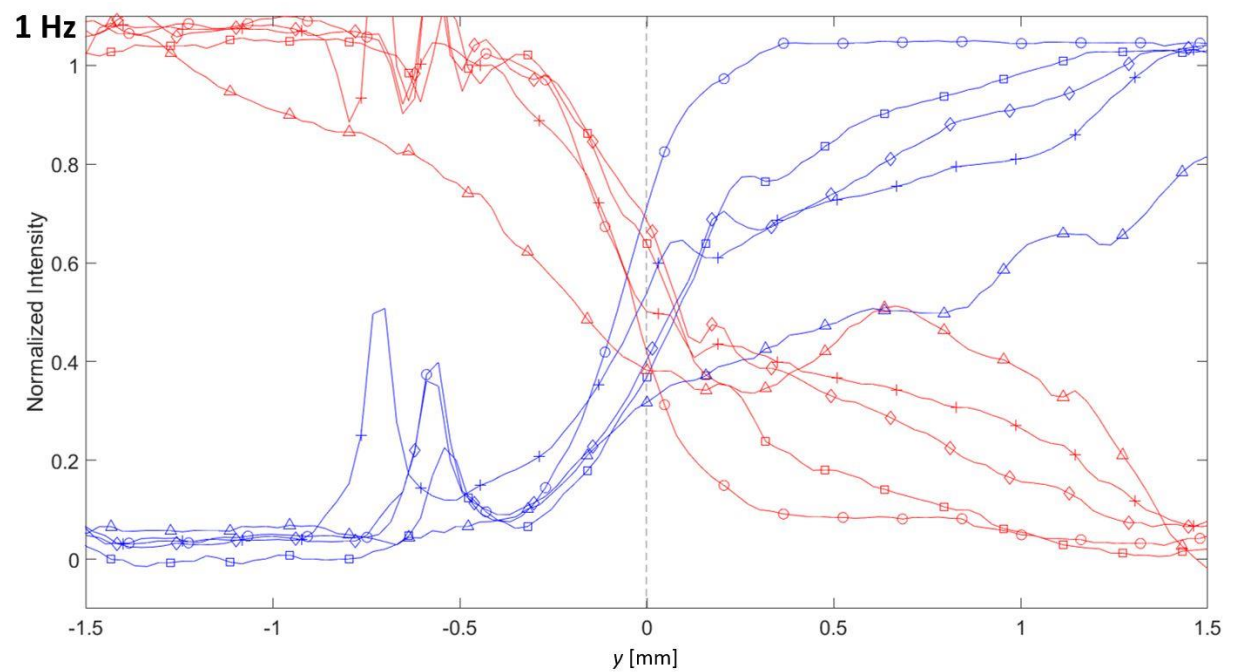
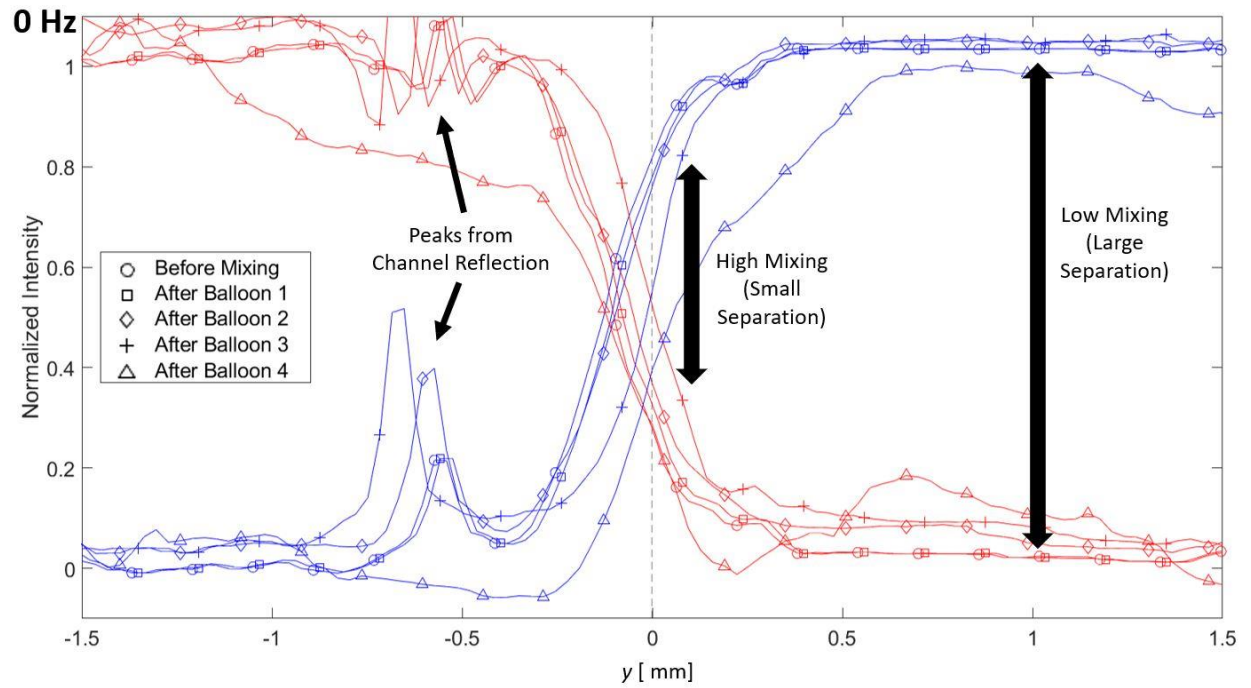
## 6.3 Results

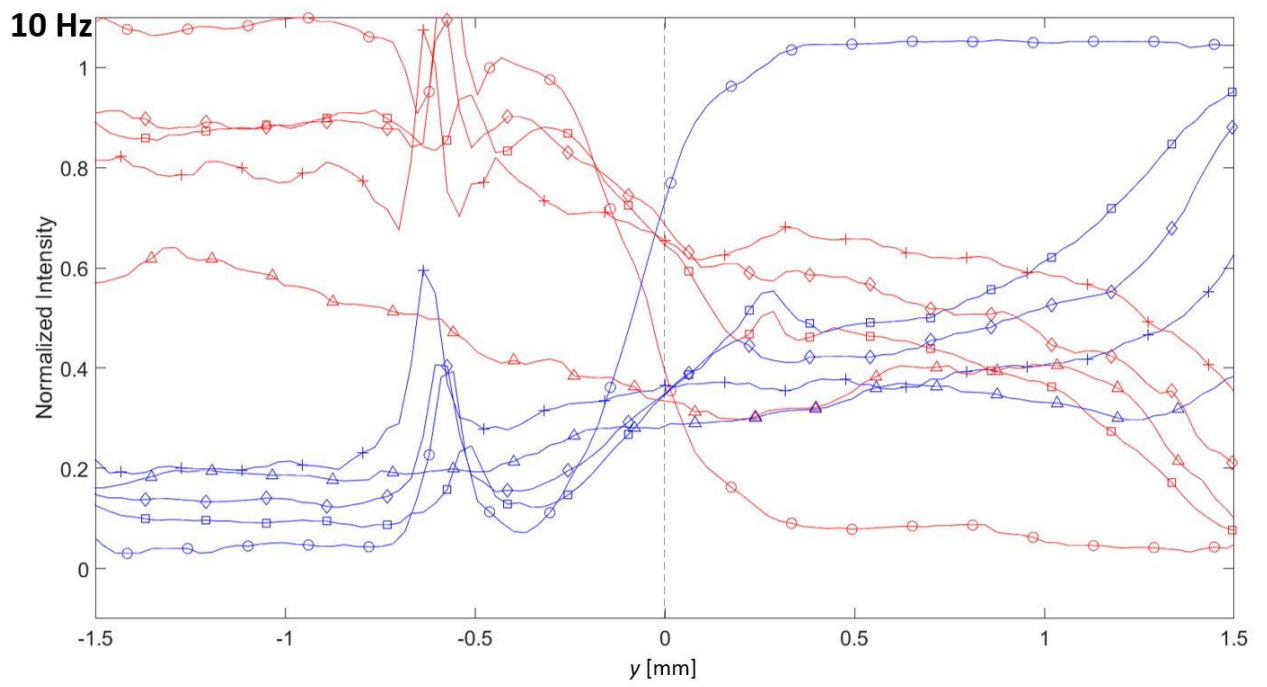
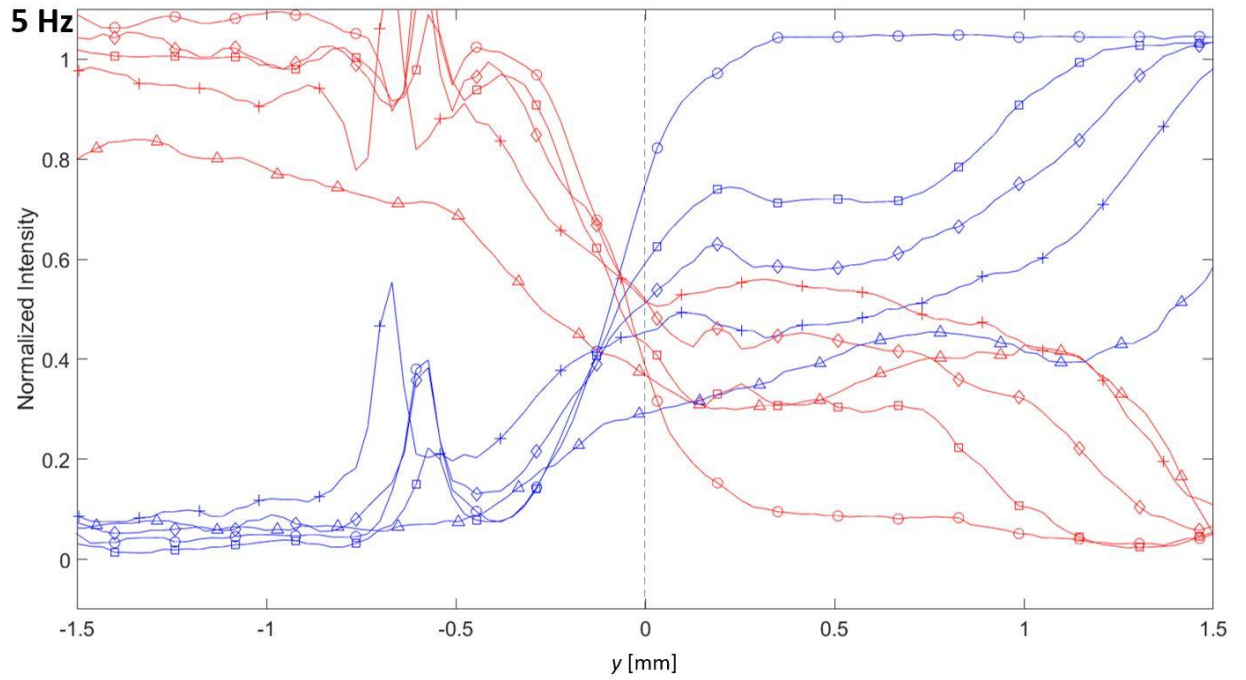
### 6.3.1 Mixing in the Microfluidic Mixer

In this study, the mixing within a microchannel due to our active mixer was investigated through imaging and image processing. A balloon module with 4 balloons (diameters: 2.5 mm), and a flow channel (height: 840  $\mu\text{m}$ , width: 3.5 mm) was used in combination with a second straight-channel module and a motherboard. Mixing was analyzed after each of the four balloons, as well as within the straight channel module.

Overall, it was found that as the red and blue dye water flowed over the dynamically actuating balloons of the active mixer, the samples were mixed as shown in Figure 6-6. The performance of the mixer can be determined by comparing the red and

blue values across the channel width. Separation between the two colors indicated little mixing, and convergence between the colors indicated mixing (Figure 6-6).





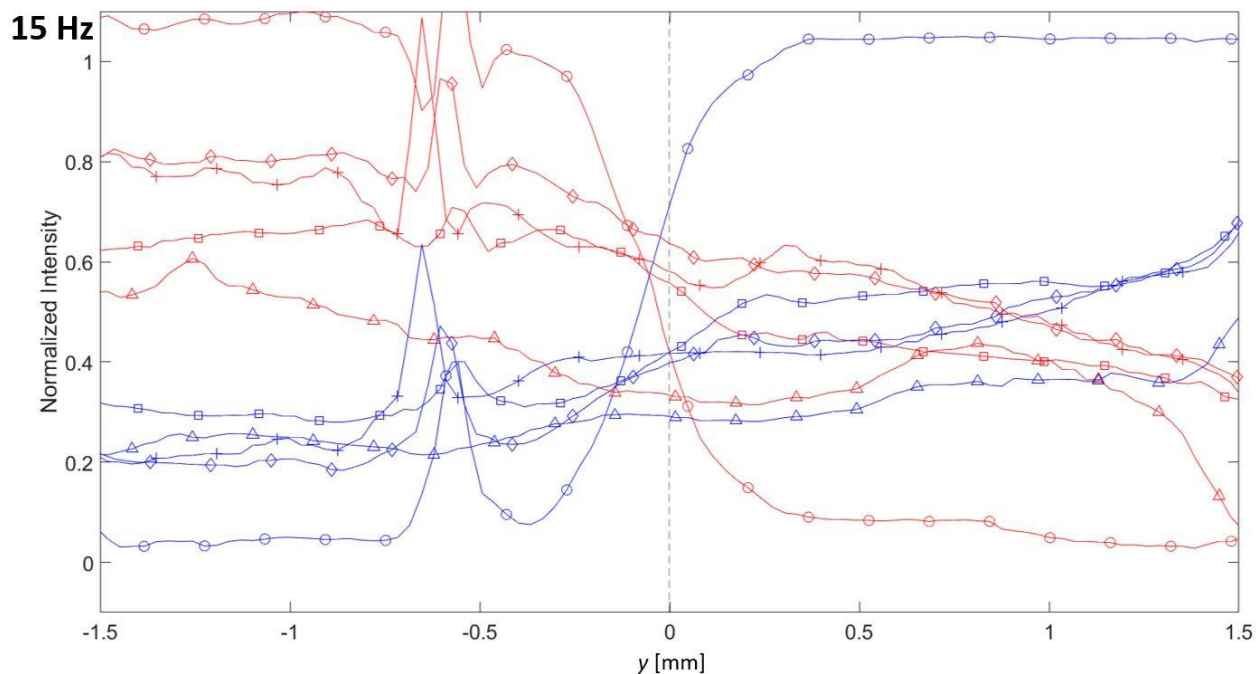


**Figure 6-6:** Quantitative mixing analysis of mixing within the active mixing microfluidic. The red lines represent the normalized red pixel intensity values, and the blue lines represent the normalized blue pixel intensity values. The circles, squares, diamonds, “+”, and triangles represent mixing before the balloons were actuated, after balloon 1, after balloon 2, after balloon 3, and after balloon 4, respectively. Balloon actuation frequencies were 0, 1, 5, 10, and 15 Hz, respectively.

From Figure 6-6, for all frequencies the mixing of the red and blue dye increased after each balloon of the microfluidic mixer. Additionally, as the frequency of mixing was increased, the dyes mixed more quickly. The dyes also appear to have more complete mixing in the right side (blue side) of the device. The difference of mixing across the width of the channel may be due to misalignment between the flow channel and the balloons of the mixer as shown in Figure 6-7.

Misalignment between the balloons and the flow channel may cause one side of the flow channel to have more volume displaced than the other, leading to uneven mixing. Even though mixing may not be symmetric over the centerline of the channel, the dyes have further opportunity to mix through the microfluidic motherboard before reaching the second channel. From Figure 6-7, it was found that the balloon-center-to-center line and the interface between the two dyes had a difference of  $1.24^\circ$ . Because the difference between the balloon-center-to-center axis and the interface between the two dyes was relatively small, the effect of misalignment on the performance of the mixing module was assumed to be negligible.

In Figure 6-6, one can also see that there are sharp peaks (shown by arrows in 0 Hz case) in the concentration of red and blue dye near the channel width of -0.6 mm for all frequencies. These peaks are thought to be due to reflections from the channels within the balloon layer as shown below in Figure 6-7. The imaged channel reflections appear to be white and as such have a much higher red and blue pixel intensity than the other regions of the channel near -0.6 mm.

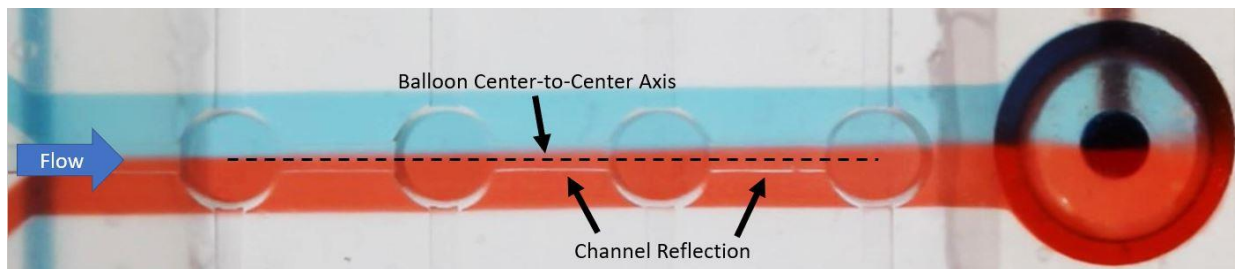


**Figure 6-7:** Image of mixing channel before mixing to show  $1.24^\circ$  difference between the balloon center-to-center axis and the interface of the red and blue dye. The dotted line

the balloons center-to-center axis. The interface of the red and blue dye water deviates from the balloon center-to-center axis downstream of the channel. Channel reflections are from the balloon microchannels are shown and may have caused peaks in Figure 6-6.

Although the red and blue dye is not completely mixed after passing over the final balloon of the balloon module, the dye has a chance to mix when passing through the motherboard before entering the second module. Mixing of the dyes after leaving the first module, but before entering the second module may be due to the twisting of the channels of the motherboard connecting the two modules. As such, the final mixing efficiency of the two dyes was characterized by imaging the second channel on the motherboard.

### **6.3.2 Mixing Efficiency Measured in the Second Module**

The first module of the motherboard, the balloon module, was designed to mix two samples before the mixture passes through the second module of the motherboard. As such, the final result of the mixing is most important within the second module of the motherboard. To understand the mixing efficiency of the dyes passing through the second module, the flow through the second module was imaged and image processing was used to quantify the mixing efficiency as described by Equation 6-2.

Overall, it was found that as balloon actuation frequency increased, the mixing efficiency in the second channel increased as shown below in Figure 6-8. The mixing efficiency was quantified in the region of the second channel that was above the viewing window of the motherboard. The quality of mixing can be seen by comparing the

difference of red and blue pixel intensity values at any channel width. From Figure 6-8, the highest quality mixing occurred at a mixing frequency of 15 Hz, and the lowest quality mixing occurred at a mixing frequency of 0 Hz.

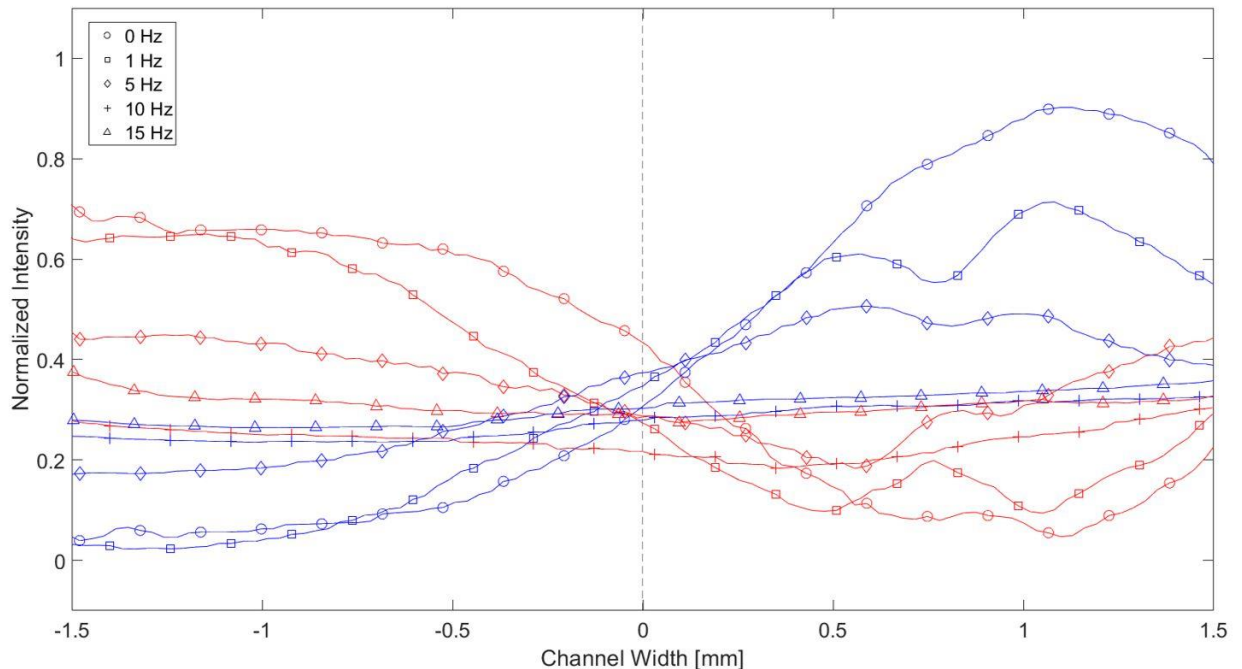


**Figure 6-8:** Quantitative mixing analysis of mixing within the second module. The red lines show the red pixel intensity across the width of the channel, and the blue lines show the blue pixel intensity across the width of the channel. Circles, squares, diamonds, “+”, and triangles represent mixing frequencies of 0, 1, 5, 10, and 15 Hz, respectively.

To further quantify the effect of mixing, the mixing efficiency was calculated for the second module using Equation 6-2. The relation between mixing efficiency in the second channel and the mixing frequency in the first channel can be seen below in Figure

6-9. Mixing efficiencies for balloon actuation frequencies of 0, 1, 5, 10, and 15 Hz were 63.1%, 69.7%, 86.7%, 87.3%, and 96.6%, respectively.

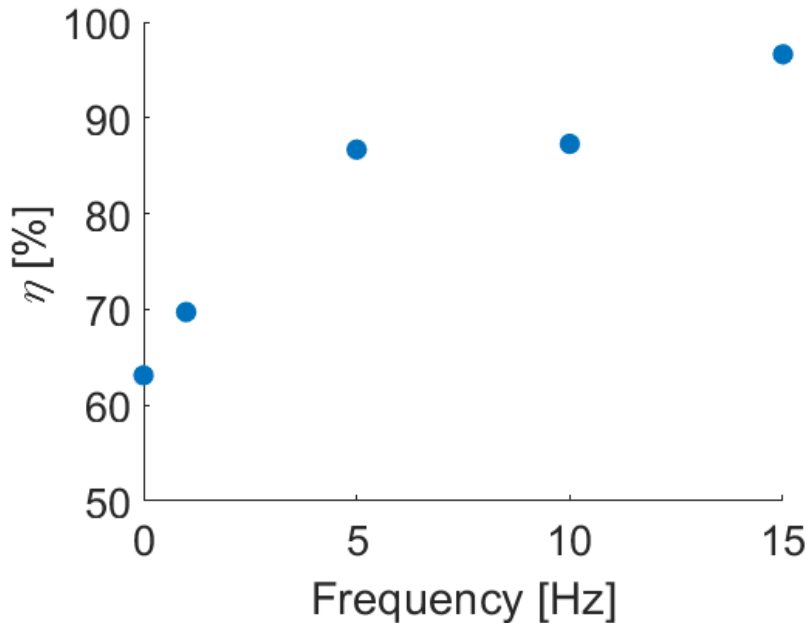


**Figure 6-9:** Mixing efficiencies ( $\eta$  in Equation 6-2) in the second module in relation to the frequency at which the balloons in the first module were actuated. This experiment occurred at a  $Re$  (Equation 1-1) of 0.0015 and a  $Pe_{balloon}$  (Equation 6-3) of 525, 2625, 5250, and 7875 for balloon actuation frequencies of 1, 5, 10, and 15 Hz, respectively. When the balloons were not actuating, the flow had a  $Pe$  of 0.745.

## 6.4 Discussion

### 6.4.1 Improving Mixing Within the Balloon Module

Although the balloon module was shown to be effective when mixing two samples before the mixture flowed into the second module on the motherboard, the following considerations must be taken when using the motherboard and module

combination for a mechanobiological study. The following considerations may be used to improve the balloon module in future works.

In Chapter 6.3 it was shown that by increasing the mixing frequency of the balloons, the device had a greater mixing efficiency. In this study, mixing frequencies ranged from 0 to 15 Hz. Higher mixing frequencies were attempted, but at frequencies above 15 Hz, the balloons of the balloon module became unresponsive and could not inflate. Unresponsiveness of the balloons at frequencies greater than 15 Hz may be due to the response time of the solenoid valve. At large frequencies, the MOSFET Arduino appeared responsive as its indicator light flashed at the input frequency, but the balloons remained deflated on the device indicating that the solenoid valve was not powered because it is a normally closed solenoid valve.

Typical solenoid valves work by using an inductor to move a plunger within the solenoid as shown below in Figure 6-10. For a normally closed solenoid valve, when it is not powered, the plug blocks the inlet channel of the solenoid. When the solenoid is powered, the plug moves, and the inlet channel is no longer blocked. At higher frequencies, the activation time per cycle of solenoid motion is reduced. For the solenoid valve used in this study, the activation time at frequencies higher than 15 Hz may be too short to move the plunger of the solenoid, and thus it remains closed.

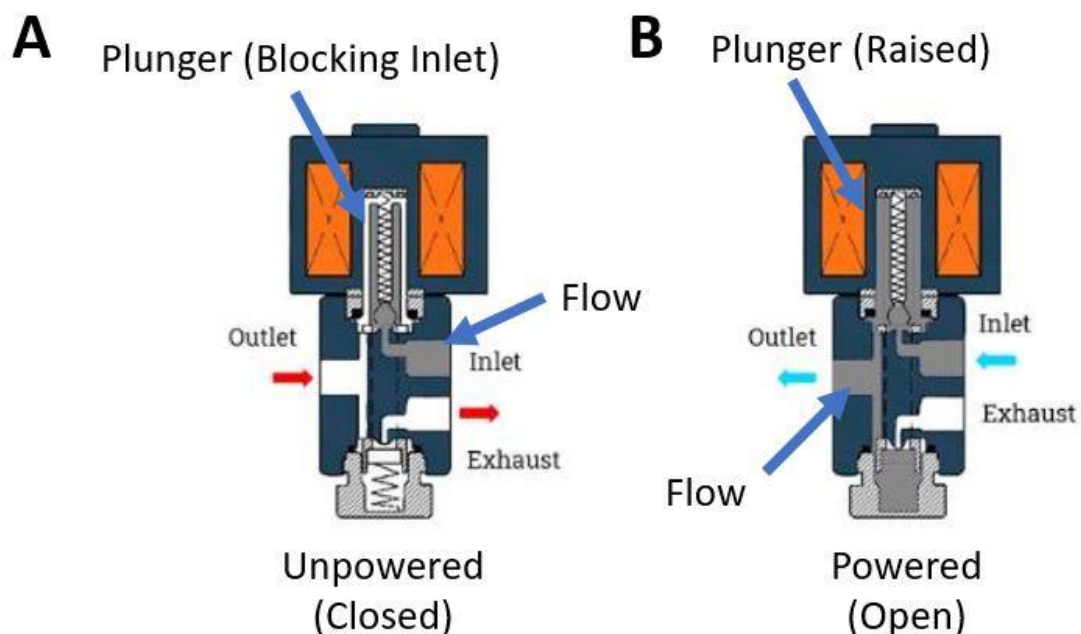


**Figure 6-10:** Function of a 3 way normally closed solenoid valve. Dark gray shows the flow of air through the solenoid valve. The plunger moves when powered to connect the inlet and outlet of the valve. (A) Schematic of the solenoid valve when it is unpowered, and the inlet channel is closed. (B) Schematic of the solenoid valve when it is powered, and the inlet channel is connected to the outlet of the valve. Adapted from [94].

To understand the mechanisms behind the mixing of the two samples due to the actuation of the PDMS balloons, a literature survey was conducted. Although there are microfluidic devices with similar methods of mixing two samples, there were no papers that offered a relation between mixing efficiency, the parameters of the balloons, and the parameter of the flow. As such, the following paragraphs offer possible ways to improve the mixing efficiency of the device based on my own observations and intuition.

Possible ways to increase the mixing efficiency of the balloon module might be to decrease the flow channel height, decrease the flow speed of the two dyes, increase the number of balloons on the device, increase the diameter of the balloons, or increase the effect of diffusion. The goal behind these suggestions is to increase the local  $Pe$  number around each balloon. The local  $Pe$  developed for the balloons is shown below.

$$Pe_{balloon} = \frac{u_{balloon}L}{D} = \frac{2fH2R}{D} = \frac{4fHR}{D}, \quad (6-3)$$

where  $Pe_{balloon}$  is the local  $Pe$  number due to balloon motion,  $u_{balloon}$  is the speed of the balloon during inflation,  $L$  is the characteristic length of the flow,  $D$  is the diffusion coefficient of the dyes into each other,  $f$  is the frequency of balloon inflation,  $H$  is the height of the balloon at full inflation, and  $R$  is balloon radius.  $D$  was assumed to be  $2 \times 10^{-9}$  m<sup>2</sup>/s based on values found in previous literature [95].

As the  $Pe_{balloon}$  increases, the mixing due to the balloon motion also increases. For frequencies ( $f$ ) of 1, 5, 10, and 15 Hz, the  $Pe_{balloon}$  values were 2,100, 10,500, 21,000, and 31,500, respectively. The increase in  $Pe_{balloon}$  as  $f$  increases indicates that as  $f$  increases, the mixing from advection become more efficient. Additionally, for the 0 Hz case,  $Pe$  was found to be 0.745.  $Pe$  was used to quantify the affect of advection in place of  $Pe_{balloon}$  because at 0 Hz, the balloons did not have any affect on the mixing.

As described by the Equation 6-3, it was found that as the inflation frequency of the balloon increased, the mixing efficiency increased. Although the maximum frequency of inflation was limited by the solenoid valve, further increasing the inflation frequency may lead to a greater mixing efficiency.

Similarly, increasing the inflation height of the balloons of the balloon module may increase the mixing within the module as the velocity of the balloon is a function of its inflation height and frequency. Previously in Chapter 4.4, it was shown that by increasing the balloon diameters, the balloon height also increases. Additionally, Equation 4-1 indicates that the inflation height of the balloons can be increased by increasing applied pressure, decreasing Young's Modulus of PDMS, or by decreasing balloon thickness. Although any of these properties can be changed to affect balloon height, it was previously found that balloon height had a weak dependence on balloon thickness [67]. Therefore, balloon diameter will have the biggest role in determining balloon height. Additionally, with larger balloon diameters, the characteristic length of the flow generated by the balloon increases, increasing  $Pe_{balloon}$ .

#### **6.4.2 Pulsatile Flow Motion Due to Balloon Inflation**

During mixing, the balloons of the balloon module were dynamically inflated and deflated. Flow within a microchannel typically has very low Reynolds Numbers (Equation 1-1), and as such, flow information can travel very far up- or down-stream without dissipating. As such, in our microchannel, the pulsatile motion of the balloons of the balloon module created a pulsatile motion within the flow field of the second microfluidic module. Pulsatile flow within the mixing module is shown below in Figure 6-11 for visibility.

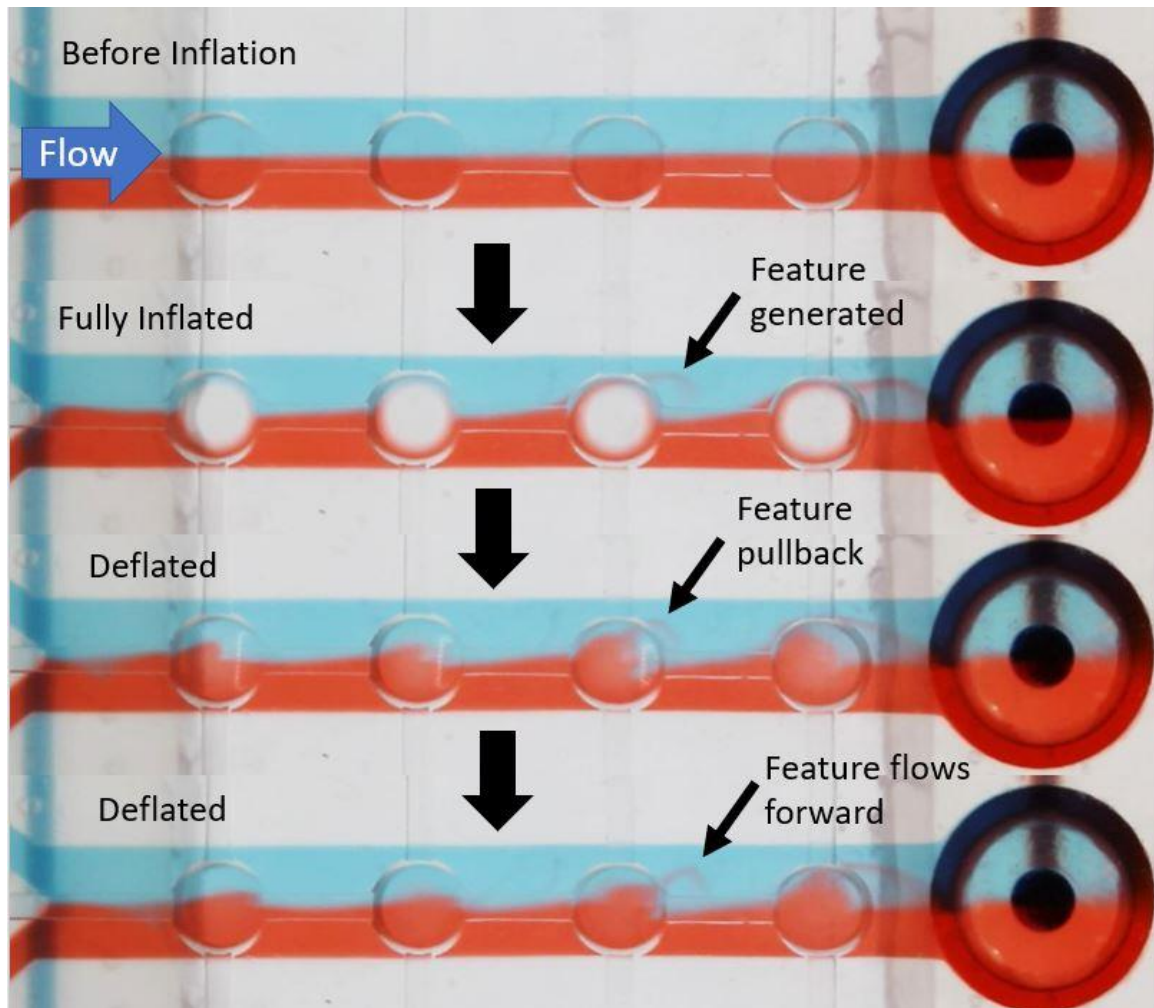


**Figure 6-11:** Images of the mixing module to visually demonstrate the pulsatile flow characteristics of the device. Before inflation, no flow features were generated. After the balloon has been inflated, a vortex has been generated after the third balloon. When the balloon deflates, the feature is pulled back toward the balloons. Then the feature flows forward with the bulk motion of the flow.

The pulsatile motion within the second module would impact the ability of the second channel to apply a consistent and predictable level of shear stress to the walls of

the channel. Although the investigation was not conducted in this work, future PTV experiments could be conducted to understand the effect of the pulsatile balloon motion on the flow in the second module. Additionally, the effects of the pulsatile motion may be reduced by increasing the volume flowrate through both channels, making the inertial properties of the flow more significant. Increasing the volume flowrate through the channels may also reduce the mixing efficiency of the balloon module. Increasing the channel length of the motherboard or adding dampening components to the channels may also reduce the effects of balloon movement on the flow.

### **6.5 Possible Future Applications**

The microfluidic motherboard, balloon module, and straight-channel module used in this study were designed to function as a platform for mixing two samples before applying shear stress to cells cultured in the straight-channel module. Although cellular experimentation was not conducted due to time constraints, it is plausible the device would be effective based on previous cell experimentation and the characterization conducted in this study. Beyond the application described, there are many other applications for the motherboard and modules developed in this study.

Due to the use of 3D printing to fabricate the motherboard, the design and channel configuration can easily be changed and updated to the end-users need. It is possible to combine modules in series or parallel, increase or decrease the number of modules, change the connections between the modules, and stack them on top of each other. Due to its versatility, the modular motherboard can be used with a wide variety of applications.

Additionally, due to its O-ring like connectors, new modules can easily be designed to operate with the motherboard.

The balloon module also has many other potential applications. Previously, it was shown that the balloons of the microfluidic device were capable of applying compression to cells embedded within a hydrogel scaffold [48]. Therefore, the balloon device fabricated in this study may similarly be able to apply compression to cells. Additionally, because the balloon module in this device also has a channel for flow, shear stress and compression could be applied simultaneously. As discussed, previously cells communicate with each other and respond to mechanical stimulus by releasing biomolecules [96]. As such, it may be possible to use the modular platform to enable communication between cells to create body-on-a-chip devices [97].

As such, one could envision an experiment where the current motherboard is combined with two balloon modules, each one containing a different cell type. The responses of the cells to compression and shear stress, as well as their communication could be studied for further understanding of the mechanobiology of the cells.

Another way that the balloon module may be used is to apply tension and shear stress to a cell monolayer. If a cell monolayer was cultured over the balloons of the balloon module, tension may be applied to the monolayer when the balloons are inflated. Due to cell-cell adhesion in a cell monolayer, if the total length of the monolayer is increased, the monolayer may experience tension [98, 99]. As such, the balloon module may be capable of applying either static or dynamic tension and shear stress to cells simultaneously.

Some additional applications for the balloon module beyond mechanobiological studies may include using the balloon as an adaptable lens for microscopic imaging [100], using the inflated balloons to block a channel to create the base of a programmable microfluidic [101], or a droplet generator which induces droplet pinch-off by restricting the drop with the deformable membrane [102]. Overall, the microfluidic motherboard and modules presented in this study are meant to serve as a base for future scientists to adapt for their specific application. The motherboard and its modules can be expanded for any use so long as the person developing it has the creativity.

## **Chapter 7: Conclusion and Prospective Research**

### **7.1 Conclusion**

Microfluidic organ-on-chip devices will play an increasingly important role in understanding the mechanobiology of a cell and in the development of new treatments for disease due to their versatility, use of minimal resources, tight control, and ease of use. Further expanding the versatility and eliminating some of the limitations of microfluidics through the use of modular platforms, will enable faster experimentation with microfluidics and increase their accessibility. In this study, we have developed a multi-use modular microfluidic platform using 3D printing that can easily be configured for various uses. Due to its use of 3D printing and high modularity, it can be easily redesigned and fabricated, removing many of the downfalls of traditional microfluidic fabrication and design.

To demonstrate the capability of the modular microfluidic platform, a hypothetical mechanobiological experiment was established where two samples were mixed in the balloon module, connected to the first slot of the motherboard, before applying shear stress to cells in the second module of the motherboard. The 3D printing procedure and design features of the motherboard and modules were optimized for microfluidic fabrication and operation while being simple and easily recreated. Then, the balloon inflation performance, shear stress application, and mixing performance of the modules were characterized for future use with cell culture. The data presented in this study shows that the multi-use modular microfluidic platform is suitable for cell mechanobiology experimentation, and that the platform has a high capacity to be used for various uses required by the end-user.

## 7.2 Prospective Research Directions

The motherboard and modules developed will be used for future cell experimentation. Currently, there is interest in culturing bile duct cells, bone cells, and endothelial cells for the study of bile duct cancer, osteoporosis, and atherosclerosis, respectively. The balloon module may be used to mix samples, apply compression to cells, apply tension to cells, and apply shear stress to cells, while the motherboard allows cells to communicate across modules. Upon implementation into mechanobiology research areas, user-feedback will be collected to improve the platform to better suit the needs of the consumer. The modularity and connectivity of the platform may enable the creation of a body-on-chip system where various organ-on-chip systems can be used to mimic most of the human body.

Additionally, future research may focus on the development of new multi-use modules to continue to expand the use of the platform even further. Applications outside of cell mechanobiology such as using the balloon module as an adaptable lens for microscopy imaging, as a droplet generator, or as the base of a programable microfluidic platform may also be developed.

## References

- [1] D. Duffy, J. C. McDonald, O. Schueller, and G. Whitesides, 1998, "Rapid Prototyping of Microfluidic Systems in Poly(dimethylsiloxane)," *Analytical Chemistry*, 70, pp. 4974 - 4984.
- [2] H. A. Stone, A. D. Stroock, and A. Ajdari, 2004, "Engineering flows in small devices: Microfluidics toward a Lab-on-a-Chip," *Annu. Rev. Fluid Mech.*, 36, pp. 381 - 411.
- [3] M. A. Burns, B. N. Johnson, S. N. Brahmaandra, K. Handique, J. R. Webster, M. Krishnan, T. S. Sammarco, P. M. Man, D. Jones, D. Heldsinger, C. H. Mastrangelo, and D. T. Burke, 1998, "An integrated nanoliter DNA analysis device," *Science*, 282, pp. 484 - 487.
- [4] T. Thorsen, S. J. Maerkl, and S. R. Quake, 2002, "Microfluidic large-scale integration," *Science*, 298, pp. 580 - 584.
- [5] C. M. Leung, P. d. Haan, K. Ronaldson-Bouchard, G.-A. Kim, J. Ko, H. S. Rho, Z. Chen, P. Habibovic, N. L. Jeon, S. Takayama, M. Shuler, G. Vunjak-Novakovic, O. Frey, E. Verpoorte, and Y.-C. Toh, 2022, "A guide to the organ-on-a-chip," *Nature Reviews*, 2, p. 33.
- [6] D. Huh, Y.-s. Torisawa, G. Hamilton, H. J. Kim, and D. Ingber, 2012, "Microengineered physiological biomimicry: Organs-on-Chips," *Lab on a Chip*, 12, pp. 2156 - 2164.
- [7] W. Zheng, B. Jiang, D. Wang, W. Zhang, Z. Wang, and X. Jiang, 2012, "A microfluidic flow-stretch chip for investigating blood vessel biomechanics," *Lab on a Chip*, 12, pp. 3441 - 3450.

- [8] L. Charelli, J. Ferreira, C. Naveira-Cotta, and T. Balbino, 2021, "Engineering mechanobiology through organoids-on-chip: A strategy to boost therapeutics," *J Tissue Eng Regen Med.*, 15, pp. 883 - 899.
- [9] P. Cui, and S. Wang, 2019, "Application of microfluidic chip technology in pharmaceutical analysis: A review," *Journal of Pharmaceutical Analysis*, 9, pp. 238 - 247.
- [10] A. R. Perestrelo, A. Aguas, A. Rainer, and G. Forte, 2015, "Microfluidic organ/body-on-a-chip devices at the convergence of biology and microengineering," *Sensors*, 15, pp. 31142 - 31170.
- [11] Y. Nakao, H. Kimura, Y. Sakai, and T. Fujii, 2011, "Bile canaliculi formation by aligning rat primary hepatocytes in a microfluidic device," *Biomicrofluidics*, 5, 022212, pp. 1-7.
- [12] K.-J. Jang, and K.-Y. Suh, 2010, "A multi-layer microfluidic device for efficient culture and analysis of renal tubular cells," *Lab on a Chip*, 10, pp. 36 - 42.
- [13] D. Huh, B. D. Matthews, A. Mammoto, M. Montoya-Zavala, H. Y. Hsin, and D. E. Ingber, 2010, "Reconstituting organ-level lung functions on a chip," *Science*, 328, pp. 1662 - 1668.
- [14] J. H. Sung, and M. L. Shuler, 2009, "A micro cell culture analog ( $\mu$ CCA) with 3-D hydrogel culture of multiple cell lines to assess metabolism-dependent cytotoxicity of anti-cancer drugs," *Lab on a Chip*, 9, pp. 1385 - 1394.
- [15] S.-M. Yang, S. Lv, W. Zhang, and Y. Cui, 2022, "Microfluidic point-of-care (POC) devices in early diagnosis: A review of opportunities and challenges," *Sensors*, 22, 1620, pp. 1 - 33.

- [16] J. L. Davidson, J. Wang, M. K. Maruthamuthu, A. Dextre, A. Pascual-Garrigos, S. Mohan, S. V. S. Putikam, F. O. I. Osman, D. McChesney, J. Seville, and M. S. Verma, 2021, "A paper-based colorimetric molecular test for SARS-CoV-2 in saliva," *Biosensors and Bioelectronics: X*, 100076.
- [17] E. Samiei, M. Tabrizian, and M. Hoorfar, 2016, "A review of digital microfluidics as portable platforms for lab-on-a-chip applications," *Lab on a Chip*, 16, pp. 2376 - 2396.
- [18] A. Sinha, T.-Y. Tai, K.-H. Li, P. Gopinathan, Y.-D. Chung, I. Sarangadharan, H.-P. Ma, P.-C. Huang, S.-C. Shiesh, Y.-L. Wang, and G.-B. Lee, 2019, "An integrated microfluidic system with field-effect-transistor sensor arrays for detecting multiple cardiovascular biomarkers from clinical samples," *Biosensors and Bioelectronics*, 129, pp. 155 - 163.
- [19] J. Li, Y. Sun, C. Chen, T. Sheng, P. Liu, and G. Zhang, 2019, "A smartphone-assisted microfluidic chemistry analyzer using image-based colorimetric assays for multi-index monitoring of diabetes and hyperlipidemia," *Analytica Chimica Acta*, 1052, pp. 105 - 112.
- [20] S. Terry, J. Jerman, and J. Angell, 1979, "A Gas Chromatographic Air Analyzer Fabricated on a Silicon Wafer," *IEEE Transactions on Electron Devices*, pp. 1880 - 1886.
- [21] G. M. Whitesides, 2006, "The origins and the future of microfluidics," *Nature*, 442, pp. 368 - 373.
- [22] V. Faustino, S. O. Catarino, R. Lima, and G. Minas, 2016, "Biomedical microfluidic devices by using low-cost fabrication techniques: A review," *Journal of Biomechanics*, 49, pp. 2280 - 2292.

- [23] A.-G. Niculescu, C. Chircov, A. C. Birca, and A. M. Grumezescu, 2021, "Fabrication and applications of microfluidic devices: a review," *International Journal of Molecular Sciences*, 22, 2011, pp. 1 - 26.
- [24] J. Hwang, Y. H. Cho, M. S. Park, and B. H. Kim, 2019, "Microchannel fabrication on glass materials for microfluidic devices," *International Journal of Precision Engineering and Manufacturing*, 20, pp. 479 - 495.
- [25] M. Wilson, N. Kota, Y. Kim, Y. Wang, D. Stolz, P. LeDuc, and O. B. Ozdoganlar, 2011, "Fabrication of circular microfluidic channels by combining mechanical micromilling and soft lithography," *Lab on a Chip*, 11, pp. 1550 - 1555.
- [26] B. Xue, Y. Geng, Y. Yan, G. Ma, D. Wang, and Y. He, 2020, "Rapid prototyping of microfluidic chip with burr-free PMMA microchannel fabricated by revolving tip-based micro-cutting," *Journal of Materials Processing Tech.*, 227, 116468, pp. 1 - 14.
- [27] R. Martinez-Duarte, and M. Madou, 2012, "SU-8 photolithography and its impacts on microfluidics," *Microfluidic and nanofluidics handbook: Fabrication, implementation, and applications*, S. M. a. S. Chakraborty, ed., CRC Press, pp. 231 - 268.
- [28] V. Mehta, and S. Rath, 2021, "3D printed microfluidic devices: a review focused on four fundamental manufacturing approaches and implications on the field of healthcare," *Bio-Design and Manufacturing*, 4, pp. 311 - 343.
- [29] J. Dong, J. Liu, G. Kang, J. Xie, and Y. Wang, 2014, "Pushing the resolution of photolithography down to 15nm by surface plasma interference," *Scientific Reports*, 4, 5618, pp. 1 - 6.

- [30] B. Carnero, C. Bao-Varela, A. I. Gomez-Varela, E. Alvarez, and M. T. Flores-Arias, 2021, "Microfluidic devices manufacturing with a stereolithographic printer for biological applications," *Materials Science & Engineering C* 129(112388).
- [31] Y. K. A. Ahmadianyazdi, and A. Folch, 2023, "A 'print-pause-print' protocol for 3D printing microfluidics using multimaterial stereolithography," *Nature Protocols*, 18, pp. 1243 - 1259.
- [32] M. I. Mohammed, S. Haswell, and I. Gibson, 2015, "Lab-on-a-chip or chip-in-a-lab: Challenges of commercialization lost in translation," *Procedia Technology*, 20, pp. 54 - 59.
- [33] X. Lai, M. Yang, H. Wu, and D. Li, 2022, "Modular microfluidics: Current status and future prospects," *Micromachines*, 13, 1363, pp. 1 - 22.
- [34] K. A. Shaikh, K. S. Ryu, E. D. Goluch, J.-M. Nam, J. Liu, C. S. Thaxton, T. N. Chiesl, A. E. Barron, Y. Lu, C. A. Mirkin, and C. Liu, 2005, "A modular microfluidic architecture for integrated biochemical analysis," *PNAS*, 102, pp. 9745 - 9750.
- [35] C. Emeigh, A. Griswold, R. H. Pallock, J. Sahni, M. Schake, U. Anuta, J. Deters, and S. Ryu, 2023, "Group-project-based development of a modular microfluidic platform: A case report on a hands-on microfluidics course," American Society for Engineering Education Midwest Section Conference 2023Lincoln, NE, USA.
- [36] K. C. Bhargava, B. Thompson, and N. Malmstadt, 2014, "Discrete elements for 3D microfluidics," *PNAS*, 111, pp. 15013 - 15018.
- [37] D.-S. Liou, Y.-F. Hsieh, L.-S. Kuo, C.-T. Yang, and P.-H. Chen, 2011, "Modular component design for portable microfluidic devices," *Microfluid Nanofluid*, 10, pp. 465 - 474.

- [38] J. Atencia, G. A. Cooksey, A. Jahn, J. M. Zook, W. N. Vreeland, and L. E. Locascio, 2009, "Magnetic connectors for microfluidic applications," *Lab on a Chip*, 10, pp. 246 - 249.
- [39] P. Skafto-Pedersen, C. G. Sip, A. Folch, and M. Dufva, 2013, "Modular microfluidic systems using reversibly attached PDMS fluid control modules," *J. Micromech. Microeng.*, 23, 055011, pp. 1 - 10.
- [40] K. Vittayarukskul, and A. P. Lee, 2017, "A truly Lego-like modular microfluidics platform," *J. Micromech. Microeng.*, 27, 035004, pp. 1 - 14.
- [41] W. Polacheck, R. Li, S. Uzel, and R. Kamm, 2013, "Microfluidic platforms for mechanobiology," *Lab on a Chip*, 13, pp. 2252 - 2267.
- [42] J. H. Wang, and B. P. Thampatty, 2006, "An introductory review of cell mechanobiology," *Biomechan Model Mechanobiol*, 5, pp. 1 - 16.
- [43] G. Yang, R. Crawford, and J. Wang, 2004, "Proliferation and collagen production of human patellar tendon fibroblasts in response to cyclic uniaxial stretching in serum-free conditions," *Journal of Biomechanics*, 37, pp. 1543 - 1550.
- [44] E. Yildiz-Ozturk, and O. Yesil-Celiktas, 2015, "Diffusion phenomena of cells and biomolecules in microfluidic devices," *Biomicrofluidics*, 9, 052606, pp. 1 - 18.
- [45] D. Ingber, 2003, "Mechanobiology and diseases of mechanotransduction," *Annals of Medicine*, 35, pp. 564 - 577.
- [46] N. Zuela-Sopilniak, and J. Lammerding, 2022, "Can't handle the stress? Mechanobiology and disease," *Trends in Molecular Medicine*, 28, pp. 710 - 725.

- [47] D. Lee, A. Erickson, A. T. Dudley, and S. Ryu, 2019, "A microfluidic platform for stimulating chondrocytes with dynamic compression," *Journal of Visualized Experiments*, 151, e59676, pp. 1 - 10.
- [48] D. Lee, A. Erickson, T. You, A. T. Dudley, and S. Ryu, 2018, "Pneumatic microfluidic cell compression device for high-throughput study of chondrocyte mechanobiology," *Lab on a Chip*, 18, pp. 2077 - 2086.
- [49] J. Zhang, S. Yan, D. Yuan, G. Alici, N.-T. Nguyen, M. E. Warkiani, and W. Li, 2016, "Fundamentals and applications of inertial microfluidics: a review," *Lab on a Chip*, 16, pp. 10 - 34.
- [50] S. M. Saravanakumar, and P.-V. Cicek, 2023, "Microfluidic mixing: A physics-oriented review," *Micromachines*, 14, 1827, pp. 1 - 26.
- [51] C. Chen, B. Mehl, A. Munshi, A. Townsend, D. Spence, and R. Martin, 2016, "3D-printed microfluidic devices: fabrication, advantages and limitations - a mini review," *Analytical Methods*, 8, pp. 6005-6012.
- [52] R. Amin, S. Knowlton, A. Hart, B. Yenilmez, F. Ghaderinezhad, S. Katebifar, M. Messina, A. Khademhosseini, and S. Tasoglu, 2016, "3D-printed microfluidic devices," *Biofabrication*, 8, 022001, pp. 1 - 16.
- [53] Y. Xu, F. Qi, H. Mao, S. Li, Y. Zhu, J. Gong, L. Wang, N. Malmstadt, and Y. Chen, 2022, "In-situ transfer vat photopolymerization for transparent microfluidic device fabrication," *Nature Communications*, 13, 918, pp. 1 - 11.
- [54] S. Altundemir, A. Uguz, and K. Ulgen, 2017, "A review on wax printed microfluidic paper-based devices for international health," *Biomicrofluidics*, 11, 041501, pp. 1 - 26.

- [55] G. Gaal, M. Mendes, T. Almeida, M. Piazzetta, A. Gobbi, A. R. Jr., and V. Rodrigues, 2017, "Simplified fabrication of integrated microfluidic devices using fused deposition modeling 3D printing," *Sensors and Actuators B*, 242, pp. 35 - 40.
- [56] R. Kurnoothala, S. Muthukumar, and K. Vishnubhatla, 2021, "Facile fabrication of integrated microfluidic SERS substrate by femtosecond laser sintering of silver nano particles," *Optical Materials*, 111, 110518, pp. 1 - 7.
- [57] P. Mali, A. Sarkar, and R. Lal, 2005, "Facile fabrication of microfluidic systems using electron beam lithography," *Lab on a Chip*, 6, pp. 310-315.
- [58] C. CADWorks, <https://creativcad.works/miicraft-ultra/>.
- [59] P. Cooley, D. Wallace, and B. Antohe, 2002, "Applications of ink-jet printing technology to BioMEMS and microfluidic systems," *JALA Automation Review*, 7, 5, pp. 33 - 39.
- [60] S. Shahriar, V. Patel, and P. Selvaganapathy, 2023, "Xurography as a tool for fabrication of microfluidic devices," *J. Micromech. Microeng.*, 33, 083002, pp. 1 - 22.
- [61] J. R. Tumbleston, D. Shirvanyants, N. Ermoshkin, R. Januszewicz, A. R. Johnson, D. Kelly, K. Chen, R. Pinschmidt, J. P. Rolland, A. Ermoshkin, E. T. Samulski, and J. M. DeSimone, 2015, "Continuous liquid interface production of 3D objects," *Science*, 347(6228), pp. 1349 - 1352.
- [62] C. Emeigh, H. Zhang, and S. Ryu, 2022, "Fabrication of a microfluidic cell compressor using a 3D-printed mold," ASME Fluids Engineering Division Summer Meeting 2022, ASME FEDSM2022-87613, Toronto, Canada.

- [63] S. Shanmugasundaram, J. Razmi, J. Mian, and L. Ladani, 2020, "Mechanical anisotropy and surface roughness in additively manufactured parts fabricated by stereolithography (SLA) using statistical analysis," *Materials*, 13, 2496, pp. 1 - 27.
- [64] L. Flanagan, V. Singh, and C. Willson, 1999, "Surface roughness development during photoresist dissolution," *J. Vac. Sci. Technol. B*, 17, pp. 1371 - 1379.
- [65] MiiCraft, <https://miicraft.ca/microfluidics/>.
- [66] L. Zhao, Z. Jiang, C. Zhang, W. Guo, Z. Jiang, X. Gao, Y. Cui, and X. Shi, 2021, "Theoretical modeling based on stress wave propagation and experimental verification of residual stress in stereolithography printer ZrO<sub>2</sub> ceramic suspensions," *Ceramics International*, 47, pp. 26935 - 26941.
- [67] C. Emeigh, R. Pineda, B. Harms, and S. Ryu, 2023, "The effects of balloon thickness on the viability of a microfluidic cell compression device," American Society of Mechanical Engineers International Mechanical Engineering Congress and Exposition 2023, ASME IMECE2023-113642, New Orleans, LA, USA.
- [68] N. Nguyen, and S. Wereley, 2006, *Fundamentals and Applications of Microfluidics*, Artech House.
- [69] C. Emeigh, and S. Ryu, 2024, "Using brightfield microscopy to assess the balloon expansion performance of a microfluidic cell compression device," Accepted for Presentation, American Society of Mechanical Engineers Fluids Engineering Division Summer Meeting, ASME FEDSM2024-130787 Anaheim, CA, USA.
- [70] Y. Fainman, L. Lee, D. Psaltis, C. Yang, S. Tang, and G. Whitesides, 2009, "Chapter 2: Basic Microfluidic and Soft Lithographic Techniques," *Optofluidics: Fundamentals, Devices, and Applications* McGraw Hill.

- [71] R. E. Pawinanto, J. Yunas, and A. M. Hashim, 2020, "Micropillar based active microfluidic mixer for the detection of glucose concentration," *Microelectronic Engineering*, 234, 111452, pp. 1 - 10.
- [72] T. Sato, K. Kaneko, T. Hayakawa, and H. Suzuki, 2023, "Pneumatic microballoons for active control of the vibration-induced flow," *Micromachines*, 14, 2010, pp. 1 - 13.
- [73] J. J. Vlassak, and W. D. Nix, 1992, "A new bulge test technique for the determination of Young's modulus and Poisson's ratio of thin films," *J. Mater. Res.*, 7, 12, pp. 3242 - 3249.
- [74] D. Lee, M. Rahman, Y. Zhou, and S. Ryu, 2015, "Three-dimensional confocal microscopy indentation method for hydrogel elasticity measurement," *Langmuir*, 31, pp. 9684 - 9693.
- [75] I. Kasa, 1976, "A circle fitting procedure and its error analysis," *IEEE Transactions on Instrumentation and Measurement*, March, 1976, pp. 8 - 14.
- [76] N. Bohlim, D. Lee, S. Ryu, and R. A. Wilson, 2021, "Mimicking the surface mechanical properties of rice (*Oryzae sativa*) leaf using PDMS soft lithography," *JMST Advances*, 3, pp. 11 - 17.
- [77] S. Inoue, 1986, *Video Microscopy*, Springer Science & Business Media.
- [78] S. Inoue, 1997, *Video microscopy: The Fundamentals*, Springer.
- [79] S. Moorbath, J. H. Allaart, D. Bridgwater, and V. R. McGregor, 1976, "Laser speckle photography in a fluid medium," *Nature*, 270, 3, pp. 45 - 47.
- [80] T. Dracos, 1996, "Particle Tracking Velocimetry (PTV) Basic Concepts," *Three-Dimensional Velocity and Vorticity Measuring and Image Analysis Techniques*, Kluwer Academic Publishers, pp. 155 - 160.

- [81] S. Wereley, and C. Meinhart, 2009, "Recent advances in micro-particle image velocimetry," *Annu. rev. Fluid Mech.*, 42, pp. 557 - 576.
- [82] R. Lindken, M. Rossi, S. Grobe, and J. Westerweel, 2009, "Micro-particle image velocimetry ( $\mu$ PIV): Recent developments, applications, and guidelines," *lab on a Chip*, 9, pp. 2251 - 2567.
- [83] P. Salipante, S. Hudson, J. Schmidt, and J. Wright, 2017, "Microparticle tracking velocimetry as a tool for microfluidic flow measurements," *Exp. Fluids*, 58, 85, pp. 1 - 10.
- [84] A. Bhagat, and I. Papautsky, 2008, "Enhancing particle dispersion in a passive planar micromixer using rectangular obstacles," *J. Micromech. Microeng.*, 18, 085005, pp. 1 - 9.
- [85] D. D. Carlo, D. Irimia, R. Tompkins, and M. Toner, 2007, "Continuous inertial focusing, ordering, and separation of particles in microchannels," *Proceedings of the National Academy of Sciences*, 104, pp. 18892 - 18897.
- [86] M. Raffel, C. Willert, F. Scarano, C. Kahler, S. Wereley, and J. Kompenhans, 2018, *Particle Image Velocimetry: a Practical Guide*, Springer.
- [87] A. Einstein, 1905, "On the movement of small particles suspended in stationary liquids required by the molecular-kinetic theory of heat," *Annalen der Physik*, 17, pp. 549 - 560.
- [88] J. G. Santiago, S. T. Wereley, C. D. Meinhart, D. J. Beebe, and R. J. Adrian, 1998, "A particle image velocimetry system for microfluidics," *Experiments in Fluids*, 25, pp. 316 - 319.

- [89] M. Mielnik, and L. Saeiran, 2004, "Micro particle image velocimetry - an overview," *Turbulence*, 10, pp. 83 - 90.
- [90] F. White, 2010, Fluid Mechanics, McGraw-Hill.
- [91] D. Blair, and E. Dufresne, "The MATLAB Particle Tracking Code Repository," <https://site.physics.georgetown.edu/matlab/index.html>.
- [92] F. White, 2005, Viscous Fluid Flow, McGraw Hill.
- [93] Z. Li, and S.-J. Kim, 2017, "Pulsatile micromixing using water-head-driven microfluidic oscillators," *Chemical Engineering*, 313, pp. 1364 - 1369.
- [94] IQS, 2024, "3-Way Solenoid Valves," <https://www.iqsdirectory.com/articles/solenoid-valve/3-way-solenoid-valves.html>.
- [95] A. Konda, D. Lee, T. You, X. Wang, S. Ryu, and S. A. Morin, 2019, "Reversible mechanical deformations of soft microchannel networks for sensing in soft robotic systems," *Adv. Intell. Syst.*, 1.
- [96] L. Plotkin, N. Sanz, and L. Brun, 2023, "Messages from the mineral: How bone cells communicate with other tissues," *Calcified Tissue International*, 113, pp. 39 - 47.
- [97] J. H. Sung, Y. I. Wang, N. Sriram, M. Jackson, C. Long, J. J. Hickman, and M. L. Shuler, 2019, "Recent advances in body-on-a-chip systems," *Analytical Chemistry*, 91, pp. 330 - 351.
- [98] V. Braga, 2002, "Cell-cell adhesion and signalling," *Current Opinion in Cell Biology*, 14, pp. 546 - 556.
- [99] R. Yang, J. Broussard, K. Green, and H. Espinosa, 2018, "Techniques to stimulate and interrogate cell-cell adhesion mechanics," *Extreme Mechanics Letters*, 20, pp. 125 - 139.

- [100] S. Camou, H. Fujita, and T. Fugjii, 2003, "PDMS 2D optical lens integrated with microfluidic channels: principle and characterization," *Lab on a Chip*, 3, pp. 40 - 45.
- [101] L. Fidalgo, and S. Maerkl, 2011, "A software-programmable microfluidic device for automated biology," *Lab on a Chip*, 11, pp. 1612 - 1619.
- [102] A. Raj, R. Halder, P. Sajeesh, and A. Sen, 2016, "Droplet generation in a microchannel with a controllable deformable wall," *Microfluid Nanofluid*, 20, 102, pp. 1 - 16.

## Appendix A: MATLAB Code Used for Balloon Height Image Processing

```

% Balloon Height Analyzer code for measuring the inflation height of a
balloon scanned with the Keyence Laser Scanning microscope
% Written by Carson Emeigh on 4-11-2023
% Input is a .csv file that is a matrix containing the Z coordinates where the
cell represents the x and y coordinates.

1  clear all
2  close all
3  clc
4
5  tolerance = 5; % Thickness of each slice generated later. Slices used to see
6  where center of balloon is.
7  Zstep = 30;% The amount of height between each slice that will be generated
8  later
9  ExclusionPercentage = 0; %percent of balloon that is excluded during plane
10 fitting
11
12 %% Load in the data
13
14 filename = 'D-2.5mm_balloon1.csv'; % Pick balloon to analyze
15 BalloonData = readmatrix(filename); % Takes data from .csv file and imports
16 into MATLAB.
17 BalloonData = smoothdata(BalloonData,'gaussian',10); % Apply Gaussian filter
18 to the data
19 Zcalibration = xlsread(filename,'B42:B42'); % Imports Z calibration values
20 Zcalibration = Zcalibration/1000; % Converts Z calibration into um
21 XYcalibration = xlsread(filename,'B41:B41'); % Imports XY calibration data.
22 XYcalibration = XYcalibration/1000000;
23 XYcalibration = XYcalibration*4; % Converts XY calibration data into mm per
24 pixel (*4 because of how data was exported)
25 [NumRows, NumCol] = size(BalloonData); % Returns the size of the data
26 BalloonData = BalloonData .* Zcalibration; % converts data from pixels into um
27
28 figure(1); % plot the raw data for visualization
29 s1 = surf(BalloonData); % Plots raw data
30 s1.LineStyle = 'none'; % Removes excess lines for clarity
31 hold on
32
33 %% Formats the data for plane fitting
34
35 % Deconstruct the height data matrix into a very long column vector
36 % to do linear regression and fit a plane to it.
37
38 X = [1:NumCol]; % Column vector of x coords
39 Y = [1:NumRows]; % column vector of x coords
40 [X, Y] = meshgrid(X,Y); %Creates matrix where each point is the x or y coord.
41 This helps me get the right repeating and length to be compatable with the
42 deconstructed height data matrix
43
44 X = reshape(X,[NumRows * NumCol,1]); % moved them back to column vector with
45 length the same number of entries as the height data column vector will have

```

```

46 Y = reshape(Y,[NumRows * NumCol,1]); % moved them back to column vector with
47 length the same number of entries as the height data column vector will have
48 Z = reshape(BalloonData,[NumRows * NumCol,1]); % takes height data matrix and
49 returns a column vector
50 data = [X,Y,Z]; % compiles all 3 column vectors into a single variable
51
52 % Plane fitting
53 Zmax = max(data(:,3));%finds max Z point for data exclusion
54 Zexclude = Zmax - ExclusionPercentage*Zmax; % Z limit for exclusion
55 options = fitoptions('Method','LinearLeastSquares','Exclude', data(:,3) >
56 Zexclude | data(:,3) == 0); %tells how to find fit, exclude portion of balloon
57 options.Robust = 'Bisquare';
58 ft = fitype('poly11'); % what type of fit (plane, polynomial, exponential,
59 ...)
60 plane = fit([data(:,1),data(:,2)],data(:,3),ft,options); %finds and fits a
61 plane
62 plot(plane) %plots the plane
63
64 %% Correct the tilt of the image. At each xy coord, subtract the z value of
65 the plane from the height z value.
66
67 planeCoeff = coeffvalues(plane); % puts plane coefficients into vector
68 [X, Y] = meshgrid([1:NumCol],[1:NumRows]); % move x and y back into matrix
69 planeZdata = planeCoeff(1) + planeCoeff(2) .* X + planeCoeff(3) .* Y; %
70 calculate the z value of the plane at each point in the matrix
71
72 BalloonData = BalloonData - planeZdata; % subtract the plane height from the
73 data point to correct the tilt of the image
74 figure(2);
75 s2 = surf(BalloonData); %plots the newly corrected data
76 s2.LineStyle = 'none';
77
78 %% Find max height for balloon
79
80 BalloonDataMax = max(max(BalloonData));
81
82 % Slice 1
83 [ParSlice1(1),ParSlice1(2)] = find(BalloonData == BalloonDataMax); % Output is
84 the row and column (X,Y value) of the maximum point.
85
86 %% Move down and find a slice of the balloon
87 % Slice 2
88 BalloonDataSlice2positions = find(BalloonData < BalloonDataMax-(Zstep-
89 tolerance) & BalloonData > BalloonDataMax-(Zstep+tolerance)); % Output is
90 location of slice 2 height values (30um+-2um from top)
91 BalloonDataSlice2values = BalloonData(BalloonDataSlice2positions(1:end)); %
92 Ouput is the values of the points in slice 2
93 BalloonDataSlice2 = zeros(NumRows,NumCol); % Initializes the matrix for slice
94 2. Array of zeros.
95
96 for i = 1:length(BalloonDataSlice2positions) % This for loop puts the values
97 into the slice 2 matrix at their positions
98     BalloonDataSlice2(BalloonDataSlice2positions(i)) =
99 BalloonDataSlice2values(i);
100 end

```

```

101
102 [BalloonDataSlice2X , BalloonDataSlice2Y] = find(BalloonDataSlice2 ~= 0); %
103 Ouput is XY values of points in slice 2. Last few steps convert matrix
104 indicies into row column format
105 BalloonDataSlice2XY = [BalloonDataSlice2X, BalloonDataSlice2Y]; % Combines row
106 column data into a single variable
107
108 ParSlice2 = CircleFitKasa(BalloonDataSlice2XY); %fits circle (CenterX,
109 CenterY, Radius)
110
111 for j = 1:360 % This for loops is part of the circle fitting
112     BalloonDataY2(j) = ParSlice2(2)+ParSlice2(3)*cos(j/360*2*pi);
113     BalloonDataX2(j) = ParSlice2(1)+ParSlice2(3)*sin(j/360*2*pi);
114 end
115
116 figure(7); % Starts plotting of the data
117 set(gcf,'Name','Balloon Slices');
118 subplot(3,1,1)
119 plot(BalloonDataSlice2X,BalloonDataSlice2Y,'o');
120 hold on
121 plot(BalloonDataX2, BalloonDataY2, '--r');
122 hold on
123 plot(ParSlice2(1),ParSlice2(2),'xm');
124 hold on
125 title('Slice 2 Points and Circular Fitting');
126 text(ParSlice2(1)+1,ParSlice2(2)+1,sprintf('Center = %0.2f , %0.2f | R = %0.2f
127 ',ParSlice2(1),ParSlice2(2),ParSlice2(3))); % Ends plotting of the data
128
129 % Slice 3: Exact same setup as slice 2. Only difference is where the slice
130 % is. Now it is 60um+-2um below the top.
131
132 BalloonDataSlice3positions = find(BalloonData < BalloonDataMax-(2*Zstep-
133 tolerance) & BalloonData > BalloonDataMax-(2*Zstep+tolerance));
134 BalloonDataSlice3values = BalloonData(BalloonDataSlice3positions(1:end));
135 BalloonDataSlice3 = zeros(NumRows,NumCol);
136
137 for i = 1:length(BalloonDataSlice3positions)
138     BalloonDataSlice3(BalloonDataSlice3positions(i)) =
139     BalloonDataSlice3values(i);
140 end
141
142 [BalloonDataSlice3X , BalloonDataSlice3Y] = find(BalloonDataSlice3 ~= 0);
143 BalloonDataSlice3XY = [BalloonDataSlice3X, BalloonDataSlice3Y];
144
145 ParSlice3 = CircleFitKasa(BalloonDataSlice3XY); %fits circle (CenterX,
146 CenterY, Radius)
147
148 for j = 1:360
149     BalloonDataY3(j) = ParSlice3(2)+ParSlice3(3)*cos(j/360*2*pi);
150     BalloonDataX3(j) = ParSlice3(1)+ParSlice3(3)*sin(j/360*2*pi);
151 end
152
153 subplot(3,1,2)
154 plot(BalloonDataSlice3X,BalloonDataSlice3Y,'o');
155 hold on

```

```

156 plot(BalloonDataX3, BalloonDataY3, '--r');
157 hold on
158 plot(ParSlice3(1),ParSlice3(2),'xm');
159 hold on
160 title('Slice 3 Points and Circular Fitting');
161 text(ParSlice3(1)+1,ParSlice3(2)+1,sprintf('Center = %0.2f , %0.2f | R = %0.2f
162 ',ParSlice3(1),ParSlice3(2),ParSlice3(3)));
163
164 % Slice 4: Exact same method as slice 2. Only difference is now the slice
165 % is 90um+-2um below the top
166
167 BalloonDataSlice4positions = find(BalloonData < BalloonDataMax-(3*Zstep-
168 tolerance) & BalloonData > BalloonDataMax-(3*Zstep+tolerance));
169 BalloonDataSlice4values = BalloonData(BalloonDataSlice4positions(1:end));
170 BalloonDataSlice4 = zeros(NumRows,NumCol);
171
172 for i = 1:length(BalloonDataSlice4positions)
173     BalloonDataSlice4(BalloonDataSlice4positions(i)) =
174     BalloonDataSlice4values(i);
175 end
176
177 [BalloonDataSlice4X , BalloonDataSlice4Y] = find(BalloonDataSlice4 ~= 0);
178 BalloonDataSlice4XY = [BalloonDataSlice4X, BalloonDataSlice4Y];
179
180 ParSlice4 = CircleFitKasa(BalloonDataSlice4XY); %fits circle (CenterX,
181 CenterY, Radius)
182
183 for j = 1:360
184     BalloonDataY4(j) = ParSlice4(2)+ParSlice4(3)*cos(j/360*2*pi);
185     BalloonDataX4(j) = ParSlice4(1)+ParSlice4(3)*sin(j/360*2*pi);
186 end
187
188 subplot(3,1,3)
189 plot(BalloonDataSlice4X,BalloonDataSlice4Y,'o');
190 hold on
191 plot(BalloonDataX4, BalloonDataY4, '--r');
192 hold on
193 plot(ParSlice4(1),ParSlice4(2),'xm');
194 hold on
195 title('Slice 4 Points and Circular Fitting');
196 text(ParSlice4(1)+1,ParSlice4(2)+1,sprintf('Center = %0.2f , %0.2f | R = %0.2f
197 ',ParSlice4(1),ParSlice4(2),ParSlice4(3)));
198 %% Slices all found, average the center
199 % Height at Center of Balloon
200
201 Center(1) = round((ParSlice1(1) + ParSlice2(1) + ParSlice3(1) +
202 ParSlice4(1))/4); %Takes row values of the center for each slice and averages
203 to find center of balloon
204 Center(2) = round((ParSlice1(2) + ParSlice2(2) + ParSlice3(2) +
205 ParSlice4(2))/4); %Takes column values of the center for each slice and
206 averages to find center of balloon
207
208 BalloonDataMaxHeight = BalloonData(Center(1),Center(2)) % Heights at the
209 center of the balloon
210

```

```

211 %% Generate cross-sectional views
212
213 % Cross Sectional Views
214 XYStep = 1; % Number of pixels between each cross-sections. Cross-sections
215 will be averaged later
216
217 BalloonDataXconst(:,1) = BalloonData(Center(1),[1:NumCol]); % Holds row
218 constant and pulls out column height values
219 BalloonDataXconst(:,2) = BalloonData(Center(1)+XYStep,[1:NumCol]);% Cross
220 section 1 to the right
221 BalloonDataXconst(:,3) = BalloonData(Center(1)-XYStep,[1:NumCol]); % Cross
222 section 1 to the left
223 BalloonDataXconst(:,4) = BalloonData(Center(1)-2*XYStep,[1:NumCol]); % Cross
224 section 2 to the left
225 BalloonDataXconst(:,5) = BalloonData(Center(1)+2*XYStep,[1:NumCol]); % Cross
226 section 2 to the right
227
228 BalloonDataYconst(:,1) = BalloonData([1:NumRows], Center(2)); % Holds column
229 constant and pulls out the row height values
230 BalloonDataYconst(:,2) = BalloonData([1:NumRows], Center(2)+XYStep); % Cross
231 section 1 up
232 BalloonDataYconst(:,3) = BalloonData([1:NumRows], Center(2)-XYStep); % Cross
233 section 1 down
234 BalloonDataYconst(:,4) = BalloonData([1:NumRows], Center(2)+2*XYStep); % Cross
235 section 2 up
236 BalloonDataYconst(:,5) = BalloonData([1:NumRows], Center(2)-2*XYStep); % Cross
237 section 2 down
238
239 BalloonDataXconst(:,6) = (BalloonDataXconst(:,1) + BalloonDataXconst(:,2) +
240 BalloonDataXconst(:,3) + BalloonDataXconst(:,4) + BalloonDataXconst(:,5))/5; %
241 Averages row constant cross sections
242 BalloonDataYconst(:,6) = (BalloonDataYconst(:,1) + BalloonDataYconst(:,2) +
243 BalloonDataYconst(:,3) + BalloonDataYconst(:,4) + BalloonDataYconst(:,5))/5; %
244 Averages column constant cross sections
245
246 %% Plot cross-sections
247
248 figure(17) % Plotting of the cross sections
249 set(gcf,'Name','Balloon Cross Sections');
250 CrossSectionMaxXconst = max(max(BalloonDataXconst(:,6)));
251 CrossSectionMaxPositionXconst = find(BalloonDataXconst(:,6) ==
252 CrossSectionMaxXconst);
253 plot([-CrossSectionMaxPositionXconst+1:NumCol-
254 CrossSectionMaxPositionXconst].*XYcalibration,BalloonDataXconst(:,6)); %Shifts
255 cross sections to be symmetrical about 0 on x axis
256 title('Cross Sectional Views');
257 xlabel('D [mm]');
258 ylabel('H [um]');
259 hold on
260 CrossSectionMaxYconst = max(max(BalloonDataYconst(:,6)));
261 CrossSectionMaxPositionYconst = find(BalloonDataYconst(:,6) ==
262 CrossSectionMaxYconst);
263 plot([-CrossSectionMaxPositionYconst+1:NumRows-
264 CrossSectionMaxPositionYconst].*XYcalibration,BalloonDataYconst(:,6));
265 hold on

```

```
266 y = [0:0.5:BalloonDataMaxHeight+50];
267 x = zeros(1,length(y));
268 plot(x,y);
269 legend('X Const','Y Const','X = 0');
```

## Appendix B: MATLAB-Based Balloon Diameter Measurement Code Using Kasa's

### Method

```

% Written by Carson Emeigh 06-01-2023
% Code to fit a circle from 3 points manually selected on an image using
Kasa's Method.

1  close all
2  clear all
3  clc
4
5  %% Reads in file
6  scale = 455.04; % scale in terms of [pix/mm]
7
8  filename = ['balloon 1 adjusted.jpg']; %Image to fit a circle to
9  I = imread(filename); %Reads in the image
10 imshow(I); %Displays the image
11 axis on
12 hold on; % holds the axis constant during future point plotting
13
14 %% Point Selection
15 fprintf('Use mouse to click 3 points on perimeter of the circle, then click
16 enter \n')
17 [x,y] = getpts; % manually click points for selection
18 plot(x(1),y(1), 'r+', 'MarkerSize',10, 'LineWidth',2); % plots chosen pt 1
19 hold on
20 plot(x(2),y(2), 'r+', 'MarkerSize',10, 'LineWidth',2); % plots chosen pt 2
21 hold on
22 plot(x(3),y(3), 'r+', 'MarkerSize',10, 'LineWidth',2); % plots chosen pt 3
23 hold on
24
25 %% Circle Fitting
26
27 m12 = (y(2) - y(1))/(x(2)-x(1)); % finds the slope of the line connecting
28 points 1 and 2
29 m12perp = -1/m12; % finds the slope of the line perpendicular to the line
30 connecting points 1 and 2
31 midpt12(1) = (x(1)+x(2))/2; % x coord of the midpoint of the line connecting
32 points 1 and 2
33 midpt12(2) = (y(1)+y(2))/2; % y coord of the midpoint of the line connecting
34 points 1 and 2
35 yintperp = midpt12(2) - m12perp*midpt12(1); % finds y intercept for the line
36 perpendicular to the line connecting points 1 and 2
37
38 plot(midpt12(1),midpt12(2), 'b+', 'MarkerSize',10, 'LineWidth',2); % plots
39 midpoint between points 1 and 2
40 hold on
41
42 center(1) = (x(3)^2 + y(3)^2 - x(1)^2 - y(1)^2 + 2*yintperp*(y(1)-
43 y(3)))/(2*(x(3)-x(1)+ m12perp*(y(3)-y(1)))); %finds x coord for center of
44 circle
45 center(2) = m12perp * center(1) + yintperp; % finds the y coord for the center
46 of the fitted circle

```

```
47 plot(center(1),center(2),'m+','MarkerSize',10,'LineWidth',2); % plots the
48 center point of the circle in magenta
49 hold on
50
51 radius = sqrt((center(1)-x(1))^2 + (center(2)-y(1))^2); % finds the radius of
52 the fitted circle in pixels
53
54 %% Plot the fitted circle onto the image
55
56 theta = 0:pi/50:2*pi; %points to put into circle equation
57 circleX = radius * cos(theta) + center(1); % x coords for the circle
58 circleY = radius * sin(theta) + center(2); % y coords for the circle
59 plot(circleX,circleY,'--','LineWidth',4); % plots the found circle
60 hold on
61
62 plot([circleX(90),center(1)], [circleY(90),center(2)], 'LineWidth',2); % plots
63 radius of circle
64 hold on
65
66 radius = radius / scale; % converts the radius in pixels into a radius in [mm]
67 diameter = radius * 2;
68
69 sprintf('The diameter of the circle is %f mm \n',diameter) % displays the
70 radius of the circle in mm
```

## Appendix C: MATLAB Code Used for PTV Analysis

```

%% Code for PTV particle tracking

%% Written by Carson Emeigh with help and commands from
% https://site.physics.georgetown.edu/matlab/index.html

1  close all
2  clear all
3  clc
4
5  %% Load image and imaging info
6
7  filename = '1652um'; % insert name of file to be analyzed (jpg, tif, bmp, etc)
8  original_image = imread([filename, '.tif']); % reads image file into 'image'
9  variable in MATLAB '.tif' file. File can contain many tif images
10 OG_Img_Fig = figure("Name",'Original Image','NumberTitle','off'); % creates
11 figure for original image
12 OG_Img_Fig = imshow(original_image); % display original image
13 pause(5.0); % pauses commands to look at image
14 info_image = iminfo([filename, '.tif']); % loads info for each frame into
15 individual row
16 num_images = length(info_image); % total number of frames
17
18 fps = 60; % frames per second for recorded video
19 scale = 0.50275; % size of pixel (um/pix)
20
21 %% Image Background Removal
22
23 % Create blank image
24 width = info_image.Width; % width of image (# of pixels)
25 height = info_image.Height; % height of image (# of pixels)
26 BG_image = zeros(height,width); % blank background image
27
28 % Create background image from first 100 frames
29 % Add the frames up and divide by number of frames for the average
30 num_images_backgroundAvg = 50; % number of frame to use when creating
31 background
32
33 for i = 1:num_images_backgroundAvg
34     frame = imread([filename, '.tif'],i); % imports ith frame from image
35     BG_image = BG_image + double(frame); % adds frame values to background
36 image
37 end
38
39 figure
40 BG_image = uint8(BG_image/num_images_backgroundAvg); % takes background image
41 divided by number of frames and converts to uint8 array
42 imshow(BG_image); % displays background image
43 pause(5.0);
44 imwrite(BG_image,'BG.tif'); % write background unit8 matrix into a .tif file
45 clear frame i info_image % clears variables to free up RAM
46
47 % Background Removal to have grayscale images with only the particles

```

```

48 for i = 1:num_images
49     image = imread([filename, '.tif'],i); % reads in ith frame of image
50     image = (255 - image) - (255 - BG_image); % flips ith frame to grayscale,
51     then subtracts background image flipped to grayscale
52
53     if i == 1
54         imwrite(image, 'Image_Reversed.tif'); % write first frame into new
55     image
56     else
57         imwrite(image, 'Image_Reversed.tif', 'WriteMode', 'append'); % writes all
58     frames after onto same image to create multiframe .tif file
59     end
60 end
61 clear image i % clears variables to free up RAM
62
63 figure;
64 imshow('Image_Reversed.tif');
65 pause(5.0);
66
67 %% Begin Particle Tracking
68
69 particle_center = []; % 1st column: x coord, 2nd coord: y coord, 3rd column:
70 time
71 tmp = []; % dummy matrix to compile data into global particle_center matrix
72
73 % num_images = 9; % dummy number used for coding
74
75 for i = 1:num_images % loops over all images
76     frame = imread('Image_Reversed.tif', 'Index', i); % reads in specific image
77     frame
78     figure % create figure for plotting frame
79     frame = rgb2gray(frame); % converts image frame into grayscale
80     imshow(frame); % displays frame on figure
81
82     b = bpass(frame, 1, 2.5); % bandpass filters the images
83     b = imbinarize(b, 5); % not from website, apply my own filter with
84     threshold of 1
85     imshow(b)
86
87     % Next find peak of particles
88     peak = pkfnd(b, 0, 4); % rough guess of location for particle center (pixel
89     accuracy)
90     cnt = cntrd(b, peak, 3); % location of particle centroid (subpixel accuracy)
91     hold on
92     plot(cnt(:, 1), cnt(:, 2), 'r. '); % plots (x,y) for particle onto image
93
94     [L, ~] = size(cnt); % Length of the time column to be added to tmp (add
95     time info to cnt matrix)
96     T = i/fps*ones(L, 1); % Time column to be added
97     tmp = [cnt(:, 1:2) T]; % adds time column to cnt (matrix is 1: x coord 2: y
98     coord 3: time)
99     particle_center = [particle_center; tmp]; % compiles matrix of particle
100    center with timestamp
101    clear tmp T
102    close

```

```

103 end
104 clear cnt peak
105
106 % Correlate found particles across many frames
107 tr = track(particle_center, 10); % column left to right: x, y, t, particle id
108 % x y values are in pixels
109
110 clear particle_center
111
112 %% Calculate particle velocity
113 particle_trajectory = []; % 1st column: x-coordinate, 2nd column: y-
114 coordinate, 3rd column: speed, 4th column: time, and 5th column: particle id
115 tmp = [];
116
117 pid_max = max(tr(:,4)); % Max particle id
118 Index = 1;
119 for i = 1:pid_max
120     row = find(tr(:,4) == i); % rows of the pid_max of interest
121     L = length(row);
122
123     if L ~= 1
124         x = tr(row,1)*scale; % Conversion of the center coordinates from
125 pixel to um
126         y = tr(row,2)*scale;
127         t = tr(row,3);
128         v = sqrt(diff(x).^2 + diff(y).^2)./diff(t); % Speed in um/s
129         v = [v; v(L-1)]; % To match length between v and x by adding
130 the last v value as the L-th element (this approach may cause a problem in
131 plotting speed)
132
133         pid = Index*ones(L,1); % Particle id column to be added
134         tmp = [x y v t pid];
135         particle_trajectory = [particle_trajectory; tmp];
136         Index = Index + 1;
137     end
138
139     clear tmp x y v t L pid row
140 end
141 clear tr
142
143
144 %% Display found speed
145 AvgSpeed = mean(particle_trajectory(:,3));
146 sprintf('The Average Particle Speed is %0.3f [um/s]',AvgSpeed)
147
148 StdDev = std(particle_trajectory(:,3))
149 %Save Variables
150 save("1652umData.mat")

```

## Appendix D: MATLAB Code Used for Mixing Analysis

```

%% Code to Image Process microchannel mixing of red and blue dye
%% Written on 2/21/2024 by Carson Emeigh

1  clear all
2  close all
3  clc
4
5  % Read in image
6  image = imread(['0HzRotated.jpg']); % load in image
7  image = imrotate(image,90); % rotate image so that channel is vertical
8  imshow(image); % display image
9  Icropped0Hz = imcrop; % choose cropped region, double click after region is
10 selected
11 imshow(Icropped0Hz); % show cropped image
12 scale = 3.5/110; % mm/pix
13
14 %Read in 3 other images
15 image = imread(['1HzRotated.jpg']); % load in image
16 image = imrotate(image,90); % rotate image so that channel is vertical
17 imshow(image);
18 Icropped1Hz = imcrop;
19 imshow(Icropped1Hz); % show cropped image
20
21 image = imread(['5HzRotated.jpg']); % load in image
22 image = imrotate(image,90); % rotate image so that channel is vertical
23 imshow(image)
24 Icropped5Hz = imcrop;
25 imshow(Icropped5Hz); % show cropped image
26
27 image = imread(['10HzRotated.jpg']); % load in image
28 image = imrotate(image,90); % rotate image so that channel is vertical
29 imshow(image);
30 Icropped10Hz = imcrop;
31 imshow(Icropped10Hz); % show cropped image
32
33 image = imread(['15HzRotated.jpg']); % load in image
34 image = imrotate(image,90); % rotate image so that channel is vertical
35 imshow(image);
36 Icropped15Hz = imcrop;
37 imshow(Icropped15Hz); % show cropped image
38
39 % Find average value
40 red0Hz = mean(Icropped0Hz(:,:,1)); %extract red pixels and average
41 blue0Hz = mean(Icropped0Hz(:,:,3)); %extract blue pixels and average
42
43 red1Hz = mean(Icropped1Hz(:,:,1)); %extract red pixels and average
44 blue1Hz = mean(Icropped1Hz(:,:,3)); %extract blue pixels and average
45
46 red5Hz = mean(Icropped5Hz(:,:,1)); %extract red pixels and average
47 blue5Hz = mean(Icropped5Hz(:,:,3)); %extract blue pixels and average
48

```

```

49 red10Hz = mean(Icropped10Hz(:,:,1)); %extract red pixels and average
50 blue10Hz = mean(Icropped10Hz(:,:,3)); %extract blue pixels and average
51
52 red15Hz = mean(Icropped15Hz(:,:,1)); %extract red pixels and average
53 blue15Hz = mean(Icropped15Hz(:,:,3)); %extract blue pixels and average
54
55 % Normalization
56 MaxRed = 158; % normalization found from channel before mixing
57 MinRed = 92;
58 MaxBlue = 155;
59 MinBlue = 42;
60
61 red0Hz = (red0Hz - MinRed)/(MaxRed - MinRed); % normalized red values
62 blue0Hz = (blue0Hz - MinBlue)/(MaxBlue - MinBlue); % normalize blue values
63
64 red1Hz = (red1Hz - MinRed)/(MaxRed - MinRed); % normalized red values
65 blue1Hz = (blue1Hz - MinBlue)/(MaxBlue - MinBlue); % normalized blue values
66
67 red5Hz = (red5Hz - MinRed)/(MaxRed - MinRed); % normalize red values
68 blue5Hz = (blue5Hz - MinBlue)/(MaxBlue - MinBlue); % normalized blue values
69
70 red10Hz = (red10Hz - MinRed)/(MaxRed - MinRed); % normalized red values
71 blue10Hz = (blue10Hz - MinBlue)/(MaxBlue - MinBlue); % normalized blue values
72
73 red15Hz = (red15Hz - MinRed)/(MaxRed - MinRed); % normalized red values
74 blue15Hz = (blue15Hz - MinBlue)/(MaxBlue - MinBlue); % normalized blue values
75
76 % Plotting results
77 x0Hz = [-length(red0Hz)/2:1:length(red0Hz)/2];
78 x0Hz = x0Hz .* scale;
79 x0Hz(end) = [];
80
81 x1Hz = [-length(red1Hz)/2:1:length(red1Hz)/2];
82 x1Hz = x1Hz .* scale;
83 x1Hz(end) = [];
84
85 x5Hz = [-length(red5Hz)/2:1:length(red5Hz)/2];
86 x5Hz = x5Hz .* scale;
87 x5Hz(end) = [];
88
89 x10Hz = [-length(red10Hz)/2:1:length(red10Hz)/2];
90 x10Hz = x10Hz .* scale;
91 x10Hz(end) = [];
92
93 x15Hz = [-length(red15Hz)/2:1:length(red15Hz)/2];
94 x15Hz = x15Hz .* scale;
95 x15Hz(end) = [];
96
97 plot(1000,1000,'blacko');
98 hold on
99 plot(x0Hz,red0Hz,'-o','Color','#FF0000');
100 hold on
101 plot(x0Hz,blue0Hz,'-o','Color','#00B2FF');
102 hold on
103

```

```

104 plot(1000,1000,'blacksquare')
105 hold on
106 plot(x1Hz,red1Hz,'-square','Color','#FF5F5F');
107 hold on
108 plot(x1Hz,blue1Hz,'b-square','Color','#58CCFF');
109 hold on
110
111 scatter(1000,1000,'blackdiamond')
112 hold on
113 plot(x5Hz,red5Hz,'-diamond','Color','#FF8181');
114 hold on
115 plot(x5Hz,blue5Hz,'-diamond','Color','#58CCFF');
116 hold on
117
118 scatter(1000,1000,'black+')
119 hold on
120 plot(x10Hz,red10Hz,'-+', 'Color', '#FF8181');
121 hold on
122 plot(x10Hz,blue10Hz,'-+', 'Color', '#A3E3FF');
123 hold on
124
125 scatter(1000,1000,'black^')
126 hold on
127 plot(x15Hz,red15Hz,'-^','Color','#FFC4C4');
128 hold on
129 plot(x15Hz,blue15Hz,'-^','Color','#D0F1FF');
130 hold on
131
132 centerX = [0,0];
133 centerY = [-.1,1.1];
134 plot(centerX,centerY,'black--');
135
136 xlim([-1.5,1.5]);
137 ylim([-0.1,1.1]);
138
139 xlabel('Channel Width [mm]');
140 ylabel('Normalized Intensity');
141 leg = legend('0 Hz', '', '1 Hz', '', '5 Hz', '', '10 Hz', '', '15
142 Hz', '', '');
143 leg.TextColor = 'black';
144
145 %% Calculate Mixing Efficiency
146 % Use average of cropped image
147 % Based on mixing of red dye relative to mixing at 15 Hz (avg of all pixels
148 % at 15 Hz)
149
150 % For 0Hz
151 I_inf = mean(red15Hz); % normalized intensity at complete mixing (assumed to
152 be mixing at 15 Hz)
153 IRed_NoMix = 1; % normalized red value at no mixing (1)
154
155 N0Hz = length(red0Hz); % number of pixels across the channel width
156 Rsum0Hz_Numerator = (red0Hz(1) - I_inf).^2; % Riedmann sum numerator of mixing
157 efficieny equation first value

```

```

158 Rsum0Hz_Denominator = (IRed_NoMix - I_inf).^2; % Riedmann sum denominator of
159 mixing efficiency equation first value
160
161 for i = 2:N0Hz % for loop to calculate values of Riedmann sums
162 Rsum0Hz_Numerator = Rsum0Hz_Numerator + (red0Hz(i) - I_inf).^2;
163 Rsum0Hz_Denominator = Rsum0Hz_Denominator + (IRed_NoMix - I_inf).^2;
164 end
165
166 MixEff0Hz_NumeratorRed = sqrt( (1/N0Hz)*Rsum0Hz_Numerator );
167 MixEff0Hz_DenominatorRed = sqrt( (1/N0Hz)*Rsum0Hz_Denominator );
168 MixEff0Hz = 1 - (MixEff0Hz_NumeratorRed./MixEff0Hz_DenominatorRed); % mixing
169 efficiency equation
170
171 % For 1Hz
172 I_inf = mean(red15Hz); % normalized intensity at complete mixing (assumed to
173 be mixing at 15 Hz)
174 IRed_NoMix = 1; % normalized red value at no mixing (1)
175
176 N1Hz = length(red1Hz); % number of pixels across the channel width
177 Rsum1Hz_Numerator = (red1Hz(1) - I_inf).^2; % Riedmann sum numerator of mixing
178 efficiency equation first value
179 Rsum1Hz_Denominator = (IRed_NoMix - I_inf).^2; % Riedmann sum denominator of
180 mixing efficiency equation first value
181
182 for i = 2:N1Hz % for loop to calculate values of Riedmann sums
183 Rsum1Hz_Numerator = Rsum1Hz_Numerator + (red1Hz(i) - I_inf).^2;
184 Rsum1Hz_Denominator = Rsum1Hz_Denominator + (IRed_NoMix - I_inf).^2;
185 end
186
187 MixEff1Hz_NumeratorRed = sqrt( (1/N1Hz)*Rsum1Hz_Numerator );
188 MixEff1Hz_DenominatorRed = sqrt( (1/N1Hz)*Rsum1Hz_Denominator );
189 MixEff1Hz = 1 - (MixEff1Hz_NumeratorRed./MixEff1Hz_DenominatorRed); % mixing
190 efficiency equation
191
192 % For 5Hz
193 I_inf = mean(red15Hz); % normalized intensity at complete mixing (assumed to
194 be mixing at 15 Hz)
195 IRed_NoMix = 1; % normalized red value at no mixing (1)
196
197 N5Hz = length(red5Hz); % number of pixels across the channel width
198 Rsum5Hz_Numerator = (red5Hz(1) - I_inf).^2; % Riedmann sum numerator of mixing
199 efficiency equation first value
200 Rsum5Hz_Denominator = (IRed_NoMix - I_inf).^2; % Riedmann sum denominator of
201 mixing efficiency equation first value
202
203 for i = 2:N5Hz % for loop to calculate values of Riedmann sums
204 Rsum5Hz_Numerator = Rsum5Hz_Numerator + (red5Hz(i) - I_inf).^2;
205 Rsum5Hz_Denominator = Rsum5Hz_Denominator + (IRed_NoMix - I_inf).^2;
206 end
207
208 MixEff5Hz_NumeratorRed = sqrt( (1/N5Hz)*Rsum5Hz_Numerator );
209 MixEff5Hz_DenominatorRed = sqrt( (1/N5Hz)*Rsum5Hz_Denominator );
210 MixEff5Hz = 1 - (MixEff5Hz_NumeratorRed./MixEff5Hz_DenominatorRed); % mixing
211 efficiency equation
212

```

```

213 % For 10Hz
214 I_inf = mean(red15Hz); % normalized intensity at complete mixing (assumed to
215 be mixing at 15 Hz)
216 IRed_NoMix = 1; % normalized red value at no mixing (1)
217
218 N10Hz = length(red10Hz); % number of pixels across the channel width
219 Rsum10Hz_Numerator = (red10Hz(1) - I_inf).^2; % Riedmann sum numerator of
220 mixing efficieny equation first value
221 Rsum10Hz_Denominator = (IRed_NoMix - I_inf).^2; % Riedmann sum denominator of
222 mixing efficiency equation first value
223
224 for i = 2:N10Hz % for loop to calculate values of Riedmann sums
225 Rsum10Hz_Numerator = Rsum10Hz_Numerator + (red10Hz(i) - I_inf).^2;
226 Rsum10Hz_Denominator = Rsum10Hz_Denominator + (IRed_NoMix - I_inf).^2;
227 end
228
229 MixEff10Hz_NumeratorRed = sqrt( (1/N10Hz)*Rsum10Hz_Numerator );
230 MixEff10Hz_DenominatorRed = sqrt( (1/N10Hz)*Rsum10Hz_Denominator );
231 MixEff10Hz = 1 - (MixEff10Hz_NumeratorRed./MixEff10Hz_DenominatorRed); %
232 mixing efficiency equation
233
234 % For 15Hz
235 I_inf = mean(red15Hz); % normalized intensity at complete mixing (assumed to
236 be mixing at 15 Hz)
237 IRed_NoMix = 1; % normalized red value at no mixing (1)
238
239 N15Hz = length(red15Hz); % number of pixels across the channel width
240 Rsum15Hz_Numerator = (red15Hz(1) - I_inf).^2; % Riedmann sum numerator of
241 mixing efficieny equation first value
242 Rsum15Hz_Denominator = (IRed_NoMix - I_inf).^2; % Riedmann sum denominator of
243 mixing efficiency equation first value
244
245 for i = 2:N15Hz % for loop to calculate values of Riedmann sums
246 Rsum15Hz_Numerator = Rsum15Hz_Numerator + (red15Hz(i) - I_inf).^2;
247 Rsum15Hz_Denominator = Rsum15Hz_Denominator + (IRed_NoMix - I_inf).^2;
248 end
249
250 MixEff15Hz_NumeratorRed = sqrt( (1/N15Hz)*Rsum15Hz_Numerator );
251 MixEff15Hz_DenominatorRed = sqrt( (1/N15Hz)*Rsum15Hz_Denominator );
252 MixEff15Hz = 1 - (MixEff15Hz_NumeratorRed./MixEff15Hz_DenominatorRed); %
253 mixing efficiency equation
254
255 % Plotting the results
256
257 MixEff = [MixEff0Hz, MixEff1Hz, MixEff5Hz, MixEff10Hz, MixEff15Hz];
258 MixEff = MixEff .* 100
259 Freq = [0, 1, 5, 10, 15];
260
261 figure;
262 scatter(Freq,MixEff,'filled');
263 hold on
264 xlim([0,15]);
265 ylim([50,100]);
266 xlabel('Frequency [Hz]');
267 ylabel('{\it \eta [%]}');

```